Radar Sounding of Disperse Streams

DISSERTATION

zur Erlangung des akademischen Grades

Doktor der Ingenieurwissenschaften
(Dr.-Ing.)

der Technischen Fakultät
der Christian-Albrechts-Universität zu Kiel

Oleksandr Teplyuk

Kiel
2012

1. Gutachter: Prof. Dr.-Ing. R. Knöchel
2. Gutachter: Prof. Dr.-Ing. Dr. h.c. K. Schünemann
3. Gutachter: Prof. Dr. G. I. Khlopov

Datum der mündlichen Prüfung: 17.02.2012

Acknowledgements

Among all who have contributed to my post graduate education, my greatest appreciation surely belongs to Prof. Dr.-Ing. Reinhard Knöchel, Prof. Dr.-Ing. Dr. h. c. Klaus Schünemann, and Prof. Dr. Grygoriy Khlopov, who guided me through this thesis. I would like to thank my academic mentor Prof. Knöchel for the given opportunity to work in his workgroup as a research fellow. This thesis would not have been possible without his great assistance and support. I also owe a huge debt of gratitude to Prof. Schünemann for his strong interest and support of my work and particularly for his invaluable advices and help with correction of the manuscript. I especially would like to thank my scientific advisor Prof. Khlopov who has encouraged me to do this research and supported me in many ways over the last ten years. Many thanks are due to him for his wise advices and thoughtful guidance all along the dissertation.

Nevertheless, my acknowledgement would not be complete without mentioning the other members of the microwave workgroup of the Christian-Albrechts-University of Kiel especially Dipl.-Ing. (FH) Wolfgang Taute, Dr.-Ing. Frank Daschner, and Miss Melanie Bork, who have made available their support in many ways during my post graduate study. I would like to acknowledge them for their professionalism, their encouragement, and for their friendship.

Last but not least, I would like to express my deepest gratitude to my wife Victoria for her patience and support.

Kiel, June 2012 Oleksandr Teplyuk

Contents

Acknowledgements ..... **i**
List of abbreviations and symbols ..... **v**
List of figures ..... **xiii**
List of tables ..... **xvii**
Introduction **1**
1 State of the art **5**
2 Theoretical background **11**
2.1 Properties of bistatic sensing of volume scatterers 11
2.1.1 Bistatic radar equation for volume scatterers 11
2.1.2 Scattering volume of bistatic sensing 14
2.1.3 Illumination of the scattering volume 16
2.2 Mono-frequency sounding of disperse streams 18
2.2.1 Sounding of monodisperse streams 18
2.2.2 Sounding of polydisperse streams 20
2.3 Double-frequency sounding of disperse streams 23
2.3.1 Differential radar cross-section 23
2.3.2 Application of Mie theory for calculation of the particle RCS 24
2.3.3 Application limits of double-frequency method 26
2.3.4 Sounding of polydisperse streams with “narrow” particle size distribution 27
2.3.5 Sounding of polydisperse streams with “wide” particle size distribution 29
2.4 Conclusions to Chapter 2 31

3 Development of radar-sensors for remote sensing of disperse streams **33**
3.1 Mono-frequency bistatic radar-sensor 33
3.1.1 Configuration of a mono-frequency bistatic radar-sensor 34
3.1.2 Antenna system of the mono-frequency bistatic radar-sensor 36
3.1.3 Design of the bistatic radar-sensor 39
3.1.4 Signal processing of the radar-sensor in spectral domain 41
3.1.5 Signal processing of radar-sensor in time domain 43

3.2 Mono-frequency monostatic quasioptical radar-sensor 48
3.2.1 Configuration of the antenna feeder system 48
3.2.2 Development of duplex device 49
3.2.3 Development of near-field offset Gregorian antenna 56
3.2.4 Configuration of the mono-frequency monostatic radar-sensor 62
3.2.5 Design of the mono-frequency monostatic radar-sensor 64
3.3 Double-frequency bistatic radar-sensor 66
3.3.1 Configuration of the double-frequency bistatic radar-sensor 66
3.3.2 Antenna system of the double-frequency bistatic radar-sensor 67
3.3.3 Design of the double-frequency radar-sensor 72
3.4 Conclusions to Chapter 3 75

4 Experimental study of remote sensing of disperse streams 79
4.1 Development of the experimental set-up 79
4.1.1 Experimental set-up configuration 79
4.1.2 Study of a screw dispenser for the experimental set-up 81
4.1.3 Development of an ejecting dispenser for the experimental set-up 82
4.1.4 Powder materials for the full-scale experiments 86
4.2 Comparison of remote sensing by a mono-frequency radar-sensor and by contact measurements 90
4.2.1 Algorithm of data processing 90
4.2.2 Calibration of the mono-frequency radar-sensor 92
4.2.3 Results of experimental study 93
4.3 Comparison of remote sensing by a double-frequency radar-sensor and by contact measurements 96
4.3.1 Algorithm of data processing 97
4.3.2 Results of the experimental study 100
4.4 Conclusions to Chapter 4 101

Summary 103
References 107

List of abbreviations and symbols

Abbreviations

A/D	Analog-to-digital
ADS	Advanced design system (software)
AT	Attenuator
CF	Correlation function
CNC	Computer numerical control
CW	Continuous wave
DC	Directional coupler
DD	Duplex device
DFA	Doppler frequency amplifier
DG	Driving generator
DRCS	Differential radar cross-section
FC	Ferrite circulator
FEPA	Federation of European Producers of Abrasives
FFT	Fast Fourier transform
FI	Ferrite isolator
HFSS	High Frequency Structure Simulator (software)
HLA	Horn-lens antenna
HPF	High-pass filter
IF	Intermediate frequency
IFA	Intermediate frequency amplifier
IFPA	Intermediate frequency preamplifier
IMPATT	Impact avalanche transit time
LO	Local oscillator
LPF	Low-pass filter
MATLAB	Matrix laboratory (software)
MGC	Manual gain control
mps	Meter per second
Mx	Mixer
NF	Noise factor
NG	Noise generator
PA	Power amplifier
PBF	Pass-band filter
PC	Personal computer
rpm	Rotation per minute

PSD	Power spectral density
RCS	Radar cross-section
RMS	Root-mean-square
SNR	Signal-to-noise ratio
TE	Transverse electric (wave)
TEM	Transverse electromagnetic (wave)
TM	Transverse magnetic (wave)
TRL	Transmission/reception loss
WL	Waveguide launcher

Latin symbols

A	Constant
A_n	Logarithmic derivative of 1st order Riccati-Bessel function
a_n	Complex expansion coefficient of scattered field
B	Constant
b_n	Complex expansion coefficient of scattered field
C	Powder flow rate
$\bar{D}$	Normalized RMS distance
D_A	Size of antenna aperture
D_c	Particle container diameter
D_e	Aperture size of equivalent axisymmetric main reflector
D_{et}	Diameter of etalon sphere
D_r	Aperture size of main reflector
d	Particle diameter
d_3	Root-mean-cube diameter
d_e	Aperture size of equivalent axisymmetric secondary reflector
d_{mean}	Mean value of particle diameter
d_{mode}	Modal value of particle diameter
d_n	Nozzle diameter
d_s	Aperture size of secondary reflector
Δd	Fraction size
E	Electric field
E_0	Amplitude of electric field
e	Euler's number
F	Antenna pattern, Focal distance
F^2	Antenna power pattern

F_0	Amplitude constant
F_D	Efficiency factor
F_R	Receiving antenna pattern
F_R^2	Receiving antenna power pattern
F_r	Focal distance of equivalent reflector
F_T	Transmitting antenna pattern
F_T^2	Transmitting antenna power pattern
F_s	Focal distance of secondary reflector
F_X	Cumulative probability function
f	Frequency
f_c	Cut-off frequency
Δf	Bandwidth
Δf_{eq}	Bandwidth of the equivalent filter
f_0	Operating frequency
f_D	Doppler frequency shift
f_{IF}	Intermediate frequency
f_{IF}^R	Instant value of IF in the output of reference channel
$\overline{f}_{IF}$	Average value of IF in the output of reference channel
Δf_{IF}	Frequency fluctuations of IF in the output of reference channel
f_{IF}^S	Instant value of IF in the output of signal channel
Δf_{LO}	Frequency fluctuations of heterodyne
Δf_T	Frequency fluctuations of driving generator
$\overline{f}_{LO0}$	Average value of heterodyne frequency
$\overline{f}_{T0}$	Average value of carrier frequency
f_X	Probability density function
G	Antenna gain
G_0	Antenna gain along the pattern axis
G_{0R}	Antenna gain along the pattern axis of receiving antenna
G_{0T}	Antenna gain along the pattern axis of transmitting antenna
G_{IFA}	IFA gain
G_R	Receiving antenna gain
G_T	Transmitting antenna gain
g	Parameter of log-normal distribution
h	Thickness of dielectric layer
h_p	Thickness of particle layer

h_r, h_s	Distance
I	Intensity
J_n	1st order Bessel function
$K(\tau)$	Correlation function
$K_N(\tau)$	Correlation function of receiver noise
$K_S(\tau)$	Correlation function of signal
$K_{SN}(\tau)$	Correlation function of signal and noise composition
K_l	Medium loss
k	Wave number, Boltzmann constant, Index number
k_d	Calibration constant
L	Distance
L_c	Coefficient of losses
M	Mass loading
M^{ef}	Effective value of mass loading
m	Index number
$\dot{m}$	Complex refractive index
m_k	Distribution moment of kth order
N	Number of particles
N_0	Number of particles in volume unit
NF	Noise factor
N_T	Total particle number
N_T^{ef}	Effective value of total particle number
n	Index number
n_r	Particle size distribution
P	Power
$P_d^{\min}$	Minimum detected signal
P_{DS}	Power reflected from disperse stream
P_{et}	Power reflected from etalon reflector
P_i	Power reflected from single particle
$P_l^{\max}$	Maximum leakage signal
$P_{\min}$	Minimum signal power at peak sensitivity
P_N	Noise power
P_R	Received power
P_S	Signal power
PSD	Power spectral density
P_T	Transmitter power
p_i	Polarization constant

Q	Gas consumption
q	Index number
q_i	Polarization constant
R	Distance
R_D	Power ratio in lateral port of DD
R_{et}	Distance to etalon reflector
R_f	Curvature radius of phase front
R_R	Distance from receiving antenna to scattering element
R_T	Distance from transmitting antenna to scattering element
R_X	Receiver
r	Particle radius, Reflection coefficient
r_0	Average particle radius
Δr	Distribution width of log-normal distribution
$\overline{\Delta r}$	Normalized distribution width
Δr_e	Distribution width of etalon log-normal distribution
r_D	Coefficient of polarisation plane orientation
r_{mod}	Distribution mode of log-normal distribution
r_{mod}^0	True value of distribution mode for log-normal distribution
r_{mod}^{ef}	Effective value of modal particle radius
$r_{\text{mod}}^{\max}$	Upper boundary of unambiguous measurement of particle size
$r_{\text{mod}}^{\min}$	Lower boundary of unambiguous measurement of particle size
r_{mono}	Upper boundary of particle size measurement for monodisperse stream
r_{rms}^{ef}	Effective RMS radius
S	Signal spectrum
S_0	Spectrum amplitude constant
S_D	Duct cross-section
$S_m(\Omega)$	Square modulus of FFT
S_{TR}	Receiver/transmitter isolation
s	Linear deviation
s_r	Parameter of log-normal distribution
s_V	Linear size of scattering volume
T	Absolute temperature and Period
T_0	Signal realisation time
T_D	Power ratio in strait port of DD
T_s	Sampling interval
T_X	Transmitter

t	Time
t_{int}^{pre}	Predetection integration time
t_{int}^{post}	Postdetection integration time
$\tan(\delta)$	Loss tangent
$U(t)$	Radar output signal
U_0	Amplitude of constant component
$U_D(t)$	Doppler signal
U_{D0}	Amplitude of Doppler signal
U_{l0}	Amplitude of leakage signal
$U_N(t)$	Receiver noise
$U_R(t)$	Signal from reference channel
U_{R0}	Amplitude of signal from reference channel
$U_S(t)$	Wanted signal, Signal from signal channel
$U_{SN}(t)$	Signal and noise composition
U_{S0}	Amplitude of signal from signal channel
V	Volume, Scattering volume
ΔV	Volume resolution
V_0	Starting voltage
V_{ef}	Effective scattering volume
V_l	Volume of displaced liquid
v_s	Speed of powder supply
v	Stream velocity
v_c	Conveyor belt speed
$v_{\max}$	maximal velocity of calibrating sphere
x	Transversal coordinate
$x_{\max}$	Transversal coordinate of the side boundary of the effective scattering volume
x_R	Transversal coordinate of the aperture center of receiving antenna
x_T	Transversal coordinate of the aperture center of transmitting antenna
y	Transversal coordinate
y_R	Transversal coordinate of the aperture center of receiving antenna
y_T	Transversal coordinate of the aperture center of transmitting antenna
Z	Reflectivity
z	Transversal coordinate
z_0	Longitudinal coordinate of antenna beams interception point
z_f	Fresnel distance
$z_{\max}$	Longitudinal coordinate of the upper boundary of effective scattering volume

$z_{\min}$	Longitudinal coordinate of the lower boundary of effective scattering volume
z_R	Longitudinal coordinate of the aperture center of receiving antenna
z_T	Longitudinal coordinate of the aperture center of transmitting antenna

Greek symbols

α	Wavelength ratio, proportionality constant
α_a	Convergence angle of the antenna beams
β	Phase incursion, interception angle, and proportionality constant
Γ	Reflection coefficient
γ	Distribution moment ratio, Weibull distribution parameter
$\overline{\Delta\gamma}$	Relative error of distribution moment ratio
δ	Dirac delta-function
δ_r	Normalized deviate of effective distribution mode
$\delta_{\Delta f}$	Fluctuation spectrum width of generator
ε	Permittivity, detection limit
$\dot{\varepsilon}$	Complex permittivity
ε'	Real part of complex permittivity
ε''	Imaginary part of complex permittivity
η_{T-R}	Transmission/reception loss
θ	Diffraction angle, Angle of incidence
θ_0	Antenna power pattern halfwidth at -3 dB level
θ_e	Antenna power pattern halfwidth at 1/e level
θ_R	Elevation angle of receiving antenna
θ_T	Elevation angle of transmitting antenna
ϑ	Polar angle
λ	Operating wavelength
$\lambda_{\max}$	Maximum operating wavelength
$\lambda_{\min}$	Minimum operating wavelength
ξ	Ejection coefficient
$\overline{\Pi}$	Normalized signal-to-noise ratio
ρ	Transversal coordinate in cylindrical coordinate system, diffraction parameter;
ρ^{ef}	Effective diffraction parameter
ρ_{mod}	Modal diffraction parameter
ρ^0_{mod}	True value of modal diffraction parameter
ρ^{ef}_{mod}	Effective value of modal diffraction parameter
ρ_p	Particle material density g/m^3

ρ_ε	Diffraction parameter depending on material permittivity
$\rho^{\max}$	Maximum value of diffraction parameter
$\rho^{\min}$	Minimum value of diffraction parameter
ρ_{rmc}^{ef}	Effective RMC value of diffraction parameter
σ	Radar cross-section
σ_0	Specific radar cross-section
$\sigma_0^x(\lambda)$	Specific RCS measured for wavelength λ
σ_D	Differential radar cross-section (DRCS)
σ_D^e	Calculated DRCS for equivalent polydisperse medium
σ_D^x	Measured value of DRCS
σ_{et}	RCS of calibration sphere
$\Delta\sigma_{\min}$	Accuracy of DRCS measurement
σ_N^2	Dispersion of noise
σ_p	Radar cross-section of single particle
σ_S^2	Dispersion of signal
σ_t	Total scattering cross-section of a single particle
ς_n	3rd order Riccati-Bessel function
τ	Time delay
τ_N	Correlation window of noise
τ_R	Time of signal propagation to the target and back
τ_S	Correlation window of signal
$\Delta\varphi$	Phase incursion
φ_0	Phase of constant component
φ_D	Phase of Doppler signal
φ_l	Phase of leakage signal
φ_R	Phase of the signal from reference channel
φ_S	Phase of the signal from signal channel
χ	Weibull distribution parameter
ψ_n	1st order Riccati-Bessel function
Ω	Angular frequency
ω	Gaussian beamwidth, Angular frequency
ω_0	Gaussian beamwidth in antenna aperture
ω_D	Angular Doppler frequency
ω_N	Receiver bandwidth
$\Delta\omega_S$	Signal bandwidth

List of figures

1.1 Optical microscope 5
1.2. Set of sieves – a) and mechanical shaker –b) used for sieving analysis 6
1.3 Configuration of sedimentary method (after Slot R.&Geldof H. (1979). Design Aspects and Performance of a Settling Tube System. Laboratory of Fluid Mechanics, Delft University of Technology Internal Report no. 6-79: 18pp.) 6
1.4 Configuration of laser velosimetry method [6] 7
1.5 Configuration of triboelectric method 7
1.6 Configuration of light absorbtion method 7
1.7 Configuration of light scattering method 8
1.8 Configuration of scattering indicantrix method 8
1.9 Configuration of light absorption method [9] 8
1.10 Conception of laser diffraction method [10] 9
2.1 Bistatic radar configuration 12
2.2 Geometry of a bistatic radar antenna system 14
2.3 Illumination of the effective scattering volume 17
2.4 Normalized signal-to-noise ratio for a volume scatterer 18
2.5 Particle size distribution: a) – distribution type; b) parameters of distribution 19
2.6 Log-normal particle size distribution 22
2.7 The relative error of moment ratio for the polydisperse medium 23
2.8 Type of scattering from dielectric particle 25
2.9 Typical dependence of the DRCS on the diffraction parameter 26
2.10 DRCS dependence for polydisperse stream 27
2.11 DRCS dependence for polydisperse disperse stream 29
2.12 Error of approximation for polydisperse medium 30
3.1 Block diagram of the coherent radar in 3mm waveband 34
3.2 Model for the simulation of the HLA – a); field structure of the feed – b) 36
3.3 Horn-lens antenna design 37
3.4 Measurement of the antenna near fields 37
3.5 3D field plot in the aperture of the HLA 38
3.6 Field distribution in HLA aperture (blue),Gaussian beam (black). a)H-plane; b) E-plane 38
3.7 Power pattern of the HLA (blue) and its Gaussian beam approximation (black). a) H-plane; b) E-plane 39
3.8 Design of the coherent radar in the 3mm wave band 39

3.9 Frequency characteristic of the LPF – a); outlook of the LPF – b) 40
3.10 Signal spectrum reflected from corundum particles 42
3.11 The correlation function of a noise-like signal with Doppler frequency shift and the correlation function of the noise 43
3.12 Dependence of normalized receiver bandwidth on mean Doppler frequency 45
3.13 Block diagram of the correlation experiment set-up 46
3.14 Spectra– a) and correlation functions of the simulated signals – b) 46
3.15 Dependence of the output SNR on the input SNR 47
3.16 Spectrum of signal and vibrating duct 47
3.17 Configuration of quasioptical transmit-receive antenna-feeder path 49
3.18 Dependence of TRL loss on frequency deviation 51
3.19 Outlook of the duplex device 52
3.20 Workbench for measurement of the DD field structure 52
3.21 Configuration for measurement of the DD field structure 53
3.22 DD power profiles in the beam cross section at $z = 0\,\text{mm}$ 53
3.23 DD power profiles in the beam cross section at $z = 500\,\text{mm}$ 53
3.24 DD power profiles in the beam cross section at $z = 1000\,\text{mm}$ 54
3.25 Dependence of the DD beamwidth in H-plane (solid line – calculation; * – transmitting channel; ° – receiving channel) 54
3.26 Dependence of the DD beamwidth in E-plane (solid line – calculation; * – transmitting channel; ° – receiving channel) 55
3.27 Measurement configuration of diffraction loss of the beam-waveguide junction 55
3.28 Measurement configuration of DD isolation in "transmit-receive" mode 56
3.29 Design of double-mirror near field antennas using Cassegrainian geometry – a) and offset Gregorian geometry – b) 57
3.30 Outlook of the offset near-field Gregorian antenna with quasioptical DD 58
3.31 Measurement of the antenna field structure in anechoic chamber 59
3.32 Antenna field measurement configuration 59
3.33 Power profile in the antenna aperture at $z = 0\,\text{mm}$ (dash – R_X; dots – T_X; solid line – Gaussian beam) 59
3.34 Power profile in the beam cross-section at $z = 600\,\text{mm}$ (dash – R_X; dots – T_X; solid line – Gaussian beam) 60
3.35 Power profile in the beam cross-section at $z = 1200\,\text{mm}$ (dash – R_X; dots – T_X; solid line – Gaussian beam) 60
3.36 3D field structure of the receiving channel – a) and transmitting channel – b), distance $z = 100\,\text{mm}$ 61
3.37 3D field structure of the receiving channel – a) and transmitting channel – b), distance $z = 1200\,\text{mm}$ 61
3.38 Dependence of the antenna beamwidth in H-plane (solid curve – calculations; * – transmitting channel; ° – receiving channel) 62

3.39 Dependence of the antenna beamwidth in E-plane (solid line – calculations; * – transmitting channel; ° – receiving channel) 62
3.40 Monostatic radar configuration 63
3.41 Outlook of the monostatic coherent radar 65
3.42 pectrum of signals reflected from drizzle 66
3.43 Block diagram of 8 mm radar-sensors 67
3.44 Simulation of the horn-lens antenna in HFSS environment: a) – calculating model b) – field distribution 68
3.45 HLA design 68
3.46 Measurement of the HLA in an anechoic chamber 69
3.47 3D power profile of the antennas, $z = 200\,\text{mm}$: a) – R_X; b) – T_X 69
3.48 3D power profile of the antennas, $z = 1200\,\text{mm}$: a) – R_X; b) – T_X 70
3.49 Power profile of the beam at $z = 0\,\text{mm}$ (blue – R_X; red – T_X; black – Gaussian beam) 70
3.50 Power profile of the beam at $z = 100\,\text{mm}$ (blue – R_X; red – T_X; black – Gaussian beam) 71
3.51 Power profile of the beam at $z = 600\,\text{mm}$ (blue – R_X; red – T_X; black – Gaussian beam) 71
3.52 Power profile of the beam at $z = 1200\,\text{mm}$ (blue – R_X; red – T_X; black – Gaussian beam) 71
3.53 Beamwidth of the antennas in H-plane (solid curve – calculations; * – transmitting antenna; ° – receiving antenna) 72
3.54 Beamwidth of the antennas in E-plane (solid curve – calculations; * – transmitting antenna; ° – receiving antenna) 72
3.55 Configuration of the radar-sensor beams 73
3.56 Outlook of the bistatic double-frequency radar-sensor 74
3.57 Spectrum of the signal reflected from sand particles: K_a-band channel – a), W-band channel – b) 74
4.1 Experimental set-up configuration 79
4.2 Outlook of the experimental set-up 80
4.3 Screw dispenser configuration 81
4.4 Outlook of the screw dispenser 81
4.5 Powder consumption dependency on screw conveyer speed 82
4.6 Ejecting dispenser configuration 83
4.7 Ejector configuration 84
4.8 Outlook of ejecting dispenser 85
4.9 Particle consumption vs. particle supply velocity 85
4.10 Particle ensemble separation into fractions 87
4.11 Uniform particle size distribution of sieved fraction: probability density function – a), cumulative distribution function – b) 87

4.12 Particle size distribution for the powders under test according to Table 4.3: cumulative distribution function – a), probability density function – b) 88
4.13 Outlook of the fused alumina (Al_2O_3) grains F080 89
4.14 Sieves used for sand fraction separation – a), sand particles – b) 89
4.15 Configuration of the radar-sensor calibration 93
4.16 Spectrum of signal reflected from a calibrating sphere 93
4.17 Spectra of signals reflected from disperse streams 94
4.18 RCS dependence on particle mass loading 94
4.19 Dependence of coefficient $B(d)$ in (4.11) on mean particle size 95
4.20 Data comparison of remote sensing by a mono-frequency radar-sensor (Ver axis) and by contact measurements (Hor axis): mass loading – a), particle concentration – b) 96
4.21 Signal reflected in time domain: a) $\lambda_{min} = 3.23$ mm ; b) $\lambda_{max} = 8.16$ mm 98
4.22 Spectrum of signal reflected: a) $\lambda_{min} = 3.23$ mm ; b) $\lambda_{max} = 8.16$ mm 99

List of tables

3.1 Parameters of the coherent bistatic radar in the 3mm wave band 41
3.2 Double-reflector asymmetrical antenna parameters 58
3.3 Parameters of the monostatic radar-sensor 64
3.4 Parameters of antenna beam convergence 73
3.5 Parameters of the double-frequency radar-sensor 75
4.1 Parameters of powder consumption for screw dispenser 82
4.2 Consumption parameters of the ejecting dispenser 86
4.3 Parameters of sedimentary powders 88
4.4 Parameters of sieved powders 89
4.5 Physical properties of the materials under test 90
4.6 Comparison of remote and contact measurements 100

Introduction

Atmospheric pollution is one of serious risk factors for human health [1]. Nevertheless, millions of tons of solid aerosols (asbestos, carbon dust, heavy metals, etc.) precipitate on the territory of Europe annually. Furthermore, industrial emissions which are basically generated by fuel-burning power plants, metallurgical and cement works contribute no less than 25% to the total air pollution. Therefore the European Union has established strict standards for the amount of industrial emissions [2]. Moreover, creation and development of methods of remote sensing for disperse streams of solid particles for industrial emission monitoring is rather an **actual problem**.

At present, many types of sensors based on contact methods and remote sensing have been developed for monitoring solid particles in atmosphere. Some of them provide high measurement accuracy in a wide range of particle size, however, they do not permit measurements in large volumes. Therefore, they cannot be used for remote sensing in the case of industrial emission monitoring, which seriously restrict the application area of these methods. Hence sensors based on remote methods of sensing, which enable measurement in large volumes, are most applicable in this case.

Existing sensors for remote measurements basically use optical methods and hence the measuring volume is restricted by the dimensions of an optical beam; it does not exceed $\approx 10^{-5}\,\mathrm{m}^3$. Therefore it is necessary to use a multi-channel sensor to study spatial volumes $\geq 1\,\mathrm{m}^3$, which makes the sensor more expensive and complicated.

Thus **the research task** of the presented work is the development of methods for remote sensing of disperse streams of solid particles by using a coherent radar for reconstructing the parameters of the disperse stream by applying output signal processing.

To achieve the mentioned research task, the **following problems** have been solved:

- Processing algorithms of output signals from mono-frequency and double-frequency radar-sensors are developed for measurement of disperse stream parameters, including mass loading, effective particle dimension, and particle concentration;
- Millimeter wave radar-sensors are developed on the base of mono-frequency and double-frequency configurations for remote measurement of the disperse stream parameters including: mass loading, effective particle dimension, and particle concentration;
- An experimental set-up for full-scale studying of the characteristics of the designed radar-sensors is developed;

- Data comparison of contact measurement and remote sensing of disperse stream parameters is performed, which confirms the validity of the proposed methods for radar sensing and permits to estimate the limits of their application.

Object for study – phenomenon of radar signal scattering by ensembles of solid particles

Subject for study – methods and instruments for measuring parameters of a disperse stream of solid particles.

Methods of study: In this work, the following methods were used: theoretical methods of electromagnetic wave scattering by spherical dielectric particles, methods of statistical processing of experimental results, digital methods of radar signal processing, methods of radar system and antenna design.

The novelty of the study performed is characterized by the following results which have been obtained for the first time:

- A method for measurement of mass loading and particle concentration in disperse streams on the base of a coherent mono-frequency radar-sensor is proposed and studied for polydisperse streams with given distribution law of particle size.
- A method for measurement of mass loading, modal value of particle diameter, and particle concentration is proposed for polydisperse streams with narrow and wide particle size distribution using a double-frequency coherent radar-sensor.
- It has been shown that approximate concepts of single scattering and particle sphericity both provide good agreement of remote sensing data with contact measurements. The measurement error is less than 15% for mass loading and effective dimension of particles, and does not exceed 30% for particle concentration.

The practical importance of the results obtained within the scope of the dissertation consist in the following:

- A bistatic radar-sensor with high spatial resolution and CW signal radiation is designed;
- A quasioptical antenna feeder system with passive duplex device is designed to provide an operation of the radar-sensor transceiver using common antenna in CW mode;
- The mono-frequency and double-frequency radar-sensors are developed to provide measurement of mass loading, modal value of particles diameter, and particle concentration in disperse streams in air ducts.

Thesis arrangement

Chapter 1, **State of the art,** is dedicated to the analysis and choice of the field of study. The chapter provides an overview of existing methods of the particulate measurement. It shows that in spite of the high development level of the existing contact methods, they do not provide remote monitoring of atmosphere pollution. Furthermore, remote sensing based on the optical methods only permits measurements in quite small

spatial volumes $\approx 2 \cdot 10^{-5} \mathrm{m}^3$. Hence the development of remote sensing of disperse streams based on the application of a coherent radar is chosen as the main subject of inquiry. This method provides measurements in large volumes, at long distances, and practically does not depend on optical visibility.

In the first section of Chapter 2, **Theoretical background,** the radar equation for volume scatterers is discussed for a bistatic configuration of the radar-sensor, and illumination of the scattering volume is calculated for a Gaussian radiation pattern of the antenna. The second section of the chapter is devoted to a mono-frequency sounding method which permits measurement of mass loading of disperse streams and allows to estimate the number of particles when the particle size is available. The last section presents a double-frequency sounding method which permits to reconstruct the main physical characteristics of disperse streams: the particle size, the particle concentration, and the mass loading for both the monodisperse and the polydisperse medium. The numerical simulation and estimations of measurement accuracy are also provided, as well as applicability limits of the proposed methods.

Chapter 3, **Development of radar-sensors for remote sensing of disperse streams,** address design and realization of the millimeter wave radar-sensors. The first section of the chapter describes a bistatic radar-sensor designed for operation at W-band, and signal processing techniques including spectrum analysis and correlation analysis. Furthermore, the design and realization of a monostatic radar-sensor is given. It is focused on the realization of a quasioptical duplex antenna system. Finally, the last section presents design and realization of a double-frequency bistatic radar-sensor operating at K_a- and W-band. For all three sensor configurations, simulations and measurements are also provided.

Chapter 4, **Experimental study of sounding methods of disperse streams,** is devoted to the measurement and analysis of the experimental data. The chapter starts with describing an experimental set-up for the study of disperse stream parameters. The first section of the chapter also describes the design and characteristics of particle dispensers used in the experiments as well as the properties of the powder materials under test. The second part of the chapter presents a comparison of the data obtained by contact measurements and by remote sensing of a disperse stream. These results confirm the validity of the proposed method using a mono-frequency and a double-frequency radar-sensor.

Finally, the thesis concludes with a **summary** of the work presented through the four chapters of the manuscript. In this way, in the very last section of the document, the main achievements and results are recalled to the reader to give a concise but precise review of the work done.

Chapter 1

State of the art

The control of air pollution is one of the most important problems of modern society, which strongly influences human health [1]. The First Air Control Act was adopted in several European countries and in the USA in 1950s, to provide regulations for the control of industrial emissions. Since then a number of air protection programs and resolutions [2] were passed, which promoted an extensive research of different methods of particulate monitoring. Up to date, a great number of different methods for measuring different particulate characteristics are developed. Some of the first methods used in industrial emission control have been taken over from microscopic image analysis [3], sieving [4], and sedimentary analysis [5]. Other methods, including sedimentary settling velocity method [5], optical beam scattering and absorption [4] etc., are used in colloid chemistry for analysing particulate characteristics of disperse systems.

All of these methods can be classified into two big classes: contact methods, which require air sampling, and remote methods, which provide measurements of disperse stream parameters distantly. Contact methods are based on particle sampling from air [4] using different filtering systems. For example, one of the simplest contact methods permits to estimate particle size distribution using optical or electronic microscopic analysis [3] (Figure 1.1). This gives the most authentic data about the structure, form, and size distribution of the particle ensemble from an air sampler. To do so, the particles under test are fixed on a film by a special solution. As a development of the method, a digital camera can be used for image processing in a PC, which permits to automatize the process of the particle analysis. In spite of simplicity, this method provides the measurement of the particle size spectrum in quite a wide range, starting from parts of microns up to thousands of microns. However, this method has some disadvantages – low measurement rate and high labor content.

Figure 1.1 Optical microscope

a)

b)

Figure 1.2 Set of sieves – a) and mechanical shaker –b) used for sieving analysis

The sieve method [4] consists in sequential sieving of the particles through a set of sieves with different mesh sizes (Figure 1.2a). Then every fraction is weighted, the number of particles in every fraction is calculated, and the particle size distribution is plotted. The sieving process can be automatized [4] using a mechanical shaker – Figure 1.2. To estimate the mass loading, which determines the air pollution rate, it is necessary to use an appropriate calibration. The main advantages of the method are its simplicity and the ability of direct measurement. However, the applicability of the sieve method is restricted by coagulation of small particles, which does not permit to apply the method for particles less than 50 μm in size. The sieve method can be realized for both dry particles and particles suspended in liquid.

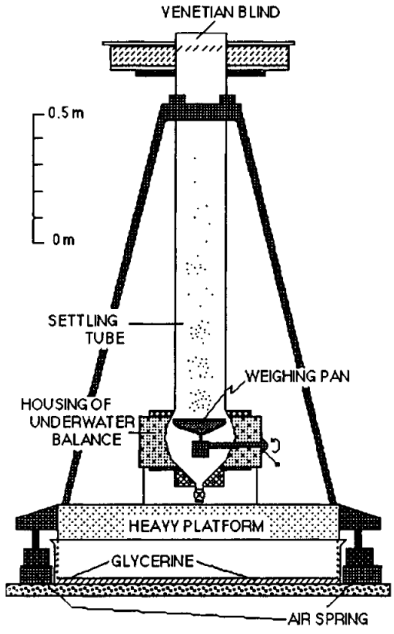

Figure 1.3 Configuration of sedimentary method (after Slot R.&Geldof H. (1979). Design Aspects and Performance of a Settling Tube System. Laboratory of Fluid Mechanics, Delft University of Technology Internal Report no. 6-79: 18pp.)

The sedimentary analysis [5] of a particle ensemble is based on the dependence of the particle size on the settling velocity in air or liquid. The device (Figure 1.3) includes a settling tube with a balance for weighting the particle sediment over a period of time. The method permits to estimate the particle size distribution, is applicable over a wide range of particle sizes (from parts to thousands of microns), gives high resolution, and needs less time for analysis compared to the sieve method.

An aerodynamic method with a laser-Doppler velocimeter [6] is based on particle velocity measurement in transient state. The configuration of the method is shown in Figure 1.4. This set-up consists of a laser-Doppler velocimeter, an aerodynamic accelerator of particles, and an air sampler. Particle velocity primarily depends on the aerodynamic diameter of particles, which permits to measure particle size distribution in the range from several to hundreds of microns [6].

Another high-usage contact method is the triboelectric method of mass loading measurement [DURAG GROUP smart solution for combustion and environment, pp. 10 – 11], which is based on the measurement of the electrostatic charge formed by particles friction against a sensor probe (Figure 1.5). The sensor permits to measure the particle mass loading from 0.1 mg/m^3 to 1 kg/m^3 and can operate in a wide range of particle sizes starting from 0.3 µm. The continuous measurement can be easily carried out in automatic mode using this device. However, the mass loading is the only parameter which can be measured by this type of sensors. Moreover, the velocity of the disperse stream should be higher than 5 m/s.

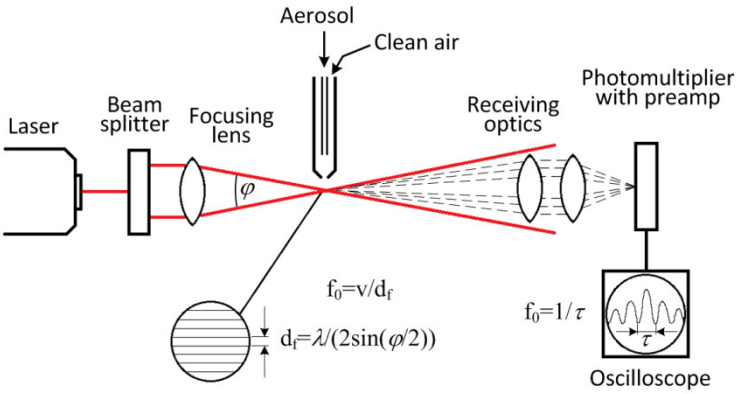

Figure 1.4 Configuration of laser velosimetry method [6]

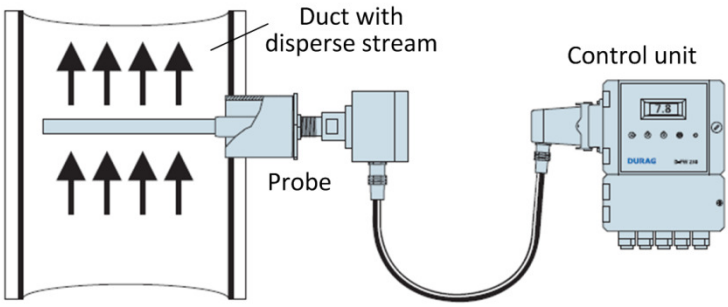

Figure 1.5 Configuration of triboelectric method

The methods mentioned above have a common disadvantage – they do not permit measurements of remote streams, which is usually required for industrial applications. From this point of view, the use of optical sensors is quite reasonable [7 – 10]. Many of such sensors are based on the particle ability to absorb or scatter electromagnetic waves.

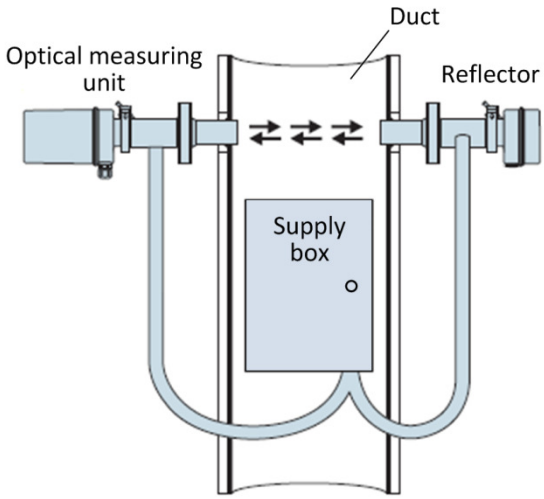

Figure 1.6 Configuration of light absorption method

Absorption of the optical beam is often used in sensors [7] which have their measuring area directly in a disperse stream. A transceiver unit (Figure 1.6) is superposed on the wall of the duct through which the disperse stream passes. Opposite to the optical transceiver, a plane reflector is placed in order to double the optical path through the stream. The extinction of the optical beam is proportional to the mass loading (g/m^3) of the stream. The device provides measurement of mass loading in the range of $1-400\ \mathrm{mg/m^3}$ and its measurement accuracy is about 1%.

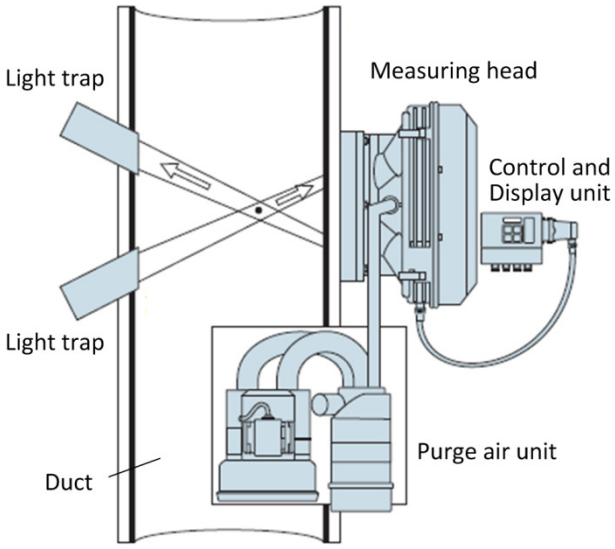

Figure 1.7 Configuration of light scattering method

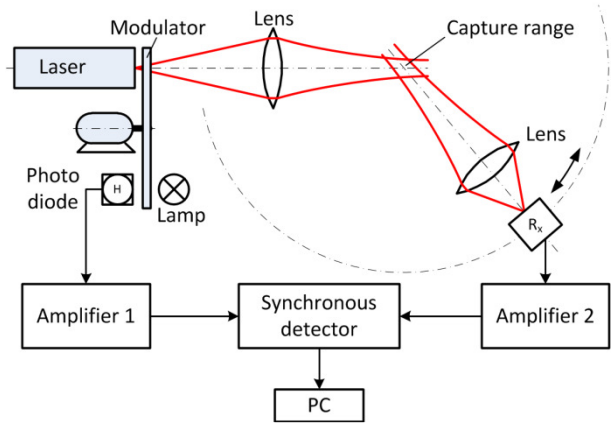

Figure 1.8 Configuration of scattering indicatrix method

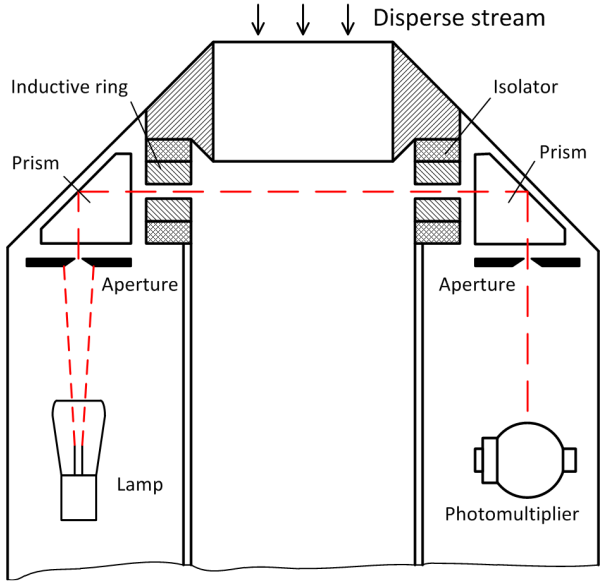

Figure 1.9 Configuration of light absorption method [9]

The scattering phenomenon is also used for measuring the mass loading of a disperse stream [4]. In this case, the transmitting and receiving units are placed side-by-side and focused at the same point (Figure 1.7). On the other side of the duct, the light traps are placed to avoid multiple reflections. A purge air unit is used for cleaning the stream particles in order to protect the optical sensors. Scattering of the optical beam is proportional to the mass loading of the disperse stream. This provides measuring the mass loading in the range of $0.01-300\,\mathrm{mg/m^3}$ with an accuracy of about 1%.

Another optical method based on light scattering permits to measure the particle size distribution by using the dependence of a scattering indicatrix on the particle size [8]. In this case (Figure 1.8), a HCN-laser ($\lambda=337\,\mu\mathrm{m}$) illuminates the particles of the disperse stream, and a pyro-receiver, which is moving around the stream in the cross-section, measures the width of the scattering indicatrix. A modulator provides the operation of amplifier 2 with the alternative current. Amplifier 1 is charged by a photo diode to provide a reference channel. A synchronous detector combines the two signals from both amplifiers. Signal processing is performed in a PC and provides measurement of the effective particle size in a range of 80 – 100 µm and particle concentration up to 1400 $\mathrm{cm^{-3}}$.

A simple device for the study of liquid aerosols is described in [9]. An optical beam from a lamp (Figure 1.9) is collimated, passes through the duct with the disperse stream, and enters a photo-multiplier. A stream particle passing through the beam causes attenuation which is proportional to the particle cross-section.

Therefore, by measuring the amplitude distribution of the pulses from the photo-detector output, it is possible to obtain the particle size distribution. This device provides measurement of the comparatively large particles in the range of 0.5 – 5 mm with an accuracy of less than 15%.

An interesting device based on the laser diffraction method is described in [4] and [10]. The device uses the effect of light scattering at the edge of a particle. A mono-chromatic light beam is diffracted by a particle and diverges at a diffraction angle θ which depends on particle size (Figure 1.10). Then the diffracted beam passes through the lens at focal distance F and enters the photo-detector matrix where the linear deviation $s = \theta \cdot F$ is registered. Hence the smaller the particle, the wider is the diffraction angle and the larger is the deviation s. In such a way, one can estimate the particle size distribution. Despite some technical problems, the method provides a range of particle size measurement starting from 0.1 µm up to 1 mm.

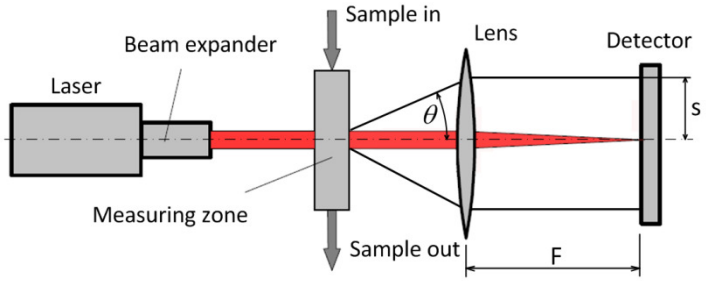

Figure 1.10 Conception of laser diffraction method [10]

A common disadvantage of the optical methods mentioned above is their quite small measuring area $\approx 10^{-5}$ m^3 which is limited by the cross-section of the optical beam. Another substantial disadvantage is the dependence on optical visibility (precipitation, fog, smoke etc.), which makes it impossible to measure opaque streams.

Therefore, it may be reasonable to utilise the radar technology in order to provide the measurement of disperse stream parameters under industrial conditions. Quite similar tasks are set in radio meteorology where radars have been used for sensing precipitations and dust clouds, which can be considered as disperse streams of bigger particles [11]. The work [12] is dedicated to the study of dust storm parameters using L-, S-, and X-band coherent pulse radars in Sahara desert. It is reported about the possibility to utilize the radar clutter depending on optical visibility in large spatial volumes of $\approx 10^3 - 10^4$ m^3.

Another approach has been realized in [13] for volcanic-cloud monitoring in Alaska in order to establish aircraft hazard warning. A mobile C-band radar was used for detecting ash clouds at a distance of about 80 km, in order to construct maps of the eruption columns and of the drifting ash clouds for short time periods (of about 30 minutes) after eruption. The radar gives direct information about active eruptions under any weather conditions, and it allows estimating the altitude of the column. This is useful for constructing three-dimensional trajectory models of ash-cloud transport. However, the long wavelength (10 cm) used does not permit to detect ash particles smaller than 100 µm in diameter, which are also drifting in volcanic clouds and staying in the atmosphere for several days or even longer.

Despite the possibility to detect disperse streams in large volumes, the radar methods mentioned above do not permit to reconstruct parameters of the stream. On the other hand,

such information can be very important for many practical applications including environmental monitoring, emission control of thermoelectric power plants, oil and gas industry, volcano eruption monitoring, and labour safety in technological processes which are connected with a high content of dust (like cement plants, ore mining and processing enterprises etc.).

Therefore, the development of a remote sensing method for solving the inverse problem of reconstructing the disperse stream parameters is of both great scientific interest and practical significance. It has hence been chosen as the main task of the present dissertation.

Chapter 2

Theoretical background

2.1 Properties of bistatic sensing of volume scatterers

The main task of disperse stream sounding is measurement of parameters of disperse streams (streams of solid particles, aerosols, smog, dust, etc.) by studying their electromagnetic wave scattering characteristics. In most cases, remote sensing methods are based on using the well known radar equation [14] which shows some peculiarities in the case of volume scatterers [15]. This equation is extensively used in radio meteorology for atmosphere and precipitation studies [11]. However, in the case of sensing industrial emissions, the dielectric parameters of solid particles, the size of the scattering volume, and the particle movement behavior significantly differ from typical parameters of the subject under test in radio meteorology.

Moreover, the size of homogeneous formations in disperse streams of industrial emissions is significantly smaller than the size of atmospheric precipitation. Therefore, in the case of industrial emission sounding, the requirements for the spatial resolution of a sensor are quite rigid: $\Delta V \le 1\,\mathrm{m}^3$. The technical realization of the radar-sensor with such characteristics is a rather complicated problem which requires using quite broadband sounding signals with bandwidth $\Delta f \ge 300\,\mathrm{MHz}$, which substantially complicates the measurement equipment and rises its price.

Therefore, it is suggested here to use a bistatic configuration of the radar [16] – Figure 2.1, for which a high spatial resolution is obtained by the interception of the transmitting and receiving antenna beams. Furthermore, it is necessary to estimate the equivalent radar cross-section (RCS) of the illuminated volume by taking into account the inhomogeneity of the disperse stream particle illumination.

2.1.1 Bistatic radar equation for volume scatterers

In the case of a point target in free space (Figure 2.1), the power received P_R at the receiving antenna of a bistatic radar can be expressed as [14]

$$P_R = P_T \frac{G_T G_R \lambda^2 \sigma}{(4\pi)^3 R_T^2 R_R^2} K_l, \tag{2.1}$$

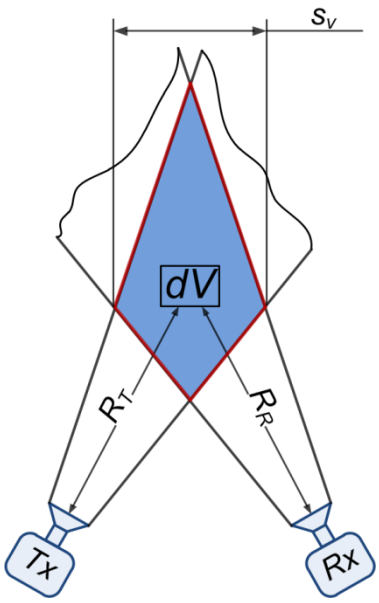

Figure 2.1 Bistatic radar configuration

where P_T – transmitting power, G_T and G_R – gain of the transmitting and receiving antennas, λ – operating wavelength, R_T and R_R – distance from a scattering element dV to the transmitting and receiving antennas, K_l – attenuation constant caused by the medium (in the cases under consideration, the attenuation is quite low: $K_l = 1$), σ – radar cross section (RCS).

Despite the simple form of the radar equation (2.1), its solution in the case of volume scatterers causes substantial difficulties, since it is impossible to find an exact expression for the RCS of the object under test σ, owing to the necessity of taking into account multiple scattering of the electromagnetic waves by disperse stream particles. Therefore, one must usually use different simplifying assumptions, in particular, the assumption of just single scattering [15], when multiple reflections can be neglected. For that, as is shown in [14], it is necessary to meet the condition: $N_0 \sigma_t s_V << 1$ – Figure 2.1 (N_0 – number of particles in the volume unit; σ_t – total scattering cross section of a single particle; s_V – linear size of the scattering volume $V \approx s_V^3$). In the case under consideration for remote sensing of solid particles, this inequality usually holds true $N_0 \sigma_t s_V \approx 10^{-4} - 10^{-3}$ ($N_0 \approx 10^6 - 10^8$ [12, 17], $\sigma_t \approx 1 \cdot 10^{-12}\,\mathrm{m}^2$, $s_V \le 10^2 - 10^3\,\mathrm{m}^2$), which permits to express the received power as the sum of the signal powers reflected from the individual particles $P_R = \sum_{i=1}^{N_T} P_i$. However, taking into account the huge amount of particles in a volume unit $N_0 \approx 10^6 \div 10^8$, it is advisable to substitute the signal summation by an integration over the scattering volume (Figure 2.1):

$$P_R = P_T \frac{\lambda^2}{(4\pi)^3} \int_V dV \frac{G_T(\vec{R}_T) G_R(\vec{R}_R)}{R_T^2 R_R^2} \sigma(V) \qquad (2.2)$$

Since particle disperse streams show very different sizes, it is preferable to use the mean value of the received power which can be obtained by averaging (2.2) over the particle ensemble by taking into account the given particle size distribution function $n_r(r)$ (particle amount in the range $r \in [r, r+\Delta r]$, where r – particle radius):

$$\langle P_R \rangle = \int_0^\infty dr\, n_r(r) P_R(r) = P_T \frac{\lambda^2}{(4\pi)^3} \int_0^\infty dr\, n_r(r) \cdot \int_V dV \frac{G_T(\vec{R}_T) G_R(\vec{R}_R)}{R_T^2 R_R^2} \sigma(r, V) \tag{2.3}$$

Hereafter, it is more convenient to use a normalized particle size distribution function $f_X(r) = \frac{n_r(r)}{N_0}$, which meets the condition of normalization – $\int_0^\infty dr\, f_X(r) = 1$. In other words, $f_X(r)$ is the probability density function (PDF) of the particle radius. Then changing the order of integration in (2.3) and expressing the gain coefficient in the form of – $G(\theta, \phi) = G_0 F^2(\theta, \phi)$ (G_0 – antenna gain along the pattern axis, $F^2(\theta, \phi)$ – antenna power pattern), the expression for the average power can be written as

$$\langle P_R \rangle = P_T \frac{\lambda^2 G_{0T} G_{0R}}{(4\pi)^3} \int_V dV \frac{F_T^2(\theta_T, \phi_T) F_R^2(\theta_R, \phi_R)}{R_T^2 R_R^2} N_0 \int_0^\infty dr\, f_X(r) \sigma_p(r). \tag{2.4}$$

where subscripts $_T$ and $_R$ correspond to the coordinate system of the transmitting and receiving antenna, respectively.

When the spatial resolution of the radar is high, one can assume that the statistical properties of the disperse stream are invariant within the scattering volume *V*. Consequently the expression (2.4) can be transformed into the simpler form

$$\langle P_R \rangle = P_T \frac{\lambda^2 G_{0T} G_{0R}}{(4\pi)^3} \sigma_0 V_{ef} \tag{2.5}$$

where V_{ef} – effective scattering volume:

$$V_{ef} = \int_V dV \frac{F_T^2(\theta_T, \phi_T) F_R^2(\theta_R, \phi_R)}{R_T^2 R_R^2} \tag{2.6}$$

σ_0 – specific RCS of the scattering volume:

$$\sigma_0 = N_0 \int_0^\infty dr\, f_X(r) \sigma_p(r). \tag{2.7}$$

and $\sigma_p(r)$ – RCS of a single particle.

Measuring the individual components of the equation (2.5) $\langle P_R \rangle$, P_T, λ^2, G_{0T}, G_{0R}, and V_{ef}, one can define the specific RCS value of the disperse stream under test:

$$\sigma_0 = \frac{\langle P_R \rangle}{P_T} \cdot \frac{(4\pi)^3}{\lambda^2 G_{0T} G_{0R}} \cdot \frac{1}{V_{ef}}, \tag{2.8}$$

which basically allows to study the disperse stream parameters.

2.1.2 Scattering volume of bistatic sensing

The effective scattering volume formation for the bistatic radar is presented in Figure 2.2. The radar antennas show identical needle-shaped power patterns with the

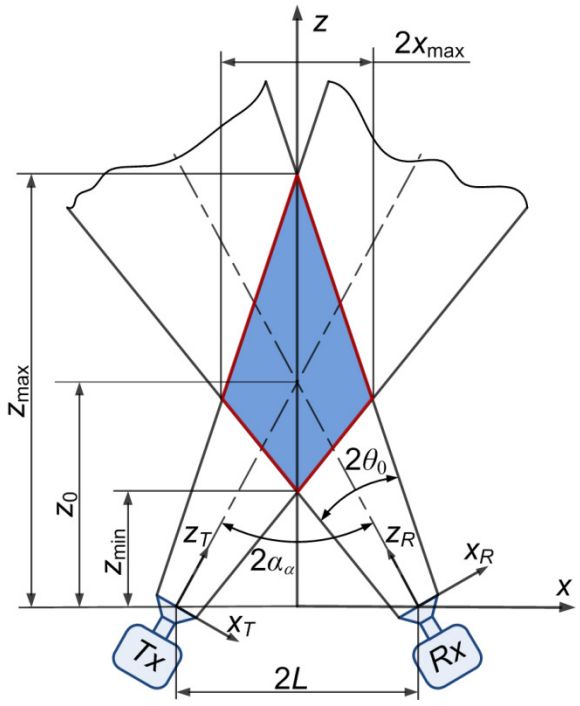

Figure 2.2 Geometry of a bistatic radar antenna system

half-power level beamwidth being equal to $2\theta_T = 2\theta_R = 2\theta_0$ and the antenna power gain – $G_{0T} = G_{0R} = G_0$. The convergence angle of the beams is denoted by $2\alpha_a$ which corresponds to the distance between the antenna phase centers – $2L$. The electrical axes of the antennas intercept at a distance of $z_0 = \frac{L}{tg\alpha_a}$. The values of $z_{\min}$ and $z_{\max}$ correspond to the minimum and maximum longitudinal coordinates of the effective scattering volume at an antenna field level of about ≈ -3 dB. In the same way, the value of $2x_{\max}$ defines the maximal dimension of the effective scattering volume in transversal direction.

Expressing the coordinates of the centers of the transmitting and receiving antenna apertures by x_R, y_R, z_R and x_T, y_T, z_T by the basic Cartesian coordinate system x, y, z, then considering sequentially the shift of the origin of the coordinate system by a distance L and its rotation by the angle of the beam convergence α_a, and leaving out lengthy transformations, the final expressions can be written as

$$\begin{aligned} x_R &= (x+L)\cos\alpha_a - z\sin\alpha_a; \\ y_R &= y; \\ z_R &= (x+L)\sin\alpha_a + z\cos\alpha_a; \\ \\ x_T &= (x-L)\cos\alpha_a + z\sin\alpha_a; \\ y_T &= y; \\ z_T &= -(x-L)\sin\alpha_a + z\cos\alpha_a \end{aligned} \tag{2.9}$$

The relation for the antenna power pattern in the far field, when an axisymmetric Gaussian field distribution is formed in the antenna aperture, is given by $E = E_0 \exp\left\{-\left(\frac{\rho}{\omega_0}\right)^2\right\}$ where $\rho = x_0^2 + y_0^2$ – transverse coordinate in a cylindrical coordinate system and ω_0 – Gaussian beamwidth in the antenna aperture defined by the power level decrease to $1/e$. According to Gaussian beam theory [18], the chosen field distribution provides the absence of side lobes (in the ideal case) and is convenient for calculating the field in any antenna beam section at a distance z from the antenna aperture:

$$E = E_0 \exp\left\{-\left(\frac{\rho}{\omega}\right)^2\right\} \tag{2.10}$$

$$\omega = \omega_0\sqrt{1+\left(\frac{2z}{k\omega_0^2}\right)^2} \tag{2.11}$$

where $k = \frac{2\pi}{\lambda}$ – wave number. The polar angle in the cylindrical coordinate system is equal to $\tan\theta = \frac{\rho}{z}$. Substituting this expression in (2.10) and taking into account that $\tan\theta \approx \sin\theta$, the expression for the power pattern can be given as

$$F = F_0 \exp\left\{-\left(\frac{z}{\omega}\sin\theta\right)^2\right\} \tag{2.12}$$

and the pattern width at the field level of $1/e$ is defined by $\sin\theta_e = \frac{\omega}{z}$. In the case when the distance from the antenna aperture to the object under test exceeds the beamwidth in the aperture $z >> \frac{k\omega_0^2}{2}$ (far-field condition for a Gaussian aperture), the number 1 under the radical in the expression (2.11) can be neglected owing to the large value of $\left(\frac{2z}{k\omega_0^2}\right)^2$. As a result, the expression for power pattern and beamwidth does not depend on the distance z:

$$F = F_0 \exp\left\{-\left(\frac{k\omega_0}{2}\sin\theta\right)^2\right\}. \tag{2.13}$$

According to the experimental results given in [19] and [20], and in order to form such Gaussian power pattern, it is necessary to fulfill the condition under which the antenna aperture size is essentially larger than the beamwidth $D_A >> \omega_0$, and the energy "overflow" is minimal, which corresponds to an illumination at the edge of the antenna aperture with power level not exceeding -20 dB.

Passing on to the Cartesian coordinates in the expression for the effective scattering volume (2.6), one obtains

$$V_{ef} = 4\times \int_{z_{\min}}^{z_{\max}} dz \int_0^{x_{\max}} dx \int_0^{y_{\max}} dy \frac{F_T^2 \cdot F_R^2}{R_T^2 \cdot R_R^2}. \tag{2.14}$$

Then the distances in the spherical coordinate system ($R_{R,T}$, $\vartheta_{R,T}$, $\phi_{R,T}$) may be expressed by $R_{R,T} = \sqrt{x_{R,T}^2 + y_{R,T}^2 + z_{R,T}^2}$.

2.1.3 Illumination of the scattering volume

An analytical evaluation of expression (2.14) obviously causes difficulties. Hence the calculation of the effective scattering volume (2.10 – 2.14) has been performed using numerical simulation. As an example, Figure 2.3 shows normalized distributions of the effective scattering volume illumination along the longitudinal coordinate z $(x=0, y=0)$ for the following parameters: ω_0=15.5 mm, λ=3.23 mm, L=35 mm, and different values of beam convergence angle α_a= 1.5, 2.5, and 3.5 deg. As can be seen, the illumination distributions are asymmetrical with respect to the distance of beam interception $z = z_0$, and shifted to the region $z/z_0 < 1$ owing to the space propagation factor in (2.1) which is proportional to $\approx R^{-4}$.

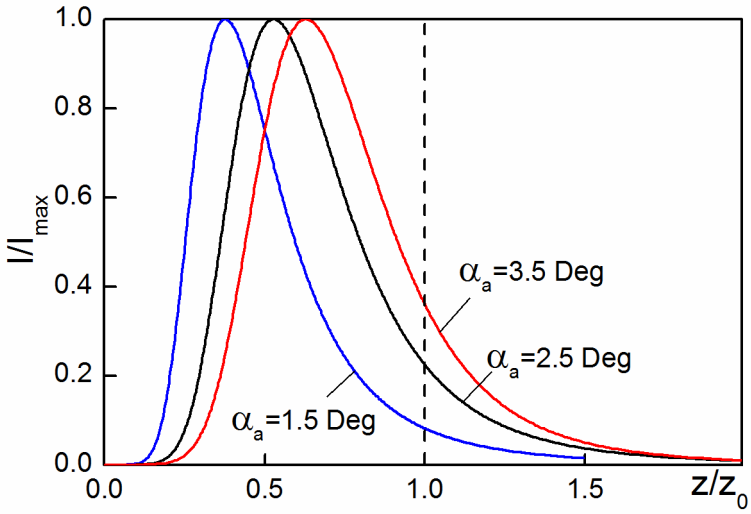

Figure 2.3 Illumination of the effective scattering volume

As the numerical estimation indicates, the model of forming the illuminated volume provides a spatial resolution value of about $\Delta z \approx 0.4 z_0$. The size of the effective scattering volume in vertical plane is close to the linear size of the antenna power pattern when the distance between the antennas is approximately equal to the aperture size $L \approx D_A$.

For the technical realization of the proposed radar-sensor configuration, it is important to choose correct parameters of the effective scattering volume such as the width of the antenna power pattern $2\theta_0$ and the convergence angle of the antenna beams α_a.

The signal power reflected from a volume scatterer (2.5) is determined as $\langle P_R \rangle \approx G^2 \cdot \lambda^2 \cdot V_{ef}$, and should increase proportionally to D_A^4, since $G \propto D_A^2$ [21]. On the other hand, the received power also depends on the scattering volume, the value of which varies according to the shape of the antenna pattern and, consequently, of the antenna gain. Hence an analytical estimation of the optimal characteristics of the antenna is quite complicated. That is why the normalized signal-to-noise ratio (SNR – $\Pi = G^2 \lambda^2 V_{ef}$) has been simulated in dependence on the Gaussian beamwidth in the antenna aperture ω_0 for different convergence angles – Figure 2.4.

As one can see, an increase of the antenna directivity leads to a degradation of the reflected signal because the illumination maximum is shifted outwards of the antennas and the effective scattering volume decreases due to the space propagation factor which is proportional to $\frac{1}{R^4}$. However, for higher directivity ($\frac{\omega_0}{\lambda} \geq 5...10$), the increase of the antenna gain ($\propto D_A^4$) compensates the scattering volume decay and increases the SNR.

Consequently, the calculated data permit to recommend the value of the convergence angle being in the range of $2\alpha_a = 1° - 3°$.

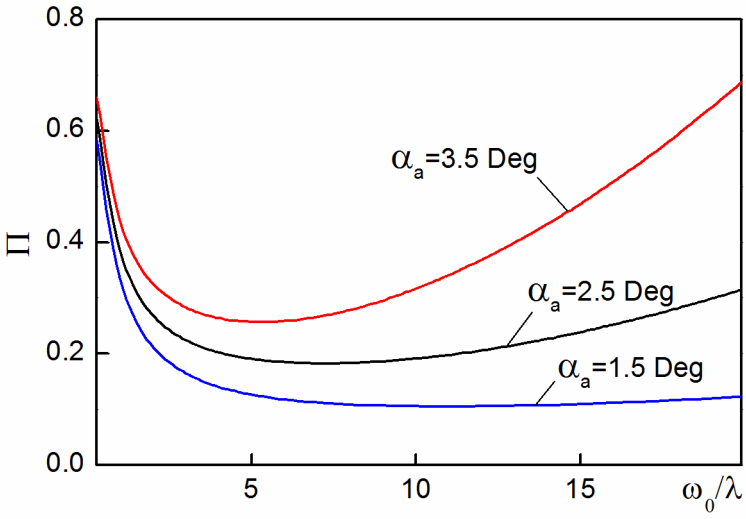

Figure 2.4 Normalized signal-to-noise ratio for a volume scatterer

In particular, the analysis carried out for the parameters $\omega_0 = 15.5$ mm; $\alpha_a = 2.5$ Deg; $\lambda = 3.23$ mm; $L = 35$ mm shows that the range resolution equals 1.68 m in the longitudinal section and 0.24 m in the cross-section at a power level of -20 dB. Hence the considered bistatic radar configuration permits to realize quite a high spatial resolution in easy way, without using a compound signal in CW mode. Moreover, this radar configuration provides a rather high isolation between the transmitting and receiving antennas, which is important for radar operation in CW mode.

2.2 Mono-frequency sounding of disperse streams

2.2.1 Sounding of monodisperse streams

The equations presented above contain information about the characteristics of volume scatterers. In fact, the shape of small solid particles comparatively to the operating radar wavelength can be considered as spherical. Hence the RCS of a single particle with radius r can be written using the Rayleigh approximation [11, 15] as

$$\sigma_p = \frac{128\pi^5}{3}\left|K_\varepsilon\right|^2 \cdot \frac{r^6}{\lambda^4}\ ; \quad \left|K_\varepsilon\right|^2 = \frac{\left(\varepsilon' - 1\right)^2 + \varepsilon''^2}{\left(\varepsilon' + 2\right)^2 + \varepsilon''^2}, \tag{2.15}$$

where ε' and ε'' – real and imaginary parts of the complex dielectric permittivity $\dot{\varepsilon} = \varepsilon' - j\varepsilon''$.

It is necessary to take into account, that a disperse stream usually contains particles of different size – so called polydisperse stream, special case of which is a monodisperse stream (Figure 2.5a). The polydisperse stream is characterized by a mode of the distribution (modal radius r_{mod}) which corresponds to the maximum of the probability density function (PDF) (Figure 2.5b), and by a distribution width Δr which characterizes the dispersion of the

particle radius. In practice, a normalized distribution width is often used. It equals the ratio of the distribution width to the modal radius: $\overline{\Delta r} = \dfrac{\Delta r}{r_{\text{mod}}}$.

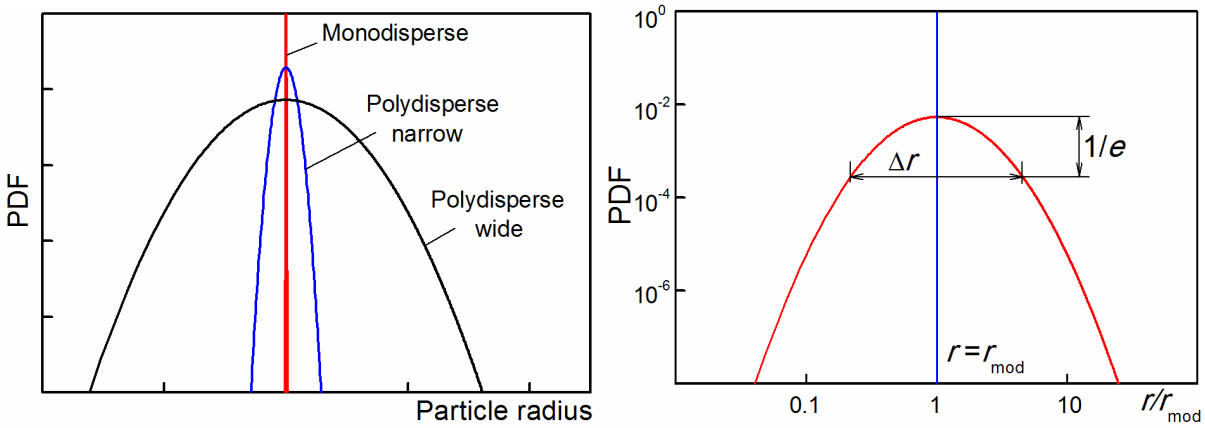

a) b)

Figure 2.5 Particle size distribution: a) – distribution type; b) parameters of distribution

In order to estimate the characteristics of a disperse stream, a log-normal distribution law is used, which is widely applicable for describing the properties of disperse streams of artificial and natural origin [12, 17]:

$$f_X(r) = \frac{1}{r\, g\sqrt{2\pi}} \exp\left\{-\frac{1}{2}\left(\frac{\ln r - \ln s_r}{g}\right)^2\right\}, \tag{2.16}$$

where s_r and g – parameters of distribution. As a numerical characteristic of a distribution law, the moments of distribution are widely used $m_k = \int_0^\infty dr r^k f_X(r)$. Then substituting (2.15) into (2.7), the specific RCS of a particle ensemble can be expressed through the 6th moment $m_6 = \int_0^\infty dr\, r^6 f_X(r)$ of the particle size distribution:

$$\sigma_0 = \frac{128\pi^5}{3\lambda^4}\left|K_\varepsilon\right|^2 \cdot N_0\, m_6 . \tag{2.17}$$

On the other hand, a mass loading M (g/m^3) is determined as the 3rd moment of the particle size distribution [14]:

$$M = \frac{4\pi}{3}\rho_p \cdot N_0\, m_3; \qquad m_3 = \int_0^\infty dr\, r^3 f_X(r). \tag{2.18}$$

where ρ_p – density of particle material (g/m^3). Leaving out the particle concentration N_0 from (2.17) and (2.18), one can show that the particle mass loading M is proportional to the specific RCS σ_0 and a ratio of the moments $\gamma = \frac{m_3}{m_6}$:

$$M = \frac{\rho_p \lambda^4}{32\pi^4 \left|K_\varepsilon\right|^2} \cdot \gamma \cdot \sigma_0 . \tag{2.19}$$

The particle concentration is equal to:

$$N_0 = \frac{3M}{4\pi \rho_p \cdot m_3} . \tag{2.20}$$

Consequently, if the distribution law is known (for instance, for streams of known origin), the expressions (2.19) and (2.20) permit to calculate the most important parameters of the disperse stream. In the case of a monodisperse medium: $f_X(r) = \delta(r - r_0)$, where $\delta(r)$ – Dirac delta-function, all particles have the same radius $r \equiv r$, so that the moment of k^{th} order is equal to: $m_k = r^k$ and the moment ratio is inversely proportional to the cube of the particle radius: $\gamma = r^{-3}$. Taking into account the calculations mentioned above, the expression for the disperse stream mass loading (2.19) becomes much simpler:

$$M = \frac{\rho_p \lambda^4}{32\pi^4 \left|K_\varepsilon\right|^2} \cdot r_0^3 \cdot \sigma_0 . \tag{2.21}$$

Therefore, the expression (2.21) provides calculating the mass loading by measuring the specific RCS of particles σ_0 for a given radius r_0 which may be estimated by contact measurements. The data obtained are valid only for a monodisperse medium, but in the case of a polydisperse stream, the situation is more complicated and requires special considerations.

2.2.2 Sounding of polydisperse streams

Also using the relations (2.20) derived above for the case of a polydisperse medium, an evaluation error of the disperse stream parameters arises. Moreover, the wider the distribution law of the particle size, the bigger is the error. For the log-normal distribution its mode r_{mod} can be defined by

$$\frac{\partial f_X}{\partial r} = \frac{1}{g\sqrt{2\pi}} \cdot \frac{\exp\left[-\frac{\left(\ln r - \ln s_r\right)^2}{2g^2}\right]}{r^2} \left[1 + \frac{\left(\ln r - \ln s_r\right)}{g}\right]. \tag{2.22}$$

Leaving out simple transformations, the equation (2.22) can be written as $1+\left(\ln r-\ln s_r\right)\cdot g^{-2}=0$, and its solution has a simple form:

$$r_{\text{mod}}=s_r\cdot\exp\left(-g^2\right). \tag{2.23}$$

Substituting (2.23) into (2.16), the maximum value of the PDF is found as

$$f_X^{\max}=f_X\left(r_{\text{mod}}\right)=\frac{\exp\left(\frac{g^2}{2}\right)}{s_r\,g\sqrt{2\pi}}. \tag{2.24}$$

Then normalizing (2.16) by using (2.24), one can derive an equation for the distribution width at the level of $1/e$:

$$\frac{f_X\left(r_{1,2}\right)}{f_X^{\max}}=\frac{s_r}{r_{1,2}}\exp\left[-\frac{\left(\ln r_{1,2}-\ln s_r\right)^2}{2g^2}-\frac{g^2}{2}\right]=\frac{1}{e}, \tag{2.25}$$

so that the final expression can be written as

$$\Delta r=r_1-r_2=r_{\text{mod}}\left(e^{g\sqrt{2}}-e^{-g\sqrt{2}}\right). \tag{2.26}$$

Solving equations (2.23) and (2.24), dependencies for the distribution parameters s_r and g can be obtained in the form

$$s_r=r_{\text{mod}}\exp\left\{\frac{1}{2}\ln^2\left[\frac{\overline{\Delta r}}{2}+\sqrt{1+\left(\frac{\overline{\Delta r}}{2}\right)^2}\right]\right\}; \tag{2.27}$$

$$g=\frac{1}{\sqrt{2}}\ln\left[\frac{\overline{\Delta r}}{2}+\sqrt{1+\left(\frac{\overline{\Delta r}}{2}\right)^2}\right] \tag{2.28}$$

where $\overline{\Delta r}$ – normalized distribution width. The expressions (2.27) and (2.28) permit to find the values of the distribution parameters s_r and g by using the mode r_{mod} and the width $\overline{\Delta r}$ of the distribution law.

As an example, the function $f_X\left(r\right)$ in logarithmic scale is presented in Figure 2.6 for different values of the normalized width $\overline{\Delta r}$. As one can see, the distribution width increases owing to the contribution of large particles, which is important for understanding the scattering field forming [16, 22].

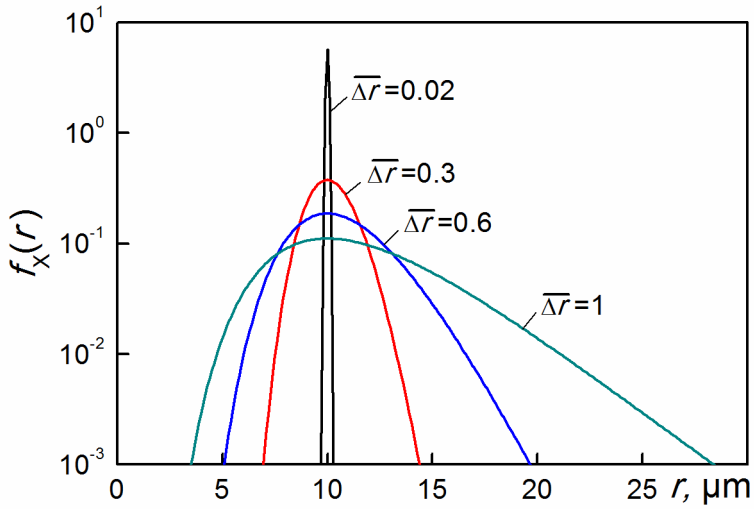

Figure 2.6 Log-normal particle size distribution

Turning back to the moment expression (2.17), it is necessary to note that the moment of k^{th} order equals $m_k = \exp\left(k \ln s_r + \frac{1}{2} k^2 g^2\right)$, according to [23]. Hence for better understanding of the subsequent analysis, it is advisable to express the distribution moment of k^{th} order in terms of its first moment $m_k = m_1^k \cdot \exp\left[\frac{1}{2} k^2 g^2 \left(1 - \frac{1}{k}\right)\right]$ which represents the mean value of the particle radius $m_1 = \bar{r}$. Then the ratio of the 3rd moment to the 6th can be expressed in the following form:

$$\gamma = \frac{m_3}{m_6} = \frac{1}{\bar{r}^3} \exp\left(-12 g^2\right). \tag{2.29}$$

The relative error of the moment ratio for a polydisperse medium γ_{poly} can be defined as: $\overline{\Delta\gamma} = \frac{\gamma_{poly} - \gamma_{mono}}{\gamma_{poly}} \cdot 100\%$. In Figure 2.7, the dependence of $\overline{\Delta\gamma}$ on the distribution width $\overline{\Delta r}$ is shown. As one can see, the error is still located within acceptable limits $\overline{\Delta\gamma} \le 30\%$ for relatively "narrow" distributions $\overline{\Delta r} \le 0.4$. In other words, if the distribution width is less than $\overline{\Delta r} \le 0.4$ and the mean value $\bar{r}$ is known (for a given particle source for instance), then such medium can be considered as monodisperse and the expressions (2.20) and (2.21) can be used for calculating values of mass loading and particle concentration.

However, if any a priori information about the particle distribution law is absent, it is still possible to use an empirical relation which is widely used in radio meteorology [11]. It can be written in the case under consideration as

$$\sigma_0 = A \cdot M^B, \tag{2.30}$$

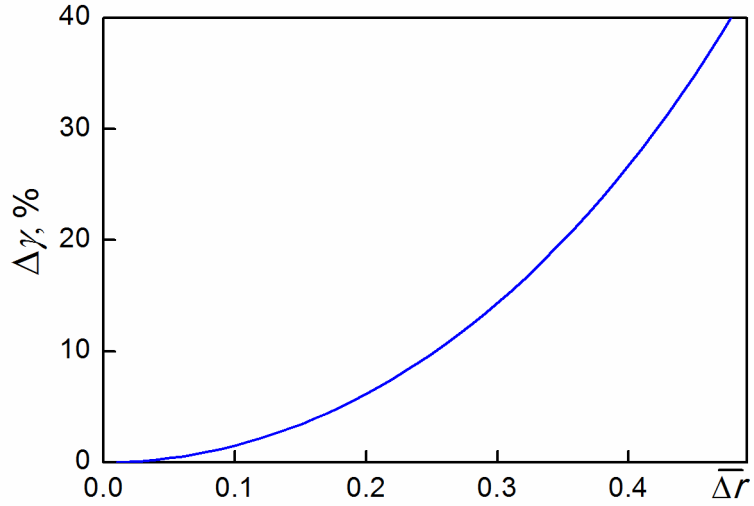

Figure 2.7 The relative error of the moment ratio for a polydisperse medium

where constants A and B must be determined experimentally. Referring to (2.21), constant $B=1$ and value $A=\frac{m_6}{m_3}\cdot\frac{32\pi^4\left|K_\varepsilon\right|^2}{\rho_p\,\lambda^4}$ depends on some parameters of the particle size distribution. Consequently if the information about the parameters of the distribution law is missing, a calibration of the radar is required, which permits to use expression (2.30).

If the particle size distribution law is changed, then it is necessary to establish a new radar calibration. Hence an approach based on using expression (2.30) is of interest if the distribution parameters are stable enough.

Therefore, the development of methods for measuring the disperse stream parameters with unknown distribution law is of substantial interest, and an attempt to solve this problem is made in section 2.3 by using a double-frequency sounding method.

2.3 Double-frequency sounding of disperse streams

2.3.1 Differential radar cross-section

As has been shown above, mono-frequency sounding permits to measure the mass loading and the concentration of solid particles if a priori information about the particle size distribution parameters is known. At the same time, the case of a polydisperse stream with beforehand unknown distribution parameters is also of great interest for practical applications.

The disadvantages of mono-frequency sounding are mainly caused by the multivariate nature of the problem. Consequently a mono-frequency radar cannot completely solve such problems in principle. For instance, in the case of a monodisperse stream, the reflected signal is characterized by the number and the size of the particles (2.16) $\sigma_0 \approx N_0\, r^6$. Therefore, even

in the simplest case, it is not possible to evaluate the parameters mentioned above separately without invoking any a priori information about the particle ensemble properties.

That is why the use of a double-frequency radar which can enhance the possibilities of remote sensing in principle is of interest. For the first time, the use of a double-frequency radar was proposed in paper [24] for determining the microphysical characteristics of precipitation. A further development of the method for remote sensing of solid particles is described in papers [25, 26]. Therefore, one should consider the peculiarities of the proposed method in more detail following paper [26], which is based on using the concept of differential RCS (DRCS) for volume scatterers:

$$\sigma_D = \frac{\sigma_0(\lambda_1)}{\sigma_0(\lambda_2)} = \frac{\int_0^\infty dr\, \sigma_p(r, \lambda_1, \dot{\varepsilon}_1) f_X(r)}{\int_0^\infty dr\, \sigma_p(r, \lambda_2, \dot{\varepsilon}_2) f_X(r)}. \tag{2.31}$$

The DRCS equals the RCS ratio at two different wavelengths $\lambda_1 = \lambda_{\min}$ and $\lambda_2 = \lambda_{\max}$ taking into account the frequency dispersion of the particle material permittivity $\dot{\varepsilon}(\lambda)$. Since the value of the DRCS does not depend on particle concentration N_0, it is possible to measure the mass loading by using relation (2.31). However, if wavelengths $\lambda_{\min}$ and $\lambda_{\max}$ are selected to be located in the Rayleigh scattering region $\lambda_{\min}, \lambda_{\max} >> r$, then the DRCS does not depend on particle size: $\sigma_D = \left(\frac{\lambda_{\max}}{\lambda_{\min}}\right)^4$ because the RCS is proportional to the particle radius in the form: $\sigma_0 \approx \frac{r^6}{\lambda^4}$. Therefore, the necessary condition is that at least one of the wavelengths has to be selected from the resonance scattering region $\lambda \cong r$, where the dependence of $\sigma_0 \propto \lambda^{-4}$ is violated. This essentially complicates, however, the calculation of the RCS, which must be calculated by using rigorous Mie theory for particles of spherical shape [27].

2.3.2 Application of Mie theory for calculation of the particle RCS

The class of electromagnetic scattering by a dielectric sphere [27] depends on the value of a diffraction parameter $\rho = \frac{2\pi r}{\lambda}$. If $\rho << 1$, Rayleigh scattering is taking place – Figure 2.8, and the RCS can be approximately calculated using relation (2.15). However, if the diffraction parameter is in the range $1 \le \rho \le 10$, the RCS must be calculated using expression [11]:

$$\sigma_p = \frac{\pi r^2}{\rho^2} \left| \sum_{n=1}^{\infty} (-1)^n (2n+1)(a_n - b_n) \right|^2 \tag{2.32}$$

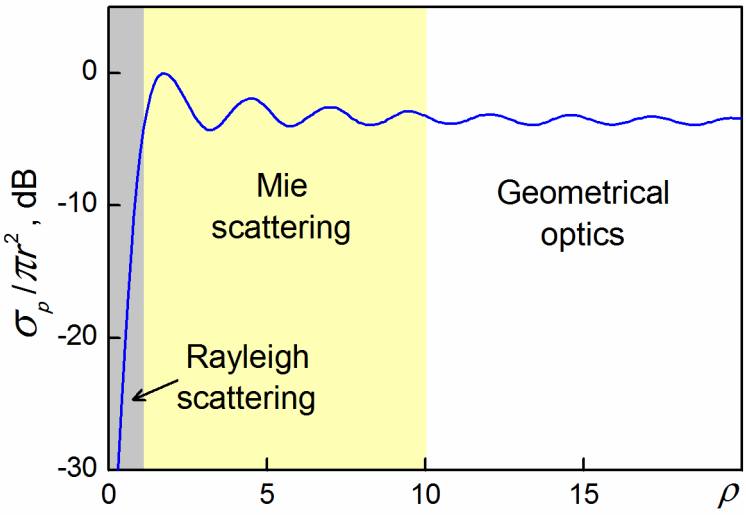

Figure 2.8 Type of scattering from dielectric particle

where a_n and b_n – complex expansion coefficients of the scattered field, the so-called Mie coefficients [27] which depend on the wavelength and the complex permittivity. If the diffraction parameter is essentially larger than unity, the radar cross-section does not depend on the diffraction parameter (Figure 2.8) and the geometrical optics approximation may be used [27].

In the case under consideration, the Mie coefficients are given by [23]:

$$a_n = \frac{\left(\frac{A_n(\dot{m},\rho)}{\dot{m}} + \frac{n}{\rho}\right)\cdot\psi_n(\rho) - \psi_{n-1}(\rho)}{\left(\frac{A_n(\dot{m},\rho)}{\dot{m}} + \frac{n}{\rho}\right)\cdot\varsigma_n(\rho) - \varsigma_{n-1}(\rho)}, \tag{2.33}$$

$$b_n = \frac{\left(A_n(\dot{m},\rho)\cdot\dot{m} + \frac{n}{\rho}\right)\cdot\psi_n(\rho) - \psi_{n-1}(\rho)}{\left(A_n(\dot{m},\rho)\cdot\dot{m} + \frac{n}{\rho}\right)\cdot\varsigma_n(\rho) - \varsigma_{n-1}(\rho)}, \tag{2.34}$$

where ψ_n and ς_n – Riccati-Bessel functions of the first and third kind, $A_n(\dot{m},\rho)$ – logarithmic derivative which is given by:

$$A_n(\dot{m},\rho) = \frac{\psi_n'(\dot{m}\rho)}{\psi_n(\dot{m}\rho)} = -\frac{n}{\dot{m}\rho} + \frac{J_{n-1/2}(\dot{m}\rho)}{J_{n+1/2}(\dot{m}\rho)}, \tag{2.35}$$

where $J_{n-1/2}$, $J_{n+1/2}$ – Bessel functions of the first kind with half-integer index and $\dot{m} = \sqrt{\dot{\varepsilon}}$ – complex refractive index.

As can be seen from (2.33) – (2.35), such representations of a_n and b_n require the calculation of the functions $A_n(\dot{m}\rho)$, $\psi_n(\rho)$, and $\varsigma_n(\rho)$. Only one of them $A_n(\dot{m}\rho)$ has a complex argument. Hence the Mie coefficients only depend on the diffraction parameter ρ and on the complex permittivity $\dot{\varepsilon}$. The expressions presented in (2.32) – (2.35) have been used for calculation and analysis of the DRCS in order to choose the wavelengths λ_1, λ_2 properly.

2.3.3 Application limits of double-frequency method

For determining the applicability range of the double-frequency method, it is necessary to consider the basic characteristics of the method by using numerical simulations of the scattering properties of a disperse stream [26]. Alternatively and approximately, one can utilize results obtained on the basis of a rigorous solution of the problem of diffraction by a dielectric sphere [27] using the algorithm described in [28].

In Figure 2.9, a typical example of a DRCS calculation is presented for the case of a monodisperse stream (distribution function $f_X(r) = \delta(r - r_0)$), value of permittivity $\varepsilon' = 10$, low dielectric loss $\varepsilon'' \to 0$, and a wavelength ratio $\alpha = \lambda_{\min}/\lambda_{\max} = 0.2$. In the region of the diffraction parameter $\rho > 2.5$, the DRCS dependence becomes ambiguous, which restricts the application of the proposed method – Figure 2.9.

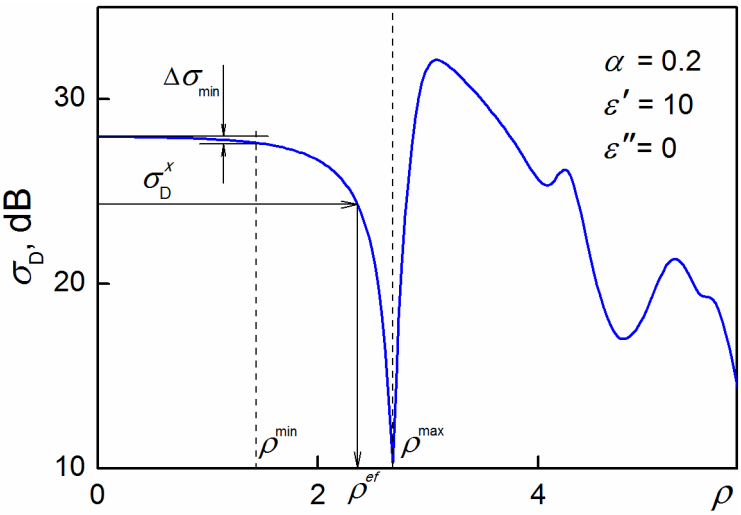

Figure 2.9 Typical dependence of the DRCS on the diffraction parameter

Nevertheless, one can always define a parameter region $\rho^{\min} \le \rho \le \rho^{\max}$, in which the DRCS dependence varies monotonically. The presence of the steadily decreasing section for values $\rho \le \rho^{\max}$ provides an unambiguous correspondence between the measured value of the DRCS σ_D^x and the effective value of the diffraction parameter ρ^{ef}. Furthermore, it should be noted that the selection of minimum and maximum operating wavelengths (in $\alpha = \lambda_{\min}/\lambda_{\max}$) has just a minor effect on the form of the DRCS dependence in the case of a monodisperse medium.

2.3.4 Sounding of polydisperse streams with "narrow" particle size distribution

A polydisperse nature of the disperse stream significantly alters the DRCS behavior. Figure 2.10 shows the results of numerical simulations of the DRCS for a disperse stream with log-normal particle size distribution and different distribution width $\overline{\Delta r}$. As can be seen from the figure, the change in distribution width leads to a measurement error compared to the true value of the modal parameter ρ_{mod}^{0}, which is the bigger, the wider the distribution width $\overline{\Delta r}$ is.

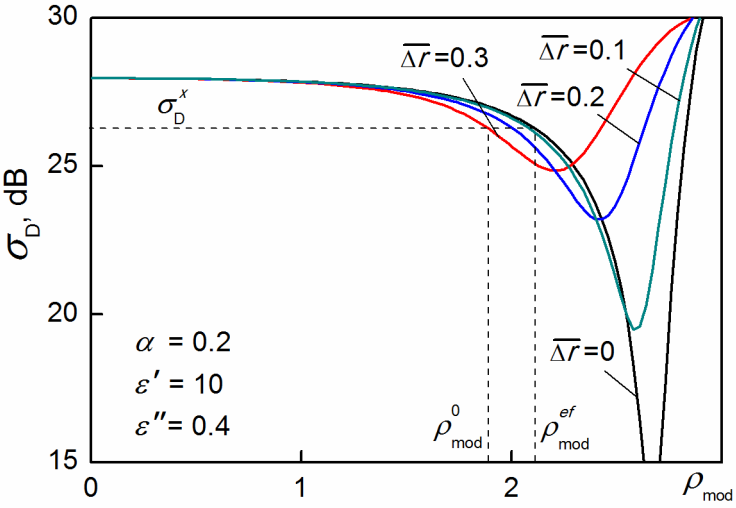

Figure 2.10 DRCS dependence for polydisperse stream

Nevertheless, for a sufficiently "narrow" particle size distribution with $\overline{\Delta r} < 1$ and a large value of the permittivity $|\dot{\varepsilon}| \geq 4$, the polydisperse medium can be approximately replaced by an equivalent monodisperse medium with an effective modal radius r_{mod}^{ef} of particles by solving the system of equations

$$\begin{cases} \sigma_D\left(\rho_{\text{mod}}^{ef}\right) = \sigma_D^x; \\ r_{\text{mod}}^{ef} = \dfrac{\lambda_{\min}}{2\pi\sqrt{|\dot{\varepsilon}|}} \cdot \rho_{\text{mod}}^{ef}, \end{cases} \tag{2.36}$$

where $\sigma_D\left(\rho_{\text{mod}}\right)$ – theoretical dependence of the DRCS for the equivalent monodisperse medium (Figure 2.10), σ_D^x – measured value of the DRCS, ρ_{mod}^{ef} – effective value of the modal diffraction parameter. The effective particle radius of the disperse stream calculated in accordance with (2.36) permits to estimate some important parameters including the effective particle concentration N_0 and the mass loading M [14 – 17]:

$$\begin{cases} N_0 = \dfrac{\sigma_0^x(\lambda_{\min})}{\sigma_p\left(\rho_{\text{mod}}^{ef}, \lambda_{\min}\right)}; \\ M = N_0 \cdot \dfrac{4\pi}{3}\rho_p \cdot \left(r_{\text{mod}}^{ef}\right)^3, \end{cases} \tag{2.37}$$

where $\sigma_0^x(\lambda_{\min})$ – specific RCS measured at wavelength $\lambda_{\min}$; $\sigma_p\left(\rho_{\text{mod}}^{ef}, \lambda_{\min}\right)$ – RCS of a single particle corresponding to the effective modal parameter ρ_{mod}^{ef} which is calculated in accordance with (2.36) and hence corresponds to the effective modal particle radius r_{mod}^{ef}.

The potentiality of the approach under consideration is, however, limited by the regime of an unambiguous measurement of the modal value of the diffraction parameter $\rho^{\min} \le \rho \le \rho^{\max}$ outside of which the DRCS dependence shows ambiguous character (Figure 2.9). The upper boundary of an unambiguous measurement of a polydisperse stream $r_{\text{mod}}^{\max}$ depends on the width of the distribution law, which significantly narrows the domain of applicability of the method under consideration. The estimates given in [26] show that the dependence of the effective modal particle radius can with sufficient degree of accuracy be approximated by the following expression:

$$r_{\text{mod}}^{\max}\left(\overline{\Delta r}\right) = r_{mono} - \frac{\lambda}{\pi\left|\sqrt{\dot{\varepsilon}}\right|} \cdot \left(\overline{\Delta r}\right)^{1,55}, \tag{2.38}$$

where $r_{mono} \le \dfrac{0.44\,\lambda_{\min}}{\left|\sqrt{\dot{\varepsilon}}\right|}$ – upper boundary of measurement for a monodisperse medium calculated using the relation $\rho^{\max} \le 2.76$ in the case of values of the real part of the permittivity exceeding 5: $\varepsilon' \ge 5$.

The lower boundary of the range $r_{\text{mod}}^{\min}$ corresponds to the flat region of the DRCS dependence (Figure 2.9). It depends on the achievable accuracy of the DRCS measurement $\Delta\sigma_{\min}$ according to the following equation:

$$40\lg\frac{\lambda_{\max}}{\lambda_{\min}} - \sigma_D\left(r_{\text{mod}}^{\min}\right) \ge \Delta\sigma_{\min}, \tag{2.39}$$

where the first term represents the asymptotic value of the DRCS for small particle radius $r \to 0$: $\lim\sigma_D(r) = \left(\lambda_{\max}/\lambda_{\min}\right)^4$ and the values of σ_D and $\Delta\sigma_{\min}$ are to be expressed in decibel.

As a result, the relative width of the unambiguous measurement regime amounts to ≈ 25 – 30% for the given example of a "narrow" distribution ($\overline{\Delta r} \le 0.3$). The analysis further

shows that an increase of the permittivity modulus reduces the width of the measurement regime. Furthermore, the difference between the effective value of the modal radius r_{mod}^{ef} and its true value r_{mod}^{0} does not exceed 15%: $\delta_r = \left| \frac{r_{mod}^{ef} - r_{mod}^{0}}{r_{mod}^{0}} \right| \le 15\%$.

Therefore, if it is a priori known that the distribution law is quite "narrow", then the application of the equivalent monodisperse medium is justified.

2.3.5 Sounding of polydisperse streams with "wide" particle size distribution

It has already been mentioned in section 2.2, that monodisperse streams are extremely seldom in practice. For this reason, characteristics of the DRCS for a lognormal particle size distribution of the disperse stream (Figure 2.6) (2.21 – 2.28) will be considered here.

The main peculiarity of electromagnetic wave scattering by a polydisperse stream consists in smoothing out the DRCS frequency dependence because of the averaging contributions from particles of different size. In contrast to the monodisperse medium, the character of the DRCS dependence substantially depends on the minimum to maximum wavelength ratio α: the bigger the difference, the bigger is the effect of smoothing. As an example, Figure 2.11 presents DRCS dependencies on the modal diffraction parameter $\rho_{\text{mod}} = \frac{2\pi\left|\sqrt{\dot{\varepsilon}}\right|}{\lambda_{\min}} r_{\text{mod}}$ for the lognormal particle size distribution of the disperse stream with various distribution widths $\overline{\Delta r} = \Delta r / r_{\text{mod}}$ ($\dot{\varepsilon} = 10 - j0.4$; $\alpha = 0.2$). As one can see from Figure 2.11a, an increase of the distribution width leads to a significant smoothing of the DRCS dependence due to decreasing resonance effects.

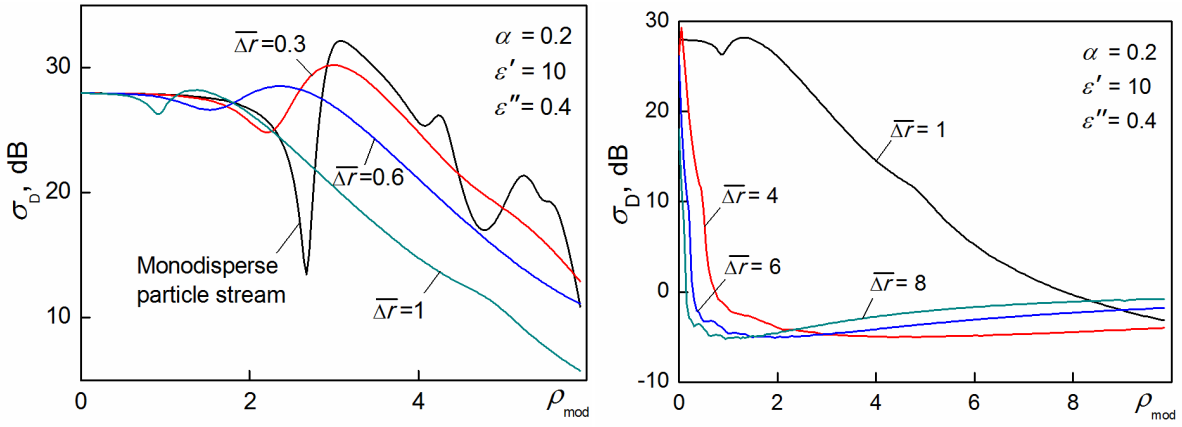

a) b)

Figure 2.11 DRCS dependence for polydisperse streams

Besides of that, the strong DRCS dependence on the distribution law, i.e. on the distribution width Δr – Figure 2.11a, does not permit to use the approach of a "narrow" distribution law considered above.

However, analyzing Figure 2.11b one can conclude that the character of the DRCS dependence remains almost the same for wide distribution width $\overline{\Delta r} \geq 4$, which permits to use another approach for the "effective" particle radius estimation. According to some experimental results given in [12] and [17], the relative width of all examined distributions is within a range $\overline{\Delta r} = 2 - 10$. Hence it is reasonable to choose the lognormal distribution law with $\overline{\Delta r_e} = 6$ as an equivalent width for disperse streams with a "wide" distribution law.

In this case, the estimation of the effective modal radius is performed in the same way as for a monodisperse medium (2.27) solving the transcendental equation:

$$\begin{cases} \sigma_D^e\left(\rho_{\text{mod}}^{ef}\right) = \sigma_D^x; \\ r_{\text{mod}}^{ef} = \dfrac{\lambda_{\min}}{2\pi\left|\sqrt{\dot{\varepsilon}}\right|}\rho_{\text{mod}}^{ef}, \end{cases} \tag{2.40}$$

where $\sigma_D^e(\rho)$ – calculated DRCS dependence for an "equivalent" polydisperse medium with relative distribution width of $\overline{\Delta r} = 6$ – Figure 2.11b, σ_D^x – measured value of DRCS, ρ_{mod}^{ef} and r_{mod}^{ef} – "effective" values of the modal diffraction parameter and the modal particle radius for the "equivalent" lognormal distribution.

It is natural that the distinction between the distribution width of the disperse stream under test and the value selected for an equivalent polydisperse medium $\overline{\Delta r} \neq \overline{\Delta r_e}$ leads to a methodic measurement error. Figure 2.12 shows the results of the numerical computation, which permit to estimate applicability limits of the approach under consideration. As can be seen, the normalized deviation $\delta_r = \left|\dfrac{r_{\text{mod}}^{ef}}{r_{\text{mod}}^{0}} - 1\right| \cdot 100\%$ of the effective modal radius r_{mod}^{ef} for a polydisperse medium attains 50% of its true value r_{mod}^{0} in the range of a relative distribution width of $\overline{\Delta r} = 4 - 8$.

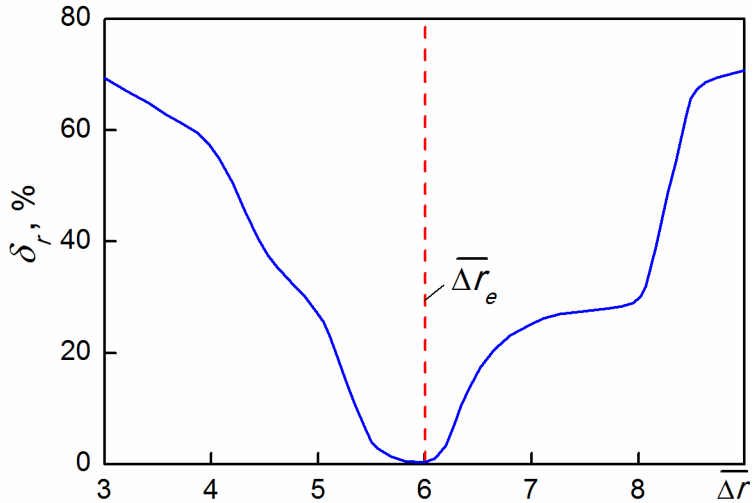

Figure 2.12 Error of approximation for polydisperse medium

At the same time, it should be noted that the range of an unambiguous measurement of the modal radius $r_{\text{mod}}^{\min} \le r_{\text{mod}} \le r_{\text{mod}}^{\max}$ is enlarged for wide distribution widths. In particular, a more detailed analysis shows that in the regime of the modal parameter $0.15 \le \rho_{\text{mod}} \le 0.32$, the range of an unambiguous measurement of the modal radius is about 72% for a polydisperse stream.

It is, however, necessary to note that the given quantitative estimations have been obtained for specified parameters of the task, so that they must be corrected in every special case.

Consequently, the use of the proposed double-frequency method of disperse stream sounding permits to obtain satisfactory results in two limiting cases, namely for both the "narrow" $\overline{\Delta r} \le 0.3$ and the "wide" $\overline{\Delta r} \ge 4$ particle size distributions. However, in the intermediate region of relative distribution widths $0.3 \le \overline{\Delta r} \le 4$ it is necessary to apply a more universal method for polydisperse stream sounding.

2.4 Conclusions to Chapter 2

As a result of the study described in Chapter 2, one can draw the following conclusions:

1. A bistatic configuration of the radar-sensor for remote sensing of disperse streams is proposed and studied. Such configuration permits to obtain high spatial resolution owing to the transmitting and receiving antenna beam interception and high isolation between transmitting and receiving channels, which allows to use a CW mode of signal radiation;

2. The radar equation for volume scatterers in the case of a bistatic configuration of the radar is obtained, which permits to measure the specific RCS of a disperse stream of solid particles;

3. An expression for the scattering volume in the case of Gaussian transmitting and receiving antenna beams is obtained. As a result of the performed analysis, relations for spatial resolution are obtained which permit to optimize the geometry of the bistatic radar-sensor;

4. A mono-frequency method for measuring characteristics of polydisperse streams is proposed for "narrow" particle size distribution $\Delta r / r_{\text{mod}} \le 0.3$. It is shown that disperse stream parameters (mass loading and concentration) can be measured by the monofrequency radar-sensor if the particle size distribution law is known;

5. A double-frequency method for measuring characteristics of polydisperse streams is proposed and limits of its applicability are defined. It is shown, that the proposed method permits to measure parameters of a disperse stream (mass loading and concentration) for arbitrary but "narrow" particle size distribution $\Delta r / r_{\text{mod}} \le 0.3$;

6. A double-frequency method for measuring characteristics of polydisperse streams is proposed for "wide" particle size distribution $\Delta r / r_{\text{mod}} \geq 4$. The method permits to estimate the effective value of the particle size, particle concentration, and mass loading. Applicability limits of the method are found taking into account unambiguity and attainable accuracy of radar measurements.

Chapter 3

Development of radar-sensors for remote sensing of disperse streams

3.1 Mono-frequency bistatic radar-sensor

In order to design radar-sensors for remote sounding of disperse streams, it is important to formulate the technical requirements for the sensor properly. Despite of a wide variety of problems arising in disperse stream sounding, one can define some general requirements for such radars.

At first, it is necessary to provide high sensitivity of the radar for detecting particles with quite small size, down to just a few microns. Since the power of the reflected signal is proportional to λ^{-4} (2.1), the use of the short-wave range of the millimeter- or even the submillimeter-wave band is most preferable.

Secondly, for obtaining high sensitivity of the radar, a necessary condition is to utilize signal integration and signal extraction against a clutter background. In this respect, coherent data processing has no alternative, because it permits to realize the most effective predetection integration of the reflected signals (Doppler filtering).

Lastly, in order to use basic equation (2.5) for developing algorithms for signal processing it is necessary to meet the requirements of spatial homogeneity of the disperse stream under test, so that statistical parameters of the medium are constant within the illuminated volume V filled by the particle ensemble. At the same time, it is necessary to take into account that the disperse stream transport channel (for instance, a duct) can have a relatively small cross-section area in a range of less than 1 – 4 m^2. Besides of that, a quite complicated longitudinal structure formed by a sequence of bends and straight portions makes the sounding of the disperse stream parameters difficult. Therefore, in order to reduce the influence of edge effects in the transport channel, the radar must provide quite a high spatial resolution along both the transverse L_x, L_y and the longitudinal L_z coordinates. Also the effective scattering volume V_{ef} must be substantially smaller than the radius of spatial correlation of the disperse stream irregularities $V_{ef} << V$.

For obtaining high spatial resolution, complex wideband signals are usually used [29],

which lead to substantial complications and rise the price of the radar hardware. Therefore, a bistatic configuration of the radar-sensor (section 2.1, Figure 2.2) is used in this work.

3.1.1 Configuration of a mono-frequency bistatic radar-sensor

To carry out an experimental study, a radar prototype on the base of a two-channel-configuration of a coherent transceiver with drifting intermediate frequency [30] is designed, taking into account the argumentations mentioned above. Such configuration almost perfectly compensates all independent (i.e. uncorrelated) frequency fluctuations of the transmitter and the local oscillator, if the correlation time of the frequency fluctuation is much shorter than the echo-delay time $\tau = \frac{1}{\delta_{\Delta f}} << \tau_R$ (τ_R – time of signal propagation to the object and back, $\delta_{\Delta f}$ – fluctuation spectrum width of the generators). In the case under consideration, the echo time will not exceed 10^{-1} microseconds during which the short-time frequency deviation of up-to-date solid-state generators [31] will not exceed $\delta_{\Delta f} \le \left(10^{-10} - 10^{-9}\right) \cdot f_0$ (where f_0 – operating frequency). For example, the absolute value of the frequency deviation during echo-time-delay will not exceed several Hz even in the 3mm wave range.

The transmitter of the designed radar – Figure 3.1 encompasses a driving generator (DG) based on an IMPATT diode [32] and a power amplifier (PA) in form of

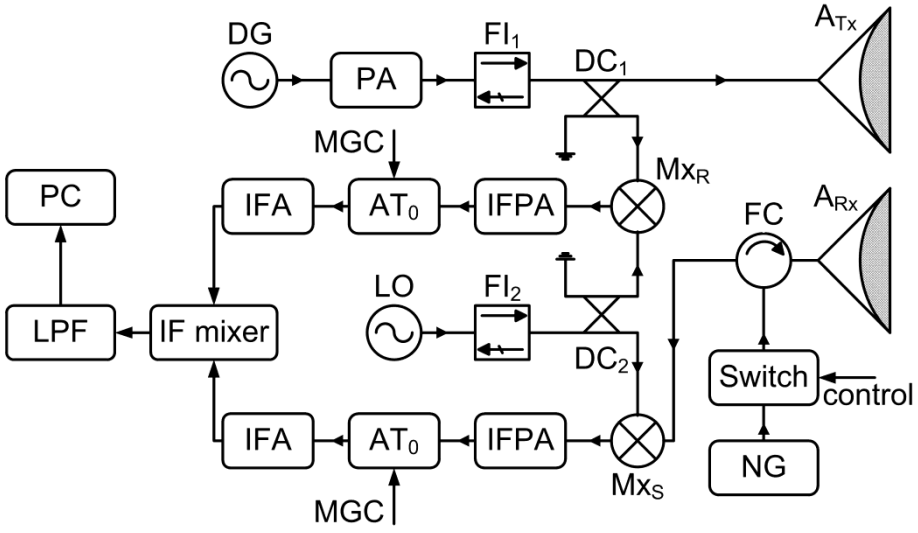

Figure 3.1 Block diagram of the coherent radar in 3mm waveband

four synchronized IMPATT diode oscillators operating in an external clock mode. The use of passive stabilization of the DG based on an external high-Q cavity resonator [33] provides high short-term frequency stability of the DG and permits to keep the information about the sounding signal phase during the echo-time-delay in order to extract the Doppler frequency from the reflected signal. A ferrite isolator FI_1 is used for reducing the influence of back reaction on frequency stability of the DG. The directional coupler DC_1 permits to tap a part of the DG power to the mixer of the reference channel MX_R. The output of the PA is connected

to a transmitting horn-lens antenna A_{Tx} in the aperture of which a Gaussian beam (2.10) is formed with respect to the recommendations mentioned in section 2.1.3.

The receiver device encompasses both the reference and the signal channel for compensating the frequency fluctuations of the DG and the local oscillator (LO) [14]. The LO is also based on an IMPATT oscillator with external high-Q cavity resonator. The directional coupler (DC_1) is used for feeding a part of the DG power into one of the input ports of the reference channel mixer (Mx_R), another port of which is fed by the power from the LO using the directional coupler DC_2. The signal from the output port of Mx_R is amplified in an intermediate frequency amplifier which consists of a preamplifier (IFPA), an electrically controlled attenuator (AT_0) for manual gain control (MGC), and the main amplifier (IFA).

The channel of the reflected signal contains a low-noise balanced mixer based on Schottky diodes [34] and the intermediate frequency amplifier, constructed in the same way as the IFA in the reference channel. A peculiarity of the receiver is the use of an additional device for receiver sensitivity calibration. The signal from the output port of a calibrated noise generator (NG) (noise power is 12 dB/kT), which is also based on an IMPATT diode [32], is coupled to a port of the ferrite circulator (FC) through a controlled microwave switch (Switch) (based on p-i-n diodes) and then to the input port of the mixer Mx_S. If the switch is turned on, the NG power enters the input port of the receiver mixer, otherwise, when the switch is turned off, the reflection coefficient of the switch becomes quite large ($|\Gamma|^2 \le$ -0.2dB), so that the power of the reflected signal enters the input port of the receiver mixer with just low losses (< -0.5dB).

The compensation of the frequency fluctuations from the DG and the LO is realized by using an intermediate frequency mixer (IF mixer), to which the signals from the reference and the signal channel are coupled. The value of the intermediate frequency at the output port of the reference channel is given by $f_{IF}^{R} = \left(\overline{f}_{T0} + \Delta f_T\right) - \left(\overline{f}_{LO0} + \Delta f_{LO}\right) = (\overline{f}_{T0} - \overline{f}_{LO0}) + + \left(\Delta f_T - \Delta f_{LO}\right) = \overline{f}_{IF} + \Delta f_{IF}$, where $\overline{f}_{T0}$, $\overline{f}_{LO0}$ – average values of the carrier frequency of the DG and the LO, respectively, Δf_T, Δf_{LO} – frequency fluctuations of the DG and the LO, $\overline{f}_{IF}$, Δf_{IF} – average value and fluctuations of the intermediate frequency at the output of the reference channel. In the same way, the value of the intermediate frequency in the signal channel is given by: $f_{IF}^{S} = \left(\overline{f}_{T0} + \Delta f_T\right) + f_D - \left(\overline{f}_{LO0} + \Delta f_{LO}\right) = (\overline{f}_{T0} - \overline{f}_{LO0}) + \left(\Delta f_T - \Delta f_{LO}\right) + f_D = = \overline{f}_{IF} + \Delta f_{IF} + f_D$. Then at the output port of the phase detector, a differential signal at frequency $f_{PD} = \left(\overline{f}_{IF} + \Delta f_{IF} + f_D\right) - \left(\overline{f}_{IF} + \Delta f_{IF}\right) = f_D$ is formed, which contains the information about the Doppler spectrum of signals reflected from an object under test. It is, however, important to note that the extraction of the Doppler spectrum from the reflected signal is only valid [31] if the RMS value of the IF fluctuations which can be calculated from $\delta_{\Delta f} = \left\{ \frac{1}{\tau_R} \int_0^{\tau_R} dt \left[f_T(t) - f_{LO}(t) \right]^2 \right\}^{1/2}$ is essentially smaller than the Doppler frequency shift of

the reflected signal $\delta_{\Delta f} << |f_D|$ during the echo-time-delay τ_R. In the considered radar configuration, these frequency fluctuations are kept low by using the passive frequency stabilization technique with an external high-Q cavity resonator [30 – 33].

The signals from the phase detector output pass through a low-pass filter (LPF) which is used for reducing the leakage of noise components, then an analog-to-digital (A/D) converter, and finally enter a personal computer (PC) in which data signal processing is carried out.

3.1.2 Antenna system of the mono-frequency bistatic radar-sensor

In order to form a Gaussian power pattern (2.10), a horn-lens antenna (HLA) is used. Its design simulation has been carried out in HFSS environment (Figure 3.2a). The antenna was simulated as a phase corrector in form of a dielectric lens ($\varepsilon = 2.1$) with hyperbolic profile. A small rectangular horn-antenna was used as a feed to provide the amplitude distribution in the antenna aperture with deep tapering ≤ -20 dB in order to decrease the side lobe level of the HLA and to avoid multi-reflections from ambient space.

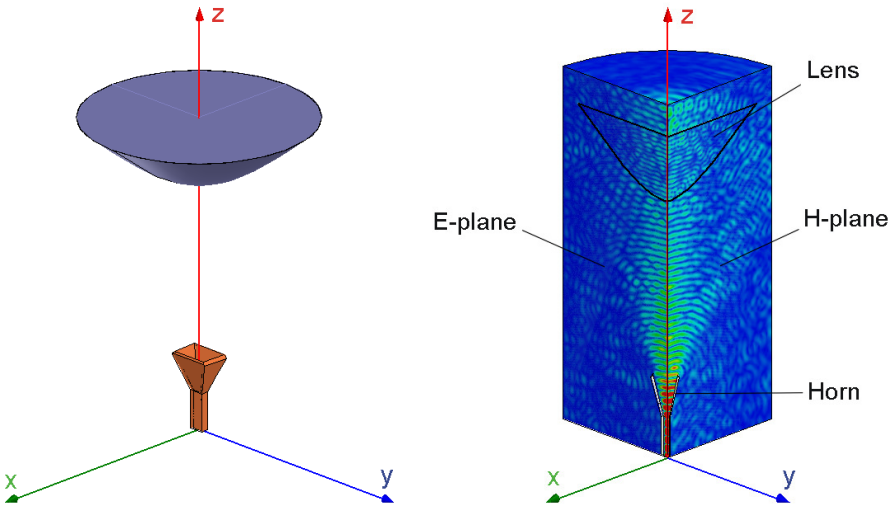

a) b)

Figure 3.2 Model for the simulation of the HLA – a); field structure of the feed – b)

An example of aperture field forming in H- and E-planes is shown in Figure 3.2b, where field power as tapered down to -20 dB from center to corner and deviation from a uniform phase distribution is not larger than 10 deg.

The antenna design is shown in Figure 3.3. The lens is made of the dielectric material Teflon with dielectric constant $\varepsilon = 2.1$ and loss tangent of $\tan(\delta) < 5 \cdot 10^{-4}$. The horn is manufactured from copper by the galvanoplastic method with further mechanical processing to join a brass flange. The lens holder is made of duralumin and covered by an absorbing material at the inner side in order to reduce the influence of multi-reflections caused by lateral radiation of the horn.

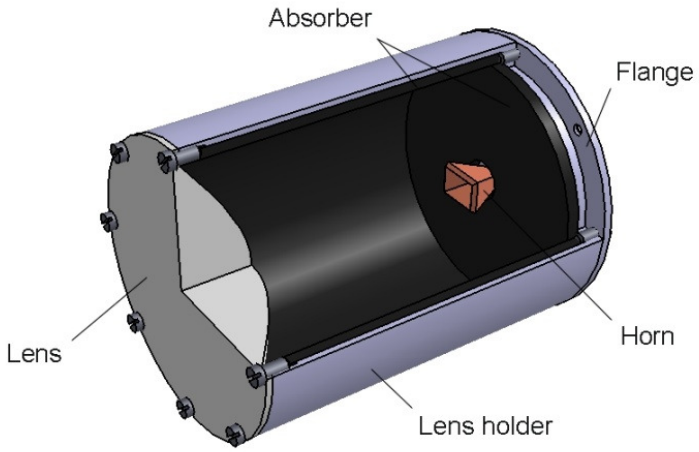

Figure 3.3 Horn-lens antenna design

The simulation results have been verified by an experimental study of the designed antenna in an anechoic chamber by means of a field scanner – Figure 3.4.

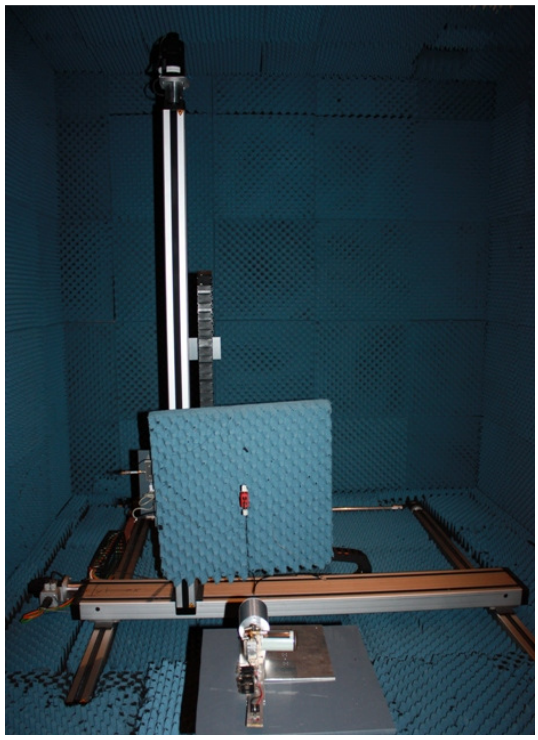

Figure 3.4 Measurement of the antenna near fields

Figure 3.5 shows a 3D field amplitude plot in the antenna aperture which confirms its axis-symmetric character with deep tapering. The corresponding curves of the 3D amplitude plot are presented in Figure 3.6 (blue curves represent measured data and black curves the calculated Gaussian distribution with beamwidth of ω_0=16.3 mm).

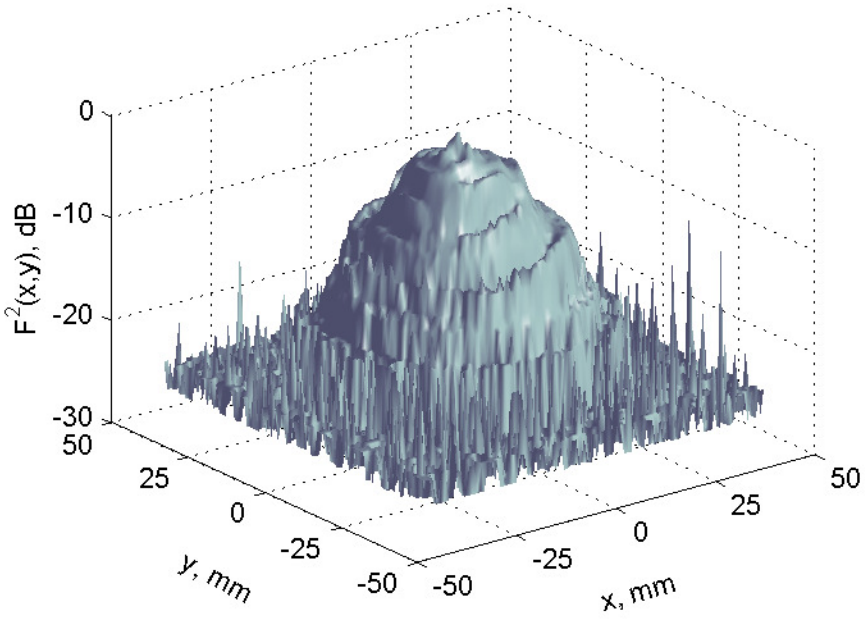

Figure 3.5 3D field plot in the aperture of the HLA

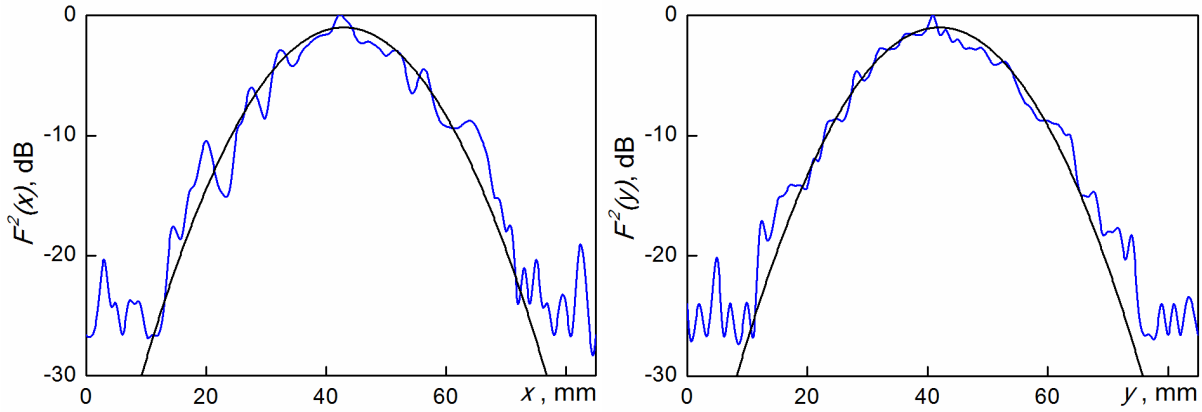

a) b)

Figure 3.6 Field distribution in HLA aperture (blue),
Gaussian beam (black). a) H-plane; b) E-plane

As one can see, aperture tapering is more than 20 dB and irregularities can be explained by multi-reflections between the measuring probe and the dielectric lens.

In Figure 3.7, the HLA far-field power patterns in H- and E- plane are presented, where the blue curves correspond to the measured data and the black curves to the calculated Gaussian power patterns (2.10). As can be seen from the figures, the measured power patterns are in good agreement with the calculated data within the main lobe down to a level of -20 dB. However, the influence of field distribution irregularities in the antenna aperture leads to forming a pedestal at a level of -22 – -25 dB.

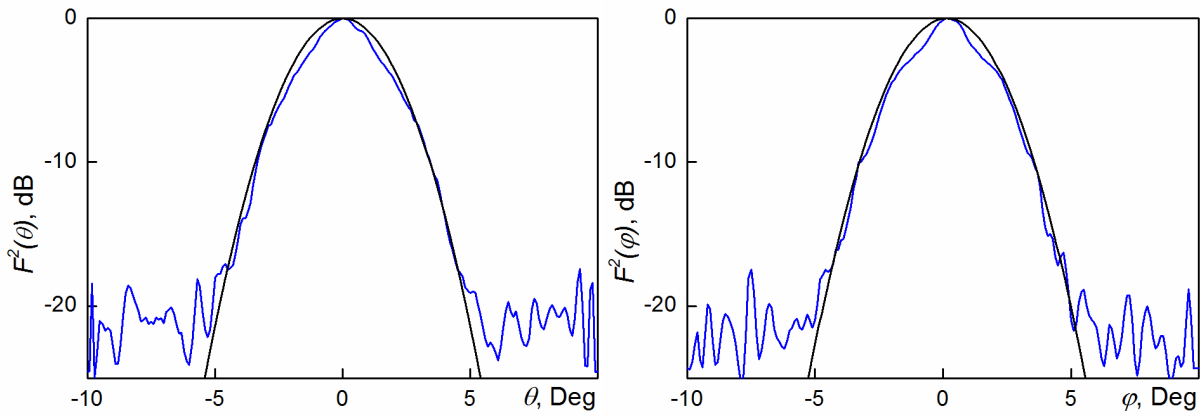

a) b)

Figure 3.7 Power pattern of the HLA (blue)
and its Gaussian beam approximation (black). a) H-plane; b) E-plane

Nevertheless, the mentioned differences between the power patterns and their Gaussian beam approximations occur only in the region of lateral radiation at a low field level, so that the expressions (2.10) and (2.11) for calculating the effective scattering volume V_{ef} can still be used.

3.1.3 Design of the bistatic radar-sensor

The design of the bistatic radar-sensor is shown in Figure 3.8. It represents an autonomous unit which includes the transmitter, receiver, power supply, and an interface unit for signal transmission into a PC.

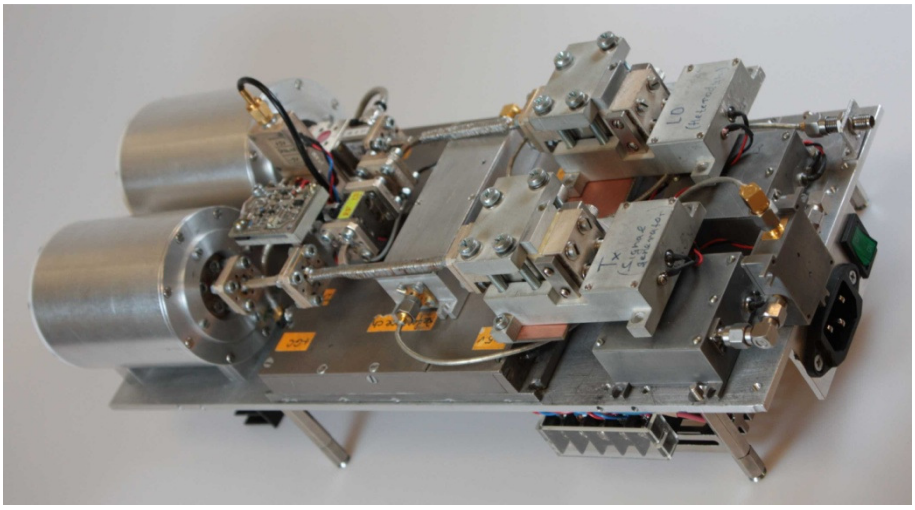

Figure 3.8 Design of the coherent radar in the 3mm wave band

The receiving and transmitting antennas are mounted on a special adjuster which permits to control the beam convergence angle α (Figure 2.2). The transceiver was built using hollow rectangular waveguides WR-10 ($1.27\times2.54\,\text{mm}^2$) and integral IF amplifiers at frequency 1.4 GHz. Such a high value of the IF decreases the influence of LO noise on sensitivity of the receiver, the noise figure (NF) of which does not exceed 10 dB. To provide high dynamic range, the IF amplifier includes 3 stages: a low-noise preamplifier (NF = 1.5

dB), a main amplifier (gain 40 dB), and an output amplifier with high dynamic range (gain 10 dB, saturation power 1 W). Between the first and the second stages, an electrically controlled p-i-n attenuator is built-in providing manual gain control over a range of 1 – 40 dB.

For calibration of the receiver sensitivity, the specially developed noise generator has been used on the base of an IMPATT diode operating in threshold mode which provides high stability of the noise level (12 dB/kT). The noise generator is controlled by a control unit which permits to control all elements of the transceiver from a PC, including switching on and off, choosing the operating mode, and power supply control.

In front of the A/D converter, a low-pass filter (LPF) is used, the bandwidth of which is matched with the reflected signal to avoid noise acquisition in the process of digitizing. The cut-off frequency of the filter is determined by the maximum width of the signal spectrum which is equal to f_c = 9 kHz in the case under consideration. As the LPF prototype, a Butterworth low-pass filter of 5th order has been used because such filter provides the smoothest frequency response in both pass and stop band. The 5th order of the filter guaranties an off-frequency rejection of more than 30 dB per octave, which is sufficient for suppression of receiver noise components in the signal bandwidth. Besides of that, the filter provides minimal transient distortions in the case of pulse clutter.

The filter is designed on the base of Cauer topology, which uses passive elements (capacitors and inductors). The frequency characteristic is calculated using ADS 2008 (advanced design system) environment for a cut-off frequency of about 9 kHz, and by taking into account only standard values of the lumped elements. The measured and calculated frequency characteristics of the designed filter are shown in Figure 3.9a. Discrepancies in the pass- and stop-band are caused by the influence of flicker-noise in the low-frequency region and by the spread of parameters of the passive elements.

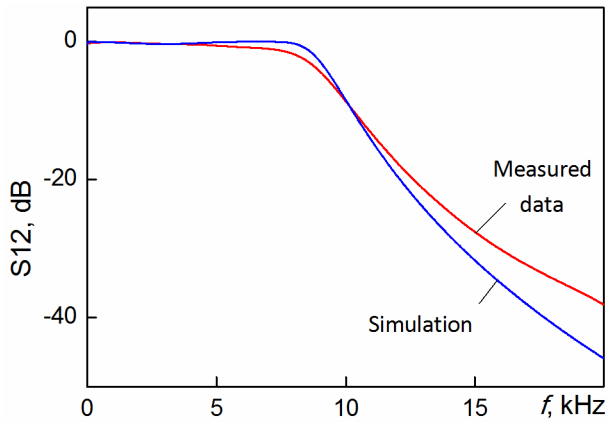

a)

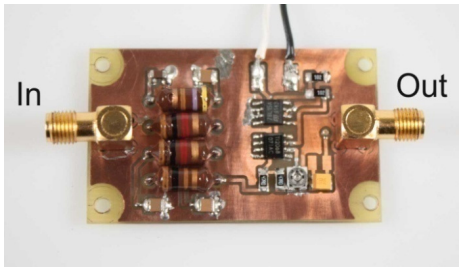

b)

Figure 3.9 Frequency characteristics of the LPF – a); outlook of the LPF – b)

Figure 3.9b shows an outlook of the LPF, which is equipped with an amplifier for the Doppler signal and with manual gain control.

The parameters of the radar prototype which have been measured during its test are summarized in Table 3.1.

Table 3.1 Parameters of the coherent bistatic radar in the 3mm wave band

N	Parameter	unit	value
	1. Antenna-feeder path		
1.1	- Aperture size	mm	60
1.2	- Field "spot" radius in the aperture	mm	16.3
1.3	- Beam width	deg	2.95
1.5	- Sidelobe level	dB	≤ 26
1.4	- Gain	dB	31.3
1.6	- Antenna effective area	-	0.38
1.7	- Isolation (transmitter -receiver)	dB	≥ 80
1.8	- Beam convergence angle ($2\alpha_a$)	deg	2.5
1.9	- Distance between antennas ($2L$)	mm	70
1.10	- Longitudinal coordinate of beam interception (z_0)	m	0.802
1.11	- Size of illuminated area $z_{\min}$	m	0.31
	$z_{\max}$		2.005
	2. Transceiver		
2.1	-Operational frequency	GHz	92.82
2.2	-Wavelength	mm	3.23
2.3	-Average illumination power	W	0.1
2.4	-Frequency noise level (frequency mismatch 10 kHz)	dB/Hz	$\leq$ -90
	3. Receiver		
3.1	-LO frequency	GHz	94.23
3.2	-Receiver noise-figure	dB	≤ 10
3.3	-Peak sensitivity	W/Hz	$\approx 1\ 10^{-19}$
3.4	-Intermediate frequency	GHz	1.4±0.3
3.5	-IF gain	dB	63
3.6	-Gain control range	dB	$\geq$25
3.7	-Filter pass band	kHz	0 – 18
	4. Data processing parameters		
4.1	-Sampling rate	kHz	44
4.2	-Resolution of A/D converter	-	10
4.3	-Signal realization volume	MB	1.3

As one can see, the parameters shown in Table 3.1 correspond to the modern state of radar technology in the short millimeter wave band.

3.1.4 Signal processing of the radar-sensor in spectral domain

The data signal processing consists of a Doppler spectrum evaluation using a fast Fourier transform (FFT) in the form:

$$S(\omega) = \frac{S_0}{T}\left|\int_0^T dt\, U(t) e^{-j\omega t}\right|, \tag{3.1}$$

where $U(t)$ – radar output signal, $\omega = 2\pi f$ – angular frequency, S_0 – constant which depends on receiver gain. For measuring the volume scatterer characteristics, the power

spectral density (PSD) of the signal reflected is used: $PSD(\omega) = T \cdot S^2(\omega)$ (W/Hz). In the measurement of the specific RCS of the disperse stream, it is useful for calculating the total received power (which is given in expression (2.8)) by using PSD integration in the Doppler spectral band of the scattered signal: $P_R = \int_{\omega_{\min}}^{\omega_{\max}} d\omega PSD(\omega)$. The constant S_0 can be determined from radar calibration by using the noise generator during the measurement process (section 3.1.1).

As has been mentioned above, for detecting disperse streams with small particles (< 5μm), it is necessary to use signal integration, including predetection and postdetection integration. In the case under consideration, the predetection integration is realized programmatically in a PC, because the analogue radar signal had to be digitized before. The A/D converter provides 10 bit capacity and a sampling frequency of 44.1 kHz.

The narrowband predetection integration has been performed by evaluating the signal spectrum using Fast Fourier Transform (FFT). Here the bandwidth of the equivalent filter is equal to $\Delta f_{eq} = 10.76$ Hz (time of integration $t_{\text{int}}^{pre} = 93$ ms). The postdetection integration has been applied for programmable smoothing of the output data by properly choosing the averaging period. On the one hand, this time interval must be essentially larger than a correlation interval of the signal fluctuations, but on the other hand, it must not exceed the time interval of the disperse stream stationarity. As has been defined experimentally, the optimal period of the postdetection integration is about $2-3$ seconds, and a value of $t_{\text{int}}^{post} = 2.325$ s has been chosen in the case under consideration.

This approach has been realized for the example of a disperse stream with corundum particles of 152 μm in size. The spectrum of the radar signals is presented in Figure 3.10.

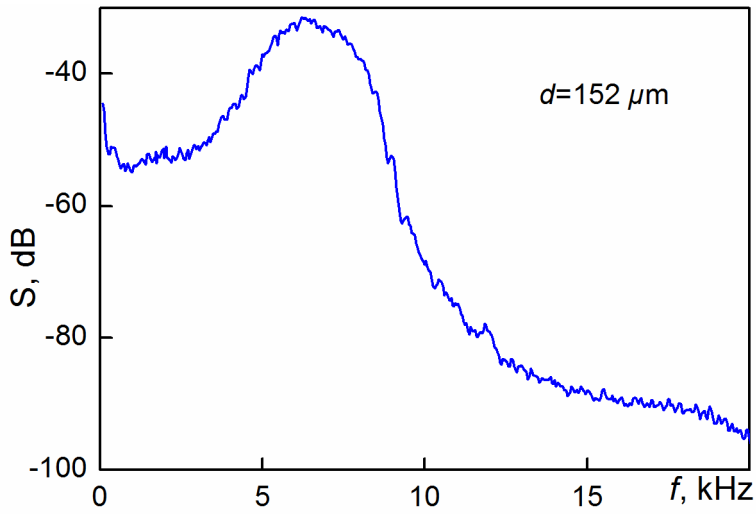

Figure 3.10 Signal spectrum reflected from corundum particles

It is important to note that turbulences of the stream cause spectrum widening and the signals approach a noise-like form. As one can see, the mean Doppler frequency (7.1 kHz) satisfactorily corresponds to the average velocity of the stream (11.3 m/s). The decay of the spectrum at frequencies above 9 kHz is caused by the shape of the LPF characteristic.

Thus the use of spectral signal processing provides physically obvious data which permit to analyze the nature of the turbulent processes in disperse streams.

3.1.5 Signal processing of radar-sensor in time domain

Since weak signals reflected from disperse streams of small particles have noise-like nature and provide low values of their signal-to-noise ratio (SNR), narrow-band signal processing is not effective enough and does not provide the required sensitivity of the radar. Therefore, correlation processing based on differences between the fine structures of the reflected signal and the receiver noise [35] has been considered here.

Indeed, if the signal realisation time essentially exceeds the correlation window of a noise-like signal $T_0 >> \tau_S$, a correlation function (CF) of such a signal with Doppler frequency shift can be depicted as shown in Figure 3.11.

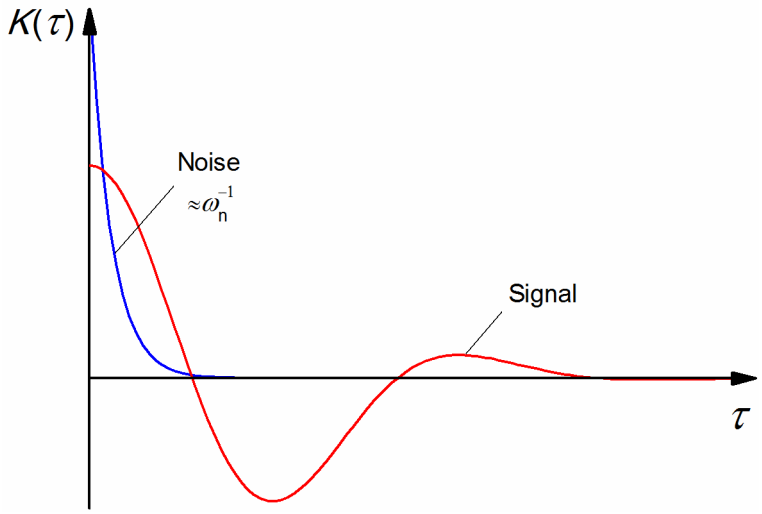

Figure 3.11 The correlation function of a noise-like signal with Doppler frequency shift and the correlation function of the noise

It may be expressed as [36]

$$K_S(\tau) = \left\langle U_S(t) \cdot U_S^*(t+\tau) \right\rangle = \sigma_S^2 \exp\left\{ -\left(\frac{\Delta\omega_S \tau}{2} \right)^2 \right\} \cos \omega_D \tau \qquad (3.2)$$

where σ_S^2 – dispersion of the signal, $\Delta\omega_S$ – spectrum bandwidth of the reflected signal, ω_D – average Doppler frequency, τ – time delay, brackets $\langle\ \rangle$ mean time averaging – $\left\langle U(t) \right\rangle = \lim_{T_0 \to \infty} \int_0^{T_0} U(t)\, dt$, and index (*) indicates complex conjugation.

By analogy with the signal CF, the CF of the thermal noise of a receiver (Figure 3.11), the spectrum of which is uniform [36] in the frequency band from 0 to ω_N, can be written as

$$K_N(\tau) = \left\langle U_N(t) * U_N^*(t+\tau) \right\rangle = \sigma_N^2 \exp\{-\omega_N \tau\}, \tag{3.3}$$

where σ_N^2 – dispersion of the thermal noise.

As one can see, an increase of the receiver bandwidth leads to decreasing the noise correlation window $\tau_N = \omega_N^{-1}$, while the CF of the signal oscillates with the Doppler frequency (Figure 3.11). The difference in shape of the correlation functions enables one to distinguish between a noise-like signal and the thermal noise.

The signal at the output of the linear radar receiver is given by a sum of the wanted signal and the noise: $U_{SN}(t) = U_S(t) + U_N(t)$, the CF of which can be expressed by

$$\begin{aligned} K_{SN}(\tau) = \left\langle U_{SN}(t) * U_{SN}^*(t+\tau) \right\rangle = \left\langle U_S(t) * U_S^*(t+\tau) \right\rangle + \left\langle U_S(t) * U_N^*(t+\tau) \right\rangle + \\ + \left\langle U_N(t) * U_S^*(t+\tau) \right\rangle + \left\langle U_N(t) * U_N^*(t+\tau) \right\rangle. \end{aligned} \tag{3.4}$$

Since the thermal noise and the wanted signal are uncorrelated, the crossed components in equation (3.4) turn into zero, which permits to simplify the equation to the form of an algebraic sum of the CF of the noise and the CF of the wanted signal:

$$K_{SN}(\tau) = \left\langle U_S(t) * U_S^*(t+\tau) \right\rangle + \left\langle U_N(t) * U_N^*(t+\tau) \right\rangle = K_S(\tau) + K_N(\tau) \tag{3.5}$$

In order to detect the wanted signal against the background noise, one can make a decision based on the criterion of normalized root-mean-square distance $\bar{D}$ for describing the similarity of the wanted signal and the noise [37]. Taking into account relation (3.5), the normalized root-mean-square distance can be written as

$$\bar{D} = \frac{\int_0^\infty d\tau \left[K_{SN}(\tau) - K_N(\tau) \right]^2}{\int_0^\infty d\tau \left[K_N(\tau) \right]^2} = \frac{\int_0^\infty d\tau \left[K_S(\tau) \right]^2}{\int_0^\infty d\tau \left[K_N(\tau) \right]^2}. \tag{3.6}$$

Then a decision about an occurrence of the signal in the combination of "signal + noise" can be made using conditions:

$$\begin{cases} U_{SN} \in U_S & \text{if } \bar{D} \geq \varepsilon \\ U_{SN} \in U_N & \text{if } \bar{D} < \varepsilon \end{cases}, \tag{3.7}$$

where ε – detection limit.

The integrals in (3.6) can be calculated using elementary functions, so that the final equation can be written as

$$\bar{D} = \sqrt{2\pi}\left(\frac{\sigma_S^2}{\sigma_N^2}\right)^2 \frac{\omega_N}{\Delta\omega_S} \exp\left\{-\left(2\frac{\omega_D}{\Delta\omega_S}\right)^2\right\}. \tag{3.8}$$

Since dispersion of the signal (or noise) is proportional to the signal (or noise) power $P \approx K(0) = \langle U(t) \cdot U^*(t) \rangle$, the detection conditions (3.7) are transformed to

$$\frac{P_S}{P_N} \approx \frac{\sigma_S^2}{\sigma_N^2} > \sqrt{\frac{\varepsilon}{F_D}}, \tag{3.9}$$

where P_S – signal power, P_N – noise power, and F_D – efficiency factor of the correlation procedure under consideration:

$$F_D = \sqrt{2\pi}\frac{\omega_N}{\Delta\omega_S} \exp\left\{-2\left(\frac{\omega_D}{\Delta\omega_S}\right)^2\right\}. \tag{3.10}$$

In other words, if $F_D > 1$, the use of the correlation algorithm provides minimal gain in comparison to the spectral processing considered above. Therefore, the condition that provides advantage over the spectral processing can be written as

$$\frac{\omega_N}{\Delta\omega_S} > \frac{1}{\sqrt{2\pi}} \exp\left\{2\left(\frac{\omega_D}{\Delta\omega_S}\right)^2\right\}. \tag{3.11}$$

The analysis for optimal bandwidth of the receiver has been carried out. As can be seen from Figure 3.12, the considered algorithm is effective for noise-like signals with Doppler frequency being comparable to the value of the signal spectrum width $\omega_D \approx \Delta\omega_S$. Otherwise the receiver bandwidth must be increased essentially.

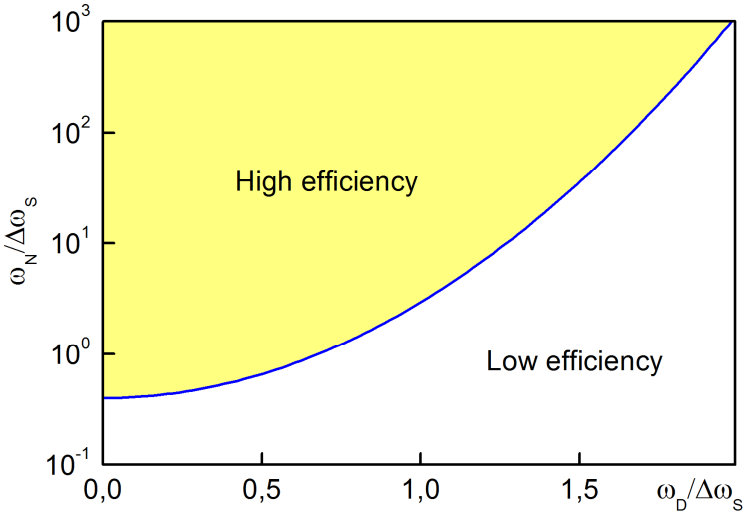

Figure 3.12 Dependence of normalized receiver bandwidth on mean Doppler frequency

Nevertheless, expression (3.9) does not permit to estimate the maximum achievable gain for the signal-to-noise ratio (SNR), because the value of the detection limit ε depends on statistical properties of the signal and must be defined experimentally.

In order to check the suggested method of utilizing the correlation, an experimental set-up (Figure 3.13) has been designed, in which signals from two noise generators are

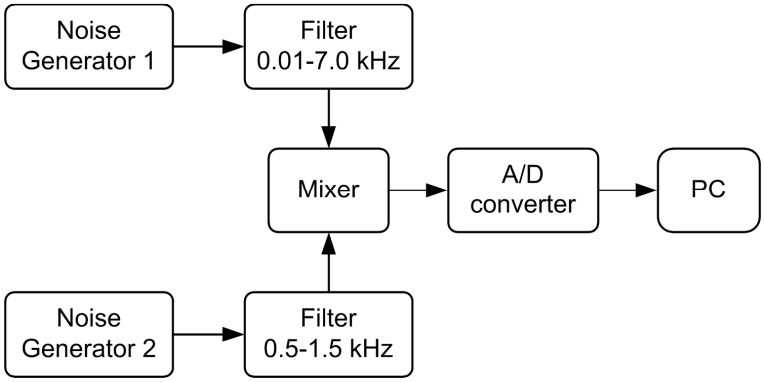

Figure 3.13 Block diagram of the correlation experiment set-up

coupled through a low-pass filter with bandwidth 0.01 – 7 kHz to simulate the thermal noise of a receiver and a pass-band filter (PBF) with frequency bandwidth 0.5 – 1.5 kHz to simulate the wanted signal, respectively. The signal composition obtained in the mixer permits to model the signal reflected from a particle stream. The signal composition is then quantized in an A/D converter for further signal processing in a PC.

In Figure 3.14a, the spectra of the signal and noise composition with an input SNR being equal to -7 dB (red curve), just the noise (black curve), and the wanted noise-like signal (blue curve) are shown. As one can see, the signal is practically indistinguishable from the background noise. Figure 3.14b shows the CF of the composition and the CF of the noise, which has been calculated using expressions (3.3 – 3.9). Despite the small value of the input SNR ($SNR_{in} = -7\text{dB}$), the correlation signal processing permits to increase the output SNR up to 14.8 dB.

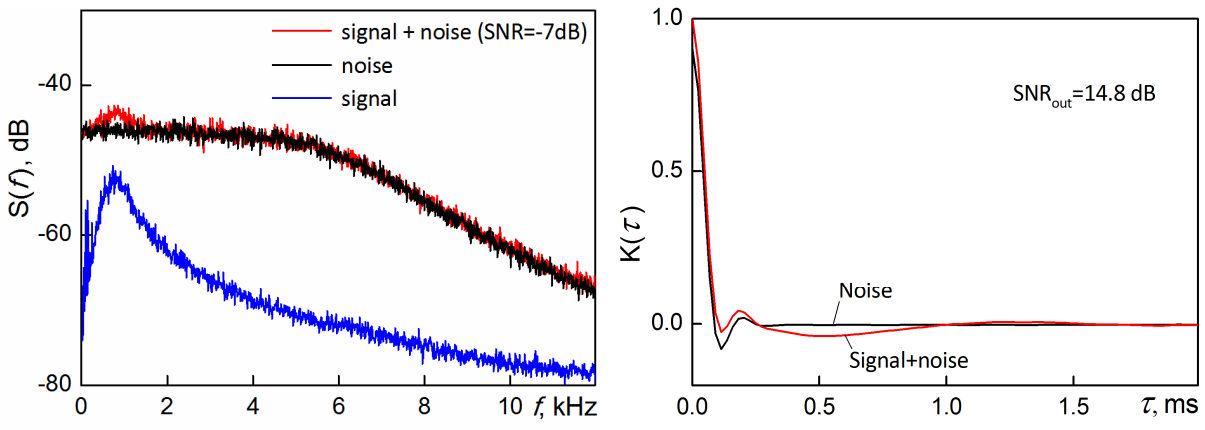

a) b)

Figure 3.14 Spectra– a) and correlation functions of the simulated signals – b)

The measured dependence of the output SNR on the input SNR is shown in Figure 3.15, which confirms the possibility of signal extraction for low values of the input SNR ($SNR_{in} \le -20\text{dB}$).

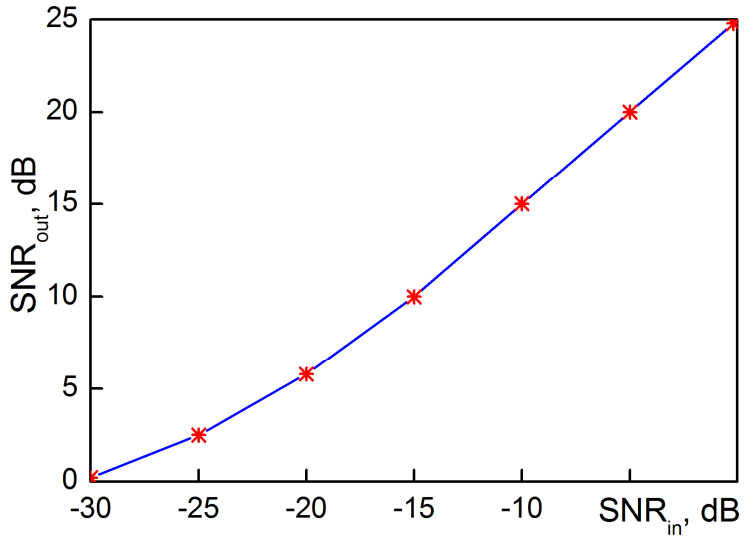

Figure 3.15 Dependence of the output SNR on the input SNR

Nevertheless, the considered method of extracting the wanted noise-like signal from the background noise of the receiver requires high stability of the signal and the noise. In other words, if and when a nonstationary clutter occurs in the "signal + noise" composition, the efficiency of the considered algorithm dramatically decreases.

Figure 3.16 presents two spectra of radar signals (section 3.1.3) which have been measured at two subsequent points of time $t1$ and $t2$. In this case, the reflected signals contain the clutter caused by reflections from vibrating parts of the experimental set-up, the vibration frequency of which changes versus time.

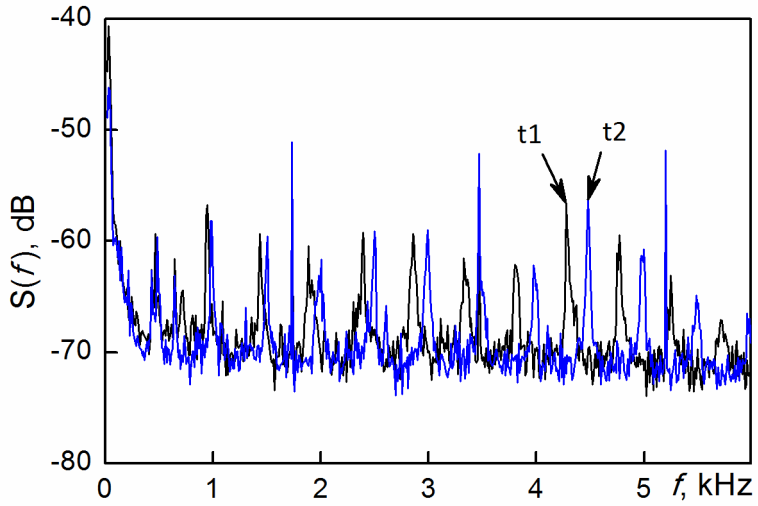

Figure 3.16 Spectrum of signal and vibrating duct

This situation violates the condition of clutter stationarity and thus reduces the value of the output SNR from 10 dB down to 2 dB. Hence applying the corresponding algorithm for disturbance compensation requires a high level of suppression of the nonstationary clutter.

3.2 Mono-frequency monostatic quasioptical radar-sensor

The bistatic radar considered in the previous chapters provides rather high sensitivity, spatial resolution, and isolation between transmitter and receiver channels, which permits to use the continuous wave (CW) mode of radiation. However, the technical realization of these advantages is only justified for short distances between the target and the radar itself: $z \cong z_0 = L / tg\alpha_a$ (Figure 2.2), since these distances are comparable to the spatial resolution of the bistatic radar (in the considered case (section 2.1.3), $\Delta z \cong 0.4 z_0$, where z_0 – distance from the radar to the interception point of the antenna beams).

On the other hand, disperse stream sensing for long distances is of substantial practical interest. In this connection, the application of a bistatic configuration of the radar is strongly restricted; therefore a monostatic configuration of the radar is developed here. Such radar can also be operated in CW mode. It provides joint operation of the transmitter and the receiver with a common antenna. In this case, a high spatial resolution can be provided owing to amplitude or frequency modulation of the transmitter.

However, such an approach requires providing high isolation between the transmitter and the receiver to avoid overload of the receiver and its saturation by transmitter noise. Therefore, the configuration of the quasioptical antenna feeder which contains a duplex device (DD) on the base of a cross-shaped junction of quasioptical waveguides [38] has been proposed.

3.2.1 Configuration of the antenna feeder system

The configuration of the antenna feeder is shown in Figure 3.17 where a Goubau beamguide [39] with dominant TEM_{00} mode is used. The beam-waveguide diameter significantly exceeds the wavelength ($d > 20\lambda$). The DD is represented by a quasioptical beam splitter [38] in the form of a cross-shaped junction of beam-waveguides with dielectric layer placed in the diagonal section of the junction. The principle of operation can be deduced from Figure 3.17 – the signal from transmitter T_X is coupled to the waveguide launcher of the transmitter channel (WL_T) which provides the field forming of the quasioptical beam, and then is split between the straight and the cross-arm of the DD. One part of the power is absorbed by the matched load; another part feeds the secondary reflector of the off-set near-field Gregorian antenna [21] and is then radiated into free space. The main and the secondary reflectors of the antenna have the shape of cut paraboloids with common focus at point *F* (Figure 3.17).

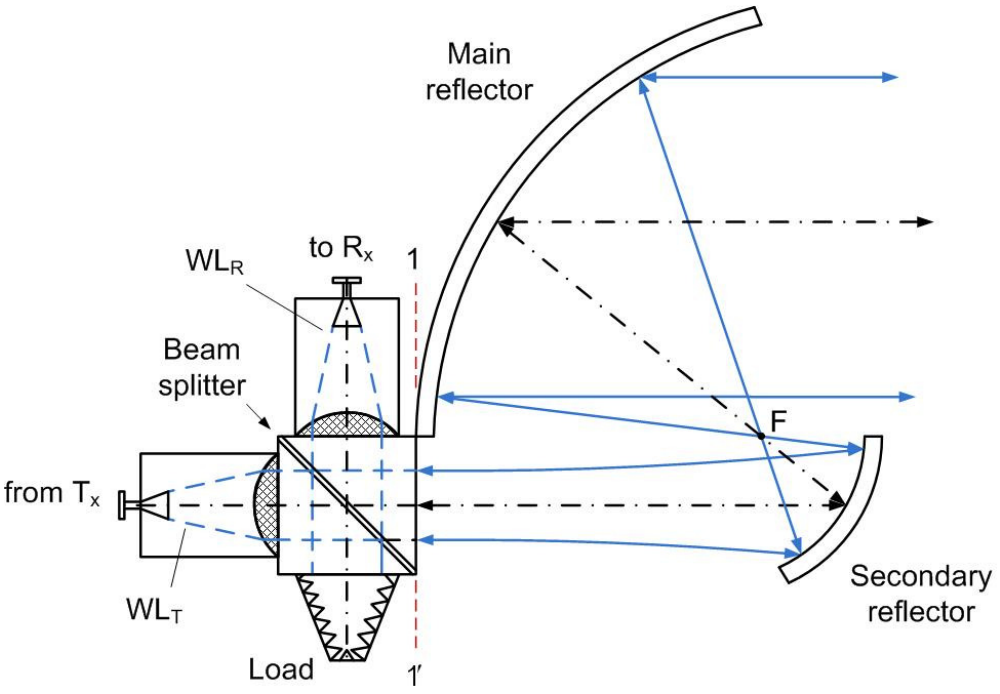

Figure 3.17 Configuration of quasioptical transmit-receive antenna-feeder path

The reflected signal from the disperse stream under test is coupled to the DD, one part of the signal enters the cross-arm port of the receiver channel (WL_R) and the other part is lost in the transmitting channel. Hence the DD provides high isolation between transmitting and receiving channels of as high as 60 dB over a wide frequency band, which is only limited by diffraction effects in the cross-shaped beam-waveguide junction. The insertion loss can be compensated by increasing the antenna gain by using a reflector of bigger size, since the SNR (2.1) is proportional to D_A^2/λ (D_A – size of the antenna aperture), so that a 40% increase of the reflector diameter can compensate 6 dB signal loss in the feeder.

In order to provide the highest possible isolation between the transmitting and receiving channels, a double-reflector Gregorian antenna with offset feed is used [38]. The design of such an antenna provides minimal back-reflections because there are no reflective surfaces in a direction normal to that of beam propagation.

3.2.2 Development of duplex device

Considering the duplex device in more detail, it is possible to optimize its operation as follows: The transmitter power at the output of the junction in section $1-1'$ (Figure 3.17) is equal to $P_{1-1} = P_T T_D$, where T_D means power transmission coefficient between input and output port and P_T means transmitting power at the input port of the DD. In order to estimate the total coefficient of transmit-receive loss (TRL), one can assume that the output of the junction (section $1-1'$) is closed by a metal mirror. Then the power at the cross-arm port WL_R is $P_R = P_{1-1} R_D$, where R_D means the power reflection coefficient. Consequently, the total TRL in the DD is equal to the product of the coefficients T_D and R_D:

$$\eta_{T-R} = \frac{P_R}{P_T} = \frac{P_{1-1} R_D}{P_T} = T_D R_D \left|\dot{\Gamma}\right|^2 . \tag{3.7}$$

where $\left|\Gamma\right|^2$ – reflection coefficient of the mirror. Neglecting the loss in the thin dielectric layer and assuming an ideal mirror ($\left|\Gamma\right|^2 = 1$) yields $T_D = 1 - R_D$, so that one can obtain the expression for the total loss as $\eta_{T-R} = R_D \left(1 - R_D\right)$. Differentiating this expression with respect to R_D and setting the derivative equal to zero, one can show that the minimum of the TRL corresponds to the value of $T_D^{opt} = R_D^{opt} = 0.5$. Therefore, the optimum value of the transmission and reflection coefficient is equal to -3 dB each.

To define conditions under which it is possible to realize the optimal DD parameters, it is necessary to consider the expression for the reflection coefficient of a plane wave incident upon the dielectric layer [40]:

$$R_D = \left| \frac{r_{12} + r_{23} e^{2j\beta}}{1 + r_{12} r_{23} e^{2j\beta}} \right|^2 , \tag{3.8}$$

where the subscripts designate the medium (air – 1, dielectric – 2, and air – 3). The reflection coefficients from the infinite half-space r_{12} and r_{23} depend on the orientation of the polarization plane. In particular, when the polarization vector is perpendicular to the plane of incidence (TE – wave), r_{ij} is given by

$$r_{ij} = \frac{p_i - p_j}{p_i + p_j}; \qquad p_i = \sqrt{\varepsilon_i} \cos\theta_i ; \tag{3.9}$$

and for parallel polarization (TM – wave):

$$r_{ij} = \frac{q_i - q_j}{q_i + q_j}; \qquad q_i = \frac{\cos\theta_i}{\sqrt{\varepsilon_i}} . \tag{3.10}$$

The phase angle is equal to $\beta = kh\sqrt{\varepsilon_2}\cos\theta_2$, where h – thickness of the dielectric layer, ε_i – permittivity of the i^{th} – medium. The angle θ_2 is determined from the refraction law: $\sin\theta_2 = \frac{1}{\sqrt{\varepsilon_2}} \sin\theta_1$. In the case under consideration, when the dielectric layer is oriented at an angle of 45°, the expressions (3.8 – 3.10) can be simplified using obvious relations: $\theta_1 = \theta_3 = 45°$, $\varepsilon_1 = \varepsilon_3 = 1$, $\varepsilon_2 = \varepsilon$, $r_{12} = -r_{23} = r_D$. Then leaving out lengthy transformations, the resulting expressions are:

$$R_D = 2r_D^2 \frac{1 - \cos 2\beta}{1 - 2r_D^2 \cos 2\beta + r_D^4} \tag{3.11}$$

$$r_D = \begin{cases} \dfrac{1-\sqrt{2\varepsilon-1}}{1+\sqrt{2\varepsilon-1}} & TE-\text{wave} \\ \dfrac{\varepsilon-\sqrt{2\varepsilon-1}}{\varepsilon+\sqrt{2\varepsilon-1}} & TM-\text{wave} \end{cases} \tag{3.12}$$

$$\beta = kh\sqrt{\varepsilon-0.5} \tag{3.13}$$

where $k = 2\pi/\lambda$, λ–wavelength in free space.

As has been shown, a necessary condition for minimizing the TRL is that T_D and R_D must be equal to 0.5. However, this value cannot be achieved for the reflection coefficient if the layer material permittivity shows too small values. On the other hand, the maximum value of the reflection coefficient corresponds to a layer thickness which is proportional to a quarter of a wavelength in the material:

$$h = \frac{\lambda}{4\sqrt{\varepsilon-0.5}}(2m+1), \quad m = 0, 1, 2, \ldots . \tag{3.14}$$

As numerical simulations show, the minimum value of the dielectric layer permittivity which still corresponds to a reflection coefficient value of $R_D = 0.5$, is different for each polarisation, so that $\varepsilon = 3.4$ results for perpendicular polarization (TE – wave) and $\varepsilon = 11$ for parallel polarization (TM – wave). In the last case, using materials with such a high value of permittivity is rather problematical; however, in the case of the perpendicular polarization, some dielectric materials with corresponding parameters exist and can be used.

The dependence of the phase angle β on the wavelength leads to a frequency dependence of the reflection coefficient, so that the maximum bandwidth can be achieved for a layer, whose thickness corresponds to (3.14). The frequency variation from the optimal value f_0 leads to an additional TRL, but the loss increase is rather insignificant, namely ~ 0.2 dB even for a relative frequency deviation of ± 40%, as shown in Figure 3.18 (the blue

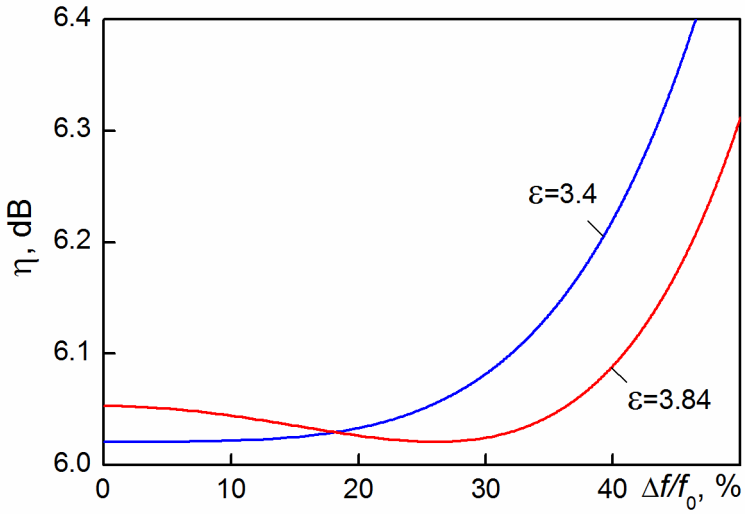

Figure 3.18 Dependence of TRL loss on frequency deviation

curve corresponds to the data for the optimal value of the permittivity $\varepsilon = 3.4$, the red curve shows the TRL calculated for fused quartz with $\varepsilon = 3.84$). As can be seen from the figure, a realization of "close-to-optimal" characteristics of the duplex device is still possible using widely available materials.

The described DD has been designed (Figure 3.19) and experimentally studied in W-band. The dielectric layer is made of fused quartz ($\varepsilon = 3.84$), the thickness of the layer is

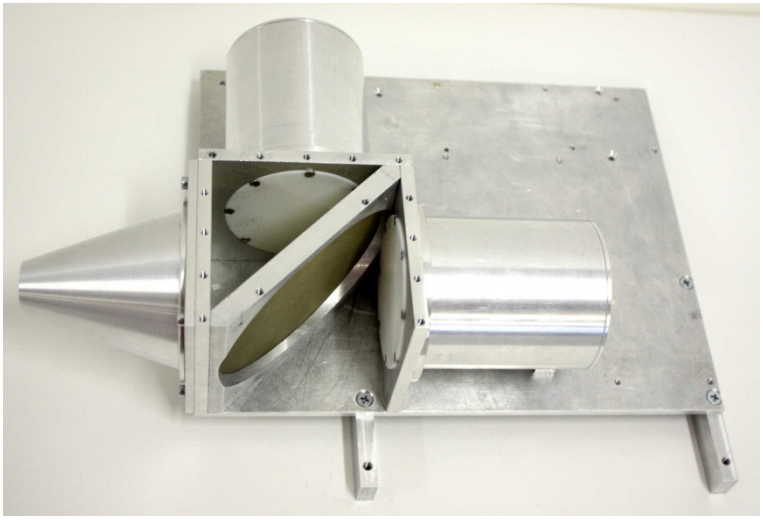

Figure 3.19 Outlook of the duplex device

0.45 mm, which is very close to the optimal value ($h_{opt} = 0.442$ mm) according to (3.14). The construction of the device consists of machined aluminum plates connected with each other on a common base, which provides quasioptical beam interception at an angle of 90°± 30'.

The experimental study of the DD was performed in an anechoic chamber by means of an electromagnetic field scanner (Figure 3.20) for both the transmitting and receiving channel. The results have been plotted in a common coordinate system. The amplitude field

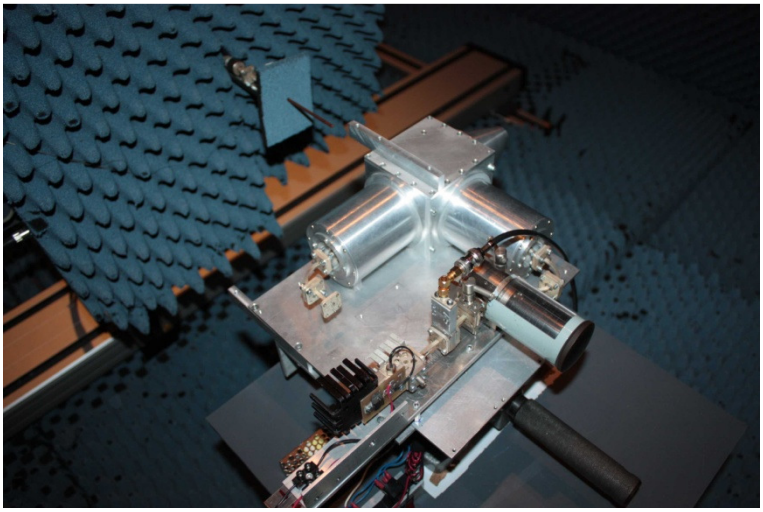

Figure 3.20 Workbench for measurement of the DD field structure

distributions in the beam cross-sections at different distances z_n from the DD output have been measured. The configuration of the field distribution measurement is shown in Figure 3.21. The distance z has been chosen within the range of 0 – 1500 mm.

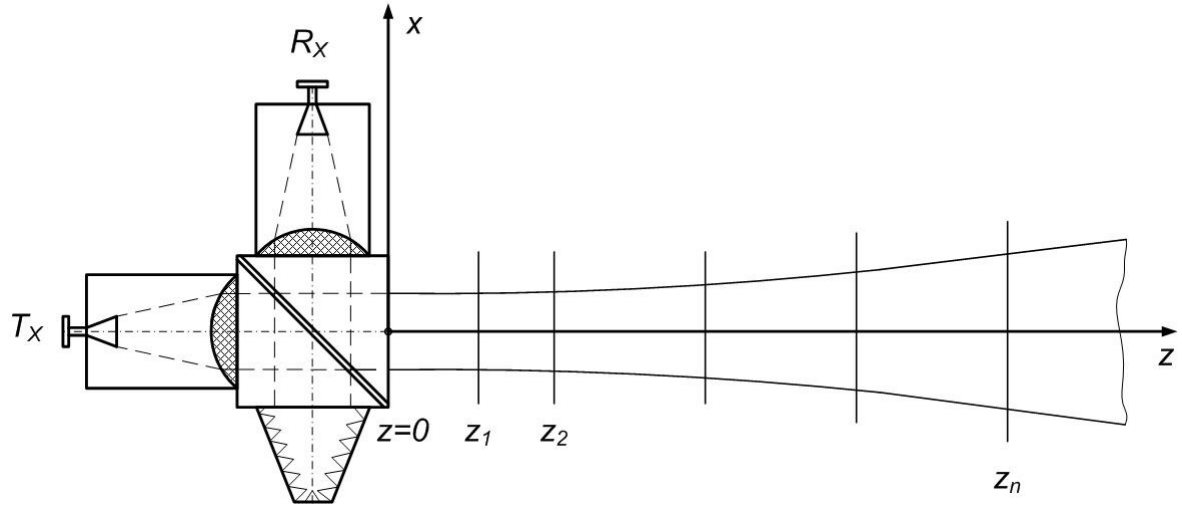

Figure 3.21 Configuration for measurement of the DD field structure

As an example, the measurement results for the quasioptical beam profiles in the principal planes are presented in Figures 3.22 – 3.24 (H-plane – at the left, E-plane – at the right).

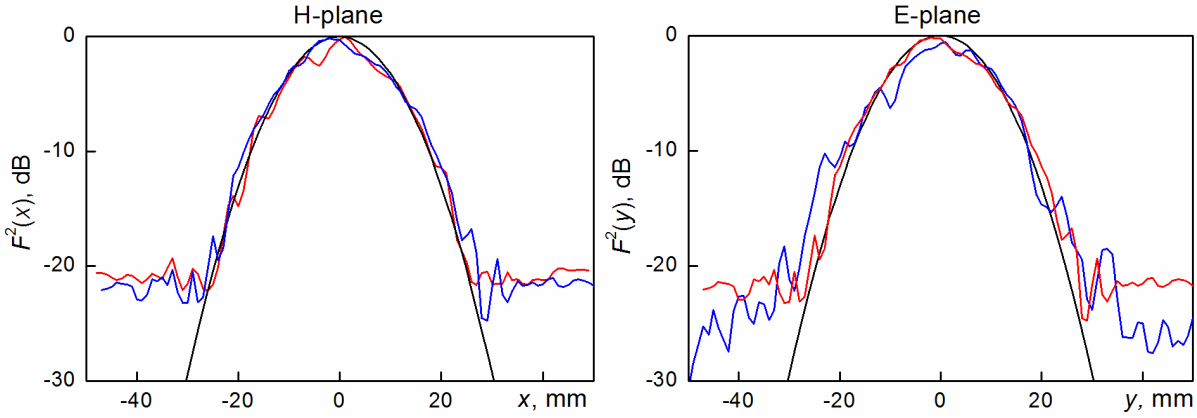

Figure 3.22 DD power profiles in the beam cross section at $z = 0$ mm

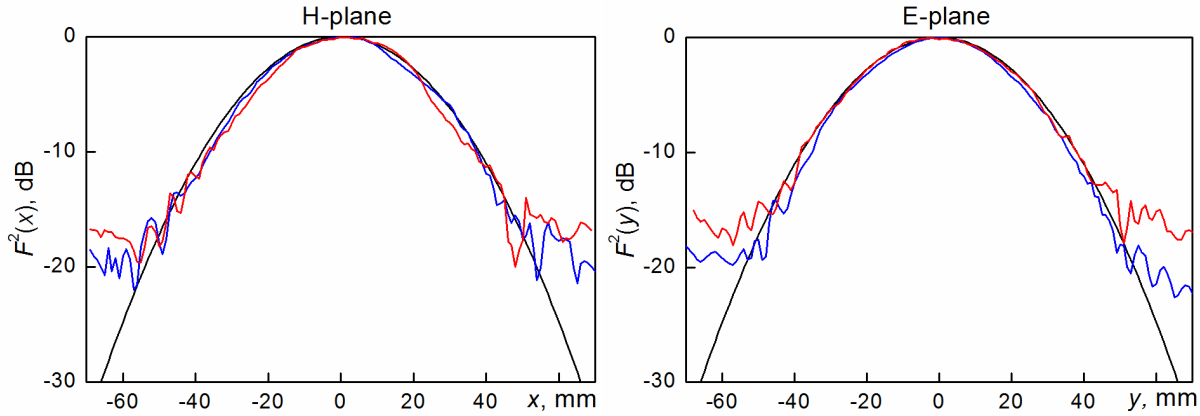

Figure 3.23 DD power profiles in the beam cross section at $z = 500$ mm

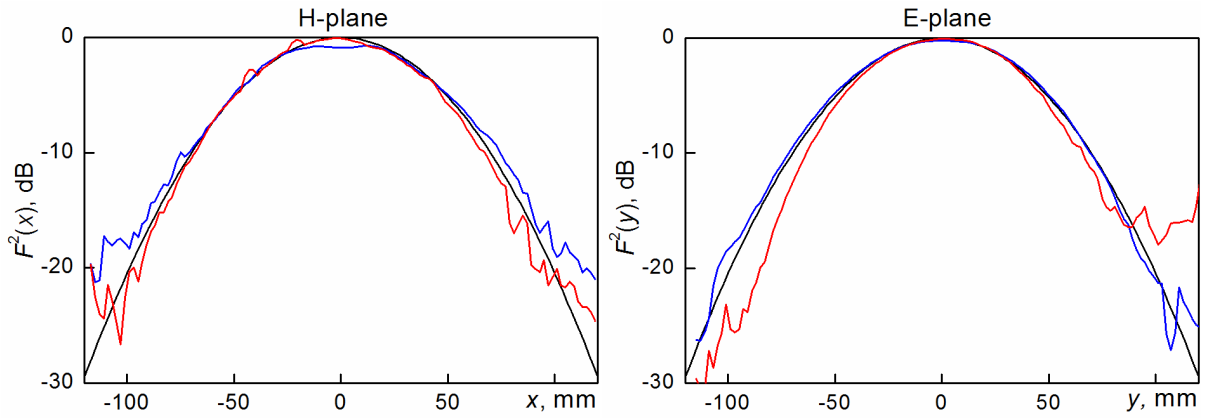

Figure 3.24 DD power profiles in the beam cross section at $z = 1000$ mm

The blue curves show the measured values for the receiving channel R_X, the red curves represent the power profile of the transmitting channel T_X. The calculated data of the Gaussian beam (2.10, 2.11) for a beamwidth in the DD aperture being equal to $\omega_0 = 16.3$ mm are represented by the black curves.

As can be seen from Figures 3.22 – 3.24, the measured field distributions can be satisfactorily approximated by Gaussian beams and any discrepancies between calculated and measured values are basically caused by field re-reflections between the feed horn and the lens of the antenna (Figure 3.3) which has been used as beamguide launcher.

However, these discrepancies do not violate the chosen concept for the beamguide launcher of the Gaussian beam, which is confirmed by the longitudinal beam profile – Figures 3.25 – 3.26 (solid line – calculated curve (2.10), asterisks – measured data from the receiving channel, circles – measured data from the transmitting channel).

Consequently, measuring results of the longitudinal and transversal field structure of the quasioptical DD confirm the correspondence with the Gaussian beam model, which is important for designing the two-reflector antenna with offset feed mentioned above – Figure 3.17.

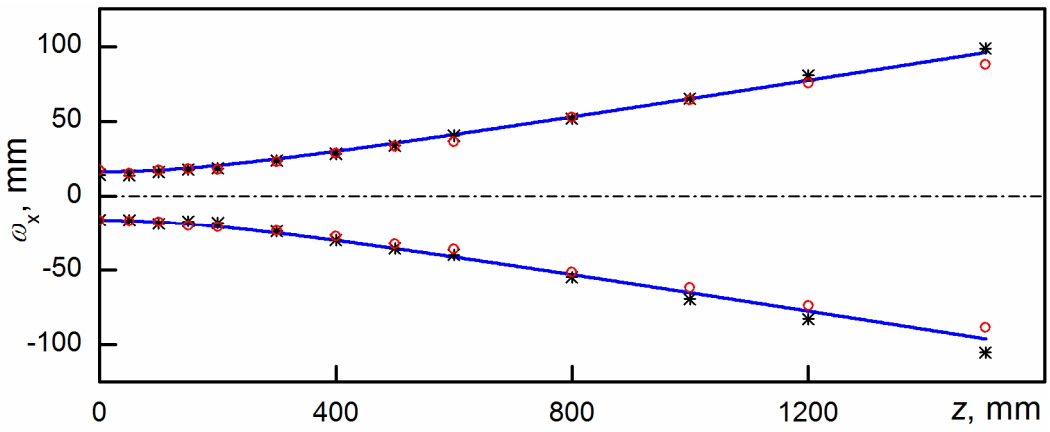

Figure 3.25 Dependence of the DD beamwidth in H-plane
(solid line – calculation; * – transmitting channel; ° – receiving channel)

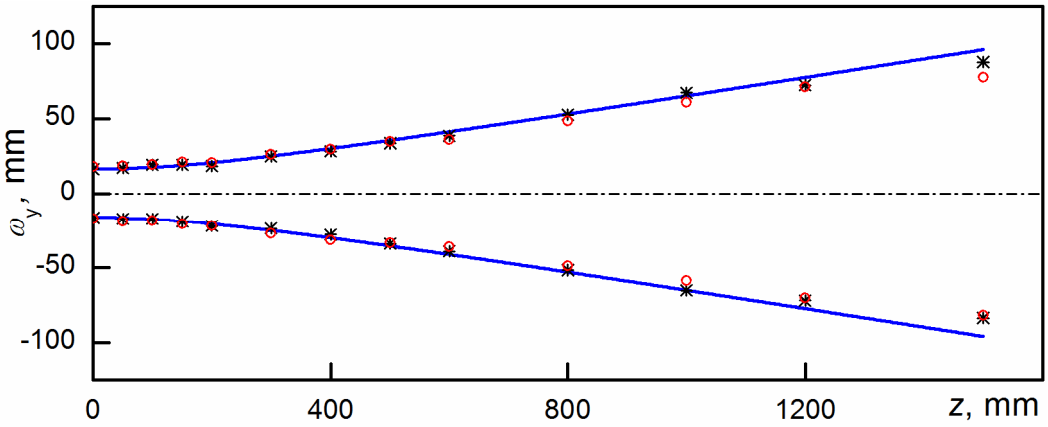

Figure 3.26 Dependence of the DD beamwidth in E-plane
(solid line – calculation; * – transmitting channel; ° – receiving channel)

The overall loss also includes the losses in the quasioptical junctions of the beam launchers which are caused by field transformation of the fundamental mode into higher-order modes because of beam diffraction in the cross-shaped junctions. The measurement of the junction reflection coefficient was carried out according to the configuration presented in Figure 3.27a, where a metal mirror is placed in diagonal of the junction. The losses can then be calculated as difference between the data obtained according to Figure 3.27a and Figure 3.27b.

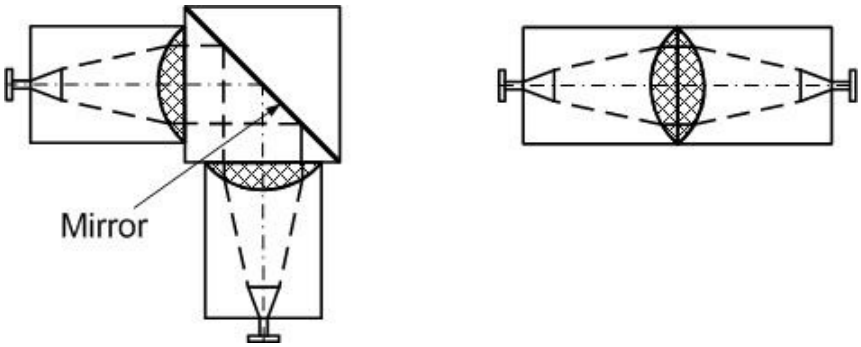

a) b)

Figure. 3.27 Measurement configuration for diffraction loss of the beam-waveguide junction

As has been found, the junction loss is not higher than 0.3 dB. A similar measurement of the junction with dielectric layer (material FR-4) in diagonal of the DD showed that the total TRL does not exceed 6.9 dB, which is quite close to the optimal DD parameters.

Another important DD parameter is the isolation between the transmitting and receiving channel, which permits to evaluate the level of the sounding signal “leakage” to the receiver and, consequently, to estimate its dynamic range. The isolation measurement has been carried out using the arrangement sketched in Figure 3.28 and applying the substitution method by comparing the attenuation data for two different configurations:

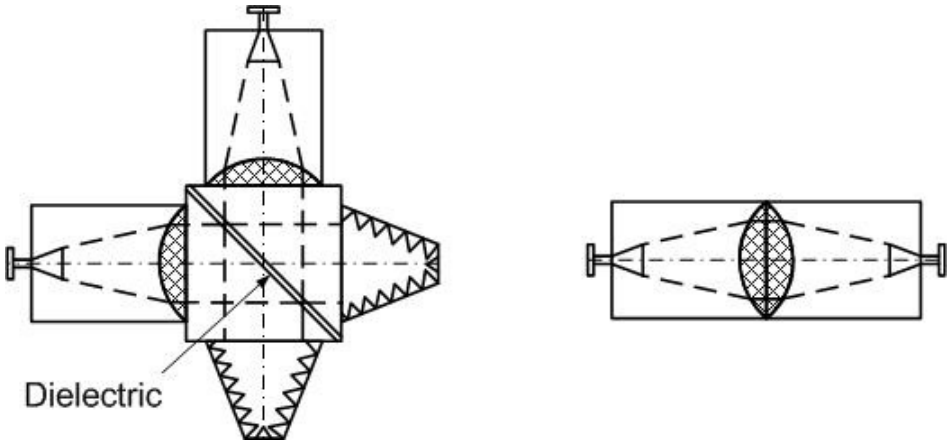

b) b)

Figure. 3.28 Measurement configuration of DD isolation in “transmit-receive” mode

“beam launcher – DD – beam launcher” (Figure 3.28a) and “beam launcher – beam launcher” (Figure 3.28b). As the measurement showed, the isolation is not less than 60 dB in a bandwidth of 10%. Moreover, a parameter estimation of the DD components showed that the obtained isolation is mainly determined by the reflection coefficient of the used matched load rather than by the junction properties. Nevertheless, the isolation between transmitting and receiving channels is quite high enough for many practical applications. It substantially exceeds the parameters of nonreciprocal ferrite circulators (< 25 dB).

3.2.3 Development of near-field offset Gregorian antenna

As was shown above, the basic argument for using the double-reflector geometry of the antenna is the necessity of minimizing back reflection from both the main and secondary reflector in order not to impair isolation between transmitting and receiving channels. Such antennas are described in detail in literature [38]. However, in the case of a quasioptical antenna-feeder path, the design of such antennas has some peculiarities. In fact, since the feed element has substantial size in comparison to wavelength, the secondary reflector is located in the near-field region of the feed. That is why the antenna calculation is based on the data of the longitudinal structure of the quasioptical beam presented in Figures 3.22 – 3.26. The radius of curvature of the feed phase front depends on the distance to the feed aperture z. It can be expressed as:

$$R_f = z\left[1+\left(\frac{k\omega_0^2}{2z}\right)^2\right], \tag{3.15}$$

where ω_0 – beamwidth radius in the feed aperture for a flat phase front. However, at distances of practical interest, the beam phase front should not differ much from a flat one. For instance, at the Fresnel distance for the Gaussian beam $z = z_f = \frac{1}{2}k\omega_0^2$, the phase incursion

$\Delta\varphi = \varphi(\omega_0) - \varphi(0) = \frac{k\omega_0^2}{2z_f}\left[1 + \left(\frac{k\omega_0^2}{2z_f}\right)^2\right]^{-1}$ at the edge of the beam cross-section $x = \omega_0$ does not exceed 30°. Then it is promising to use the "near-field" double-reflector Cassegrain antenna configuration described in paper [41] – Figure 3.29a. The secondary

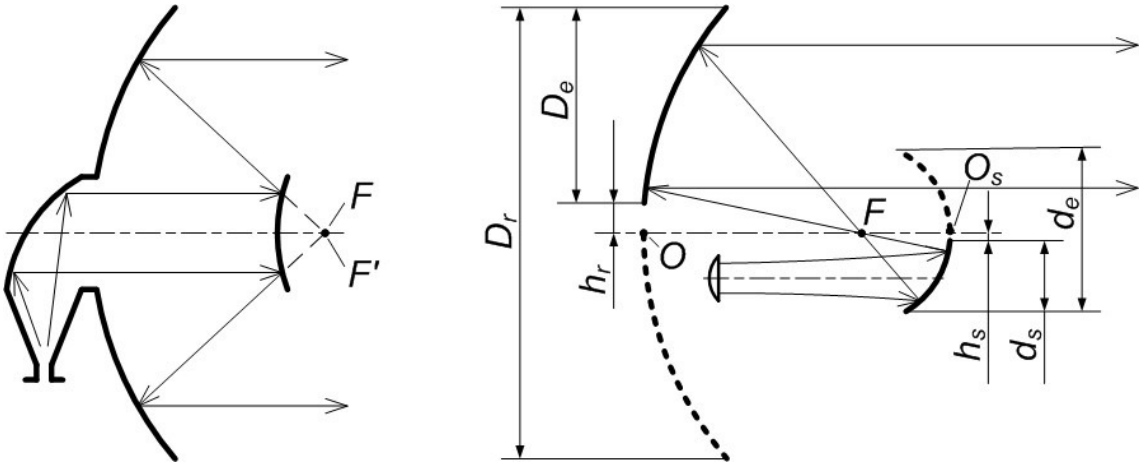

a) b)

Figure 3.29 Design of double-mirror near-field antennas using Cassegrainian geometry – a) and offset Gregorian geometry – b)

reflector has hyperbolic shape, the apparent focus of which F' coincides with the focus of the main parabolic reflector F. In this case, the secondary reflector transforms the parallel beam of the feed into a spherical divergent wave, the center of which coincides with the focus of the main reflector.

At the same time, as has been shown in paper [42], the use of a concave parabolic subreflector (Gregorian configuration – Figure 3.29b) provides both a lower sidelobe level and lower cross-polarization radiation than the traditional Cassegrainian design (Figure 3.29a). A further improvement of the "near-field" Gregorian antenna may be achieved by using an offset feed geometry – Figure 3.29b, in which any shadowing of the main reflector is missing.

The analytical description of the amplitude and phase distribution, taking into account an offset antenna geometry and a near-field placement of the feed, is a quite complicated problem. Therefore, the basic dimensions of the antenna were approximately defined using the geometrical approximation method for a part of the axisymmetric Gregorian configuration (solid curve in Figure 3.29b). This method is based on well-known relations [42]. Finally the dimensions of the antenna were defined more exactly during the experimental study. They are summarized in Table 3.2.

Table 3.2 Double-reflector asymmetrical antenna parameters

N	Antenna parameters	Value
1	Operating frequency, GHz	92.323
2	Diameter of equivalent axisymmetric reflector D_e, mm	400
3	Aperture size of the main reflector D_r, mm	190
4	Focus distance of the equivalent axisymmetric reflector F_r=OF, mm	100
5	Distance from lower edge of the reflector to the axis of the equivalent reflector h_r, mm	10
6	Angular size of the main reflector, deg	84.3
7	Diameter of the equivalent axisymmetric secondary reflector d_e, mm	160
8	Aperture size of the secondary reflector d_s, mm	74
9	Focus distance of the equivalent axisymmetric secondary reflector F_s =FO_s, mm	34
10	Distance from the lower edge of the secondary reflector to the axis of the equivalent secondary reflector h_s, mm	5

The main reflector and the subreflector are made of duralumin by milling with a CNC machine. An outlook of the assembled antenna is shown in Figure 3.30.

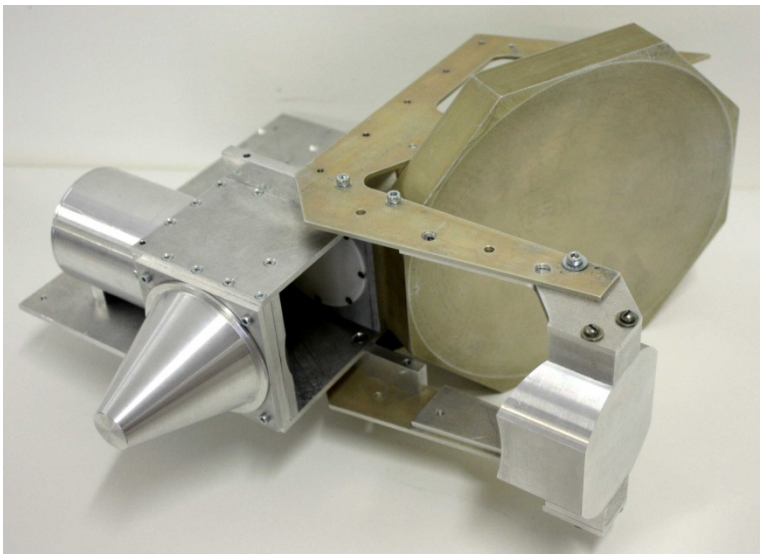

Figure 3.30 Outlook of the offset near-field Gregorian antenna with quasioptical DD

The experimental study of the antenna was carried out in an anechoic chamber using a field section scanner – Figure 3.31, for the transmitting and receiving channels of the antenna

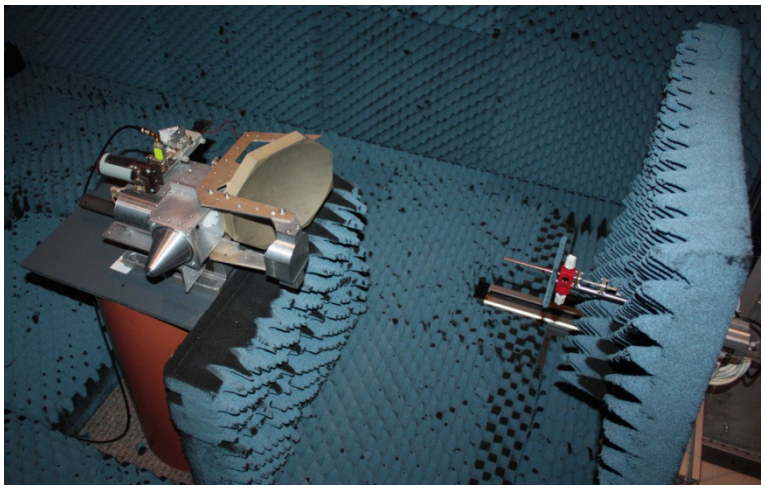

Figure 3.31 Measurement of the antenna field structure in an anechoic chamber

separately. The configuration of the measurement set-up is presented in Figure 3.32, where the distance from the antenna to the measuring plane is in the range of $z = 0 - 1500$ mm. The results are depicted in a common coordinate system (Figures 3.33 – 3.35, H-plane – at the left, E-plane – at the right). The blue curves show measured values for the receiving channel R_X, the red curves represent power profiles of the transmitting channel T_X, and the black curves correspond to a Gaussian beam (2.10, 2.11) with $\omega_0 = 48$ mm.

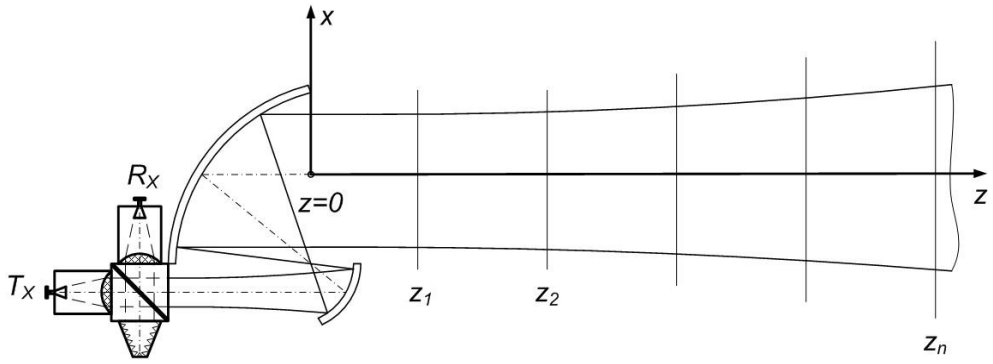

Figure 3.32 Antenna field measurement configuration

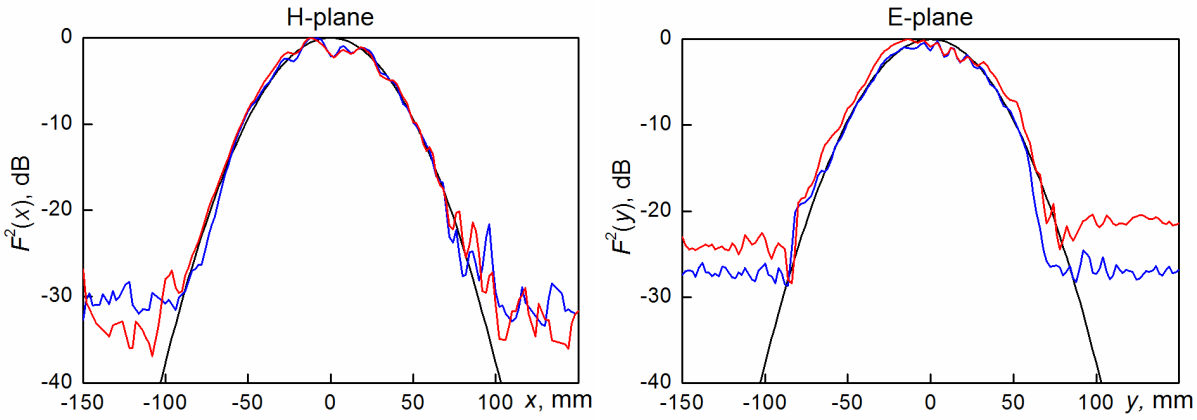

Figure 3.33 Power profile in the antenna aperture at $z = 0$ mm (dash – R_X; dots – T_X; solid line – Gaussian beam)

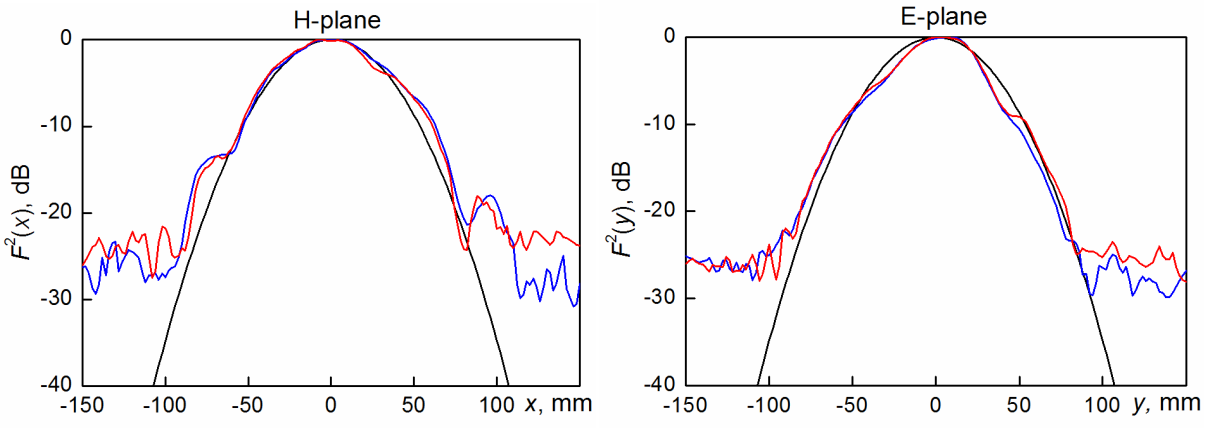

Figure 3.34 Power profile in the beam cross-section at $z = 600$ mm (dash – R_X; dots – T_X; solid line – Gaussian beam)

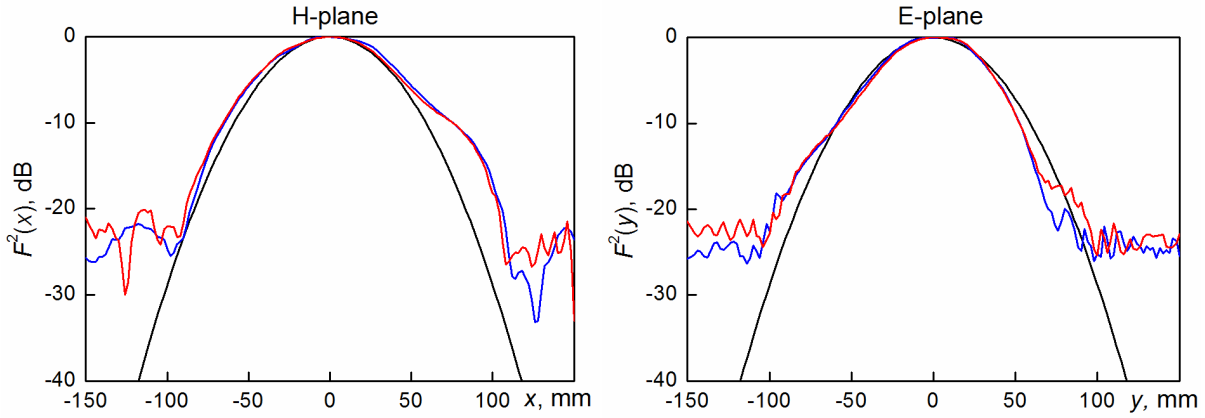

Figure 3.35 Power profile in the beam cross-section at $z = 1200$ mm (dash – R_X; dots – T_X; solid line – Gaussian beam)

As the measurements show, the value of the beamwidth in the antenna aperture well corresponds to the beamwidth ω_0 in the aperture, and the beam shape is very close to a Gaussian distribution down to a level of -20 dB over the whole range of distances z including the near-field and the far-field regions. As one can see from the measurement of the 3D antenna field distributions (Figures 3.36 – 3.37), the developed antenna provides quite a low level of side-lobes ($\leq$ -20 dB) and a high grade of axial symmetry of the radiation field. The peculiarities of the antenna field distribution mentioned above play a vital part for the operation of the radar in narrow ducts, reducing reflections from elements of the duct.

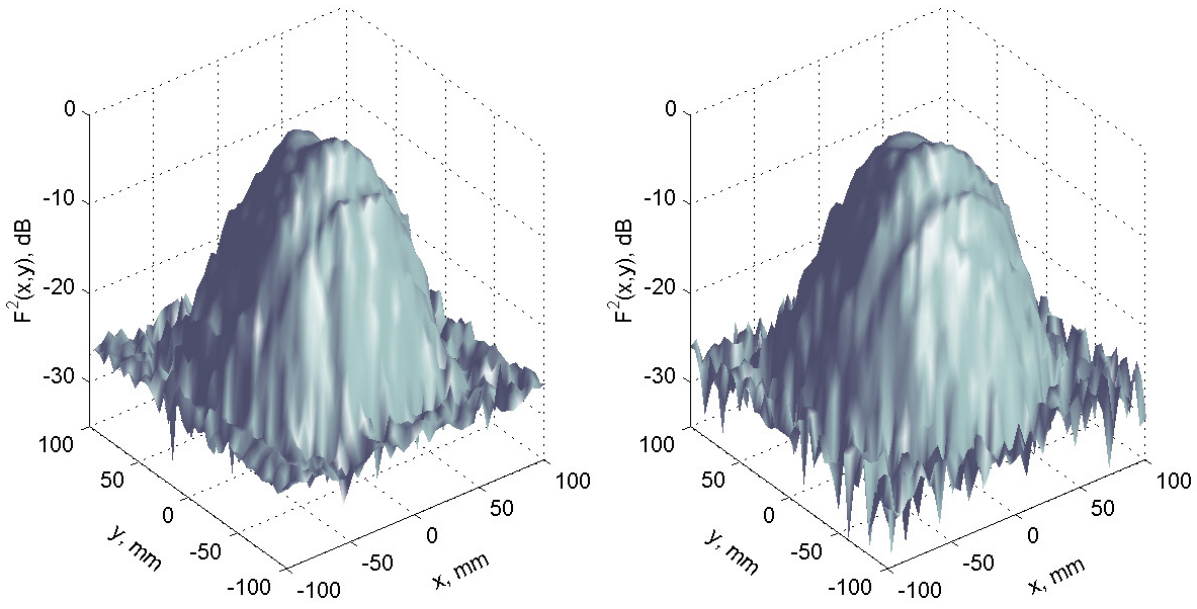

a) b)

Figure 3.36 3D field structure of the receiving channel – a) and transmitting channel – b), distance $z = 100$ mm

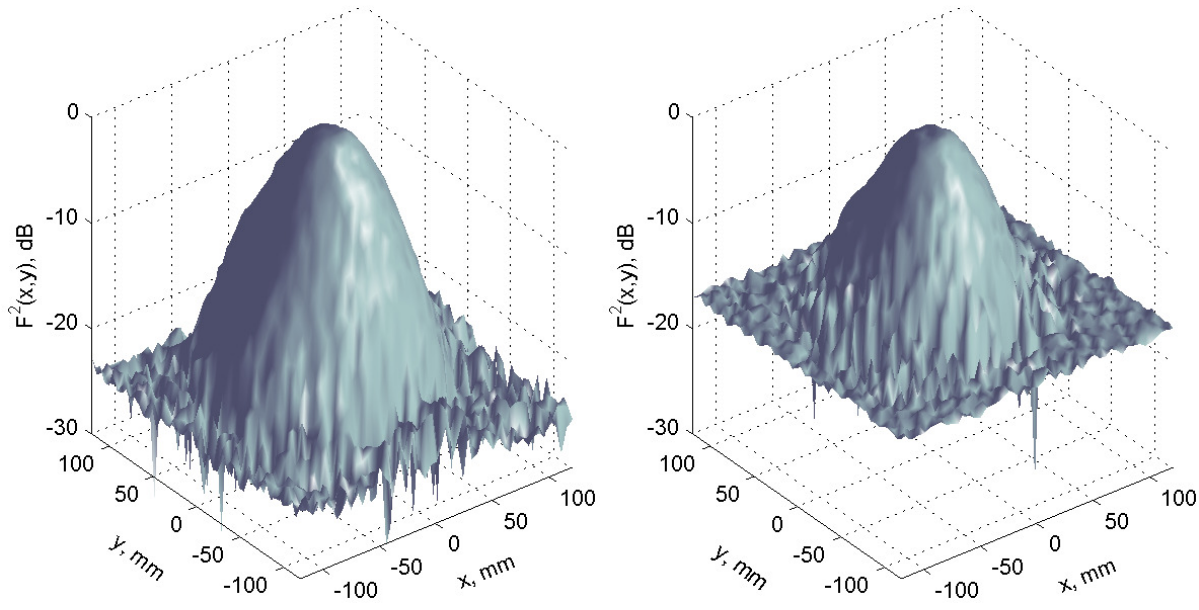

a) b)

Figure 3.37 3D field structure of the receiving channel – a) and transmitting channel – b), distance $z = 1200$ mm

Moreover, because of the low divergence of a Gaussian beam [38], the developed antenna also provides suppression of re-reflections from outside objects and confirms the advantages of Gaussian beams for sensing of disperse streams. In this respect, the conducted measurements prove the conclusions of the paper [20], as shown in Figures 3.38 and 3.39, where beamwidth dependencies on distance in both *E*- and *H*- plane are presented (solid curve

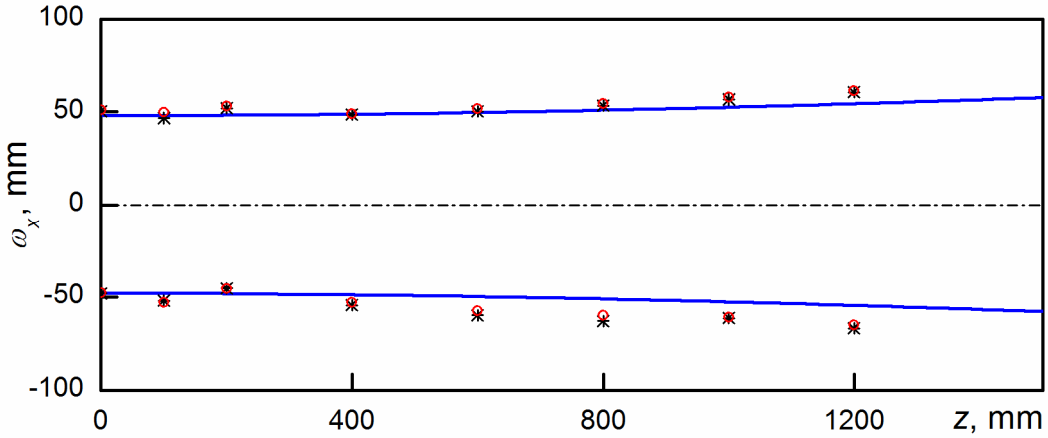

Figure 3.38 Dependence of the antenna beamwidth in H-plane on distance (solid curve – calculations; * – transmitting channel; ° – receiving channel)

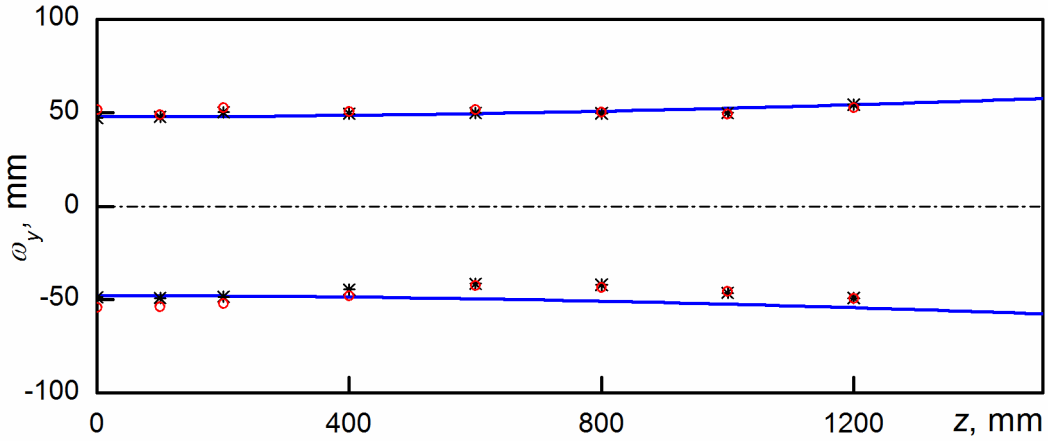

Figure 3.39 Dependence of the antenna beamwidth in E-plane on distance (solid line – calculations; * – transmitting channel; ° – receiving channel)

– calculation of a Gaussian beam, asterisks correspond to measured values for the receiving channel of the antenna and circles – transmitting antenna channel). As one can see, the initial beamwidth of the antenna stays practically constant up to half of the far-field distance of the Gaussian distribution $z = \frac{1}{2} k\omega_0^2 = 2250$ mm. At the same time, in the far-field zone of such antenna, the measured power pattern is well described by expression (3.12) and the beamwidth in the far-field zone is equal to: $2\Delta\theta_0 = \frac{1.18}{k\omega_0} = 1.4°$ at -3 dB.

3.2.4 Configuration of the mono-frequency monostatic radar-sensor

The designed antenna is used in the coherent monostatic CW radar, the configuration of which is shown in Figure 3.40 which is a modification of the bistatic radar configuration described above – Figure 3.1, where the transmitting channel output and the receiving channel input are connected to the corresponding ports of the quasioptical DD. To provide maximum possible dynamic range of the receiver, the main amplification is carried out in the Doppler frequency amplifier (DFA).

In spite of a sufficiently high isolation between the transmitting and receiving channels ($S_{TR} > 65$ dB), the leakage power from the transmitter reaches a quite significant value of $P_1 = P_T S_{TR} = 3 \cdot 10^{-8}$ W, because of a quite large transmitted power $P_T \approx 100$ mW. This power essentially exceeds that of the received signal $P_{\min} = 8kT\Delta fNF \approx 10^{-15}$ W (k – Boltzmann constant, $T = 290°$K – physical temperature of the receiver, $\Delta f = 10^4$ Hz – receiver bandwidth, $NF = 10$ dB – receiver noise figure). Since the dynamic range of the ordinary IFA quite seldom exceeds 30 dB, a simultaneous amplification of the wanted and the leakage signal leads to saturation of the receiver.

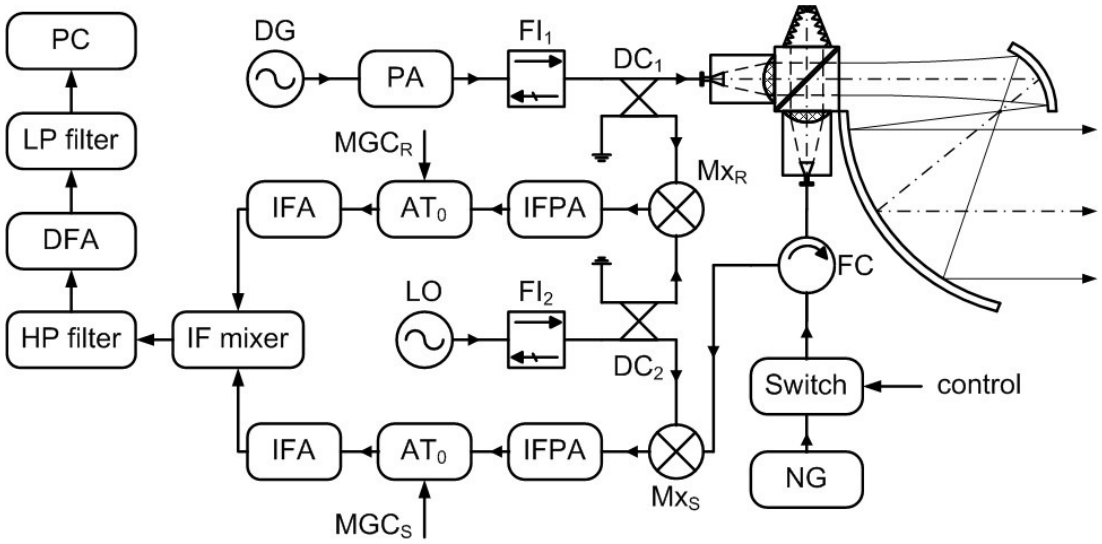

Figure 3.40 Monostatic radar configuration

On the other hand, the signal at the output of the reference channel IFA can be written as:

$$U_R(t) = U_{R0} e^{j\omega t + j\varphi_R} \tag{3.16}$$

and the wanted signal can be represented as the sum of the reflected and the leakage signals:

$$U_S(t) = U_{S0} e^{j(\omega+\omega_D)t + j\varphi_S} + U_{l0} e^{j\omega t + j\varphi_l} \tag{3.17}$$

where ω and ω_D are the operating frequency and Doppler frequency, respectively; U_{R0}, U_{S0}, U_{l0} and $\varphi_R, \varphi_S, \varphi_l$ are the amplitudes and phases of all three components. Consequently, the voltage at the output of the intermediate frequency (IF) mixer is:

$$\begin{aligned} U_D(t) = U_S \cdot U_R^* = U_{S0} U_{R0} e^{j(\omega+\omega_D)t + \varphi_S - j\omega - j\varphi_R} + \\ + U_{l0} U_{R0} e^{j\omega t + j\varphi_l - j\omega - j\varphi_R} = U_{D0} e^{j\omega_D t + \varphi_D} + U_0 e^{-j\varphi_0}. \end{aligned} \tag{3.18}$$

As one can see, there are the following components at the mixer output: the voltage at the Doppler frequency $U_{D0} \cdot \exp(j\omega_D t + j\varphi_D)$ and a low frequency product with large amplitude $U_0 >> U_{D0}$, which is caused by the transmitter leakage $U_{l0} >> U_{D0}$. This last term

is caused by a low frequency amplitude (phase) modulation of the radiated signal which, in the case of an unmodulated reflected signal, is turned into a constant component $U_0, \varphi_0 = \text{const}$. Therefore, the use of the high-pass filter (HPF) behind the IF mixer – Figure 3.40, permits to reduce the leakage influence on the Doppler frequency amplifier (DFA) and thus to increase the dynamic range of the receiver.

In order to provide the maximum of the total sensitivity of the receiver, it is necessary to meet a condition that the intrinsic noise of the Doppler signal path (IF mixer and DFA) must be substantially smaller than the noise of the microwave mixer Mx_S at the IFA input (Figure 3.40). Since the Doppler signal path is a superheterodyne receiver in the decimeter-wave band ($f_{IF} = 1 - 2$ GHz) with zero intermediate frequency, then, as experience shows, the noise figure of such a receiver usually exceeds $NF \geq 20$ dB. So the minimally detected signal is $P_d^{\min} = kT\Delta f \; NF \cong 4 \cdot 10^{-15}$ W, and the required gain of the IFA must not be less than $G_{IFA} \geq \frac{P_d^{\min}}{P_{\min}} = 10 - 100$, which corresponds to a maximum leakage signal of $P_l^{\max} \cong 10^{-7} - 10^{-6}$ W. The linear part of the amplitude characteristic for modern solid-state amplifiers substantially exceeds the mentioned value in the frequency band 1 – 2 GHz. As a result, the dynamic range of the receiver is practically determined by the ratio of the input signals of the used A/D converter.

3.2.5 Design of the mono-frequency monostatic radar-sensor

The described monostatic radar-sensor was constructed and tested. The radar includes the near-field offset antenna (Figure 3.30), a transceiver, power supply, control and interface unit which are fixed on a duralumin base (Figure 3.41). The radar was tested and its characteristics are presented in Table 3.3.

Table 3.3 Parameters of the monostatic radar-sensor

N	Parameter	Unit	Value of parameter
	1. Antenna-feeder path		
1.1	- Aperture diameter	mm	190
1.2	- Aperture beamwidth	mm	48
1.3	- Beamwidth at level of -3 dB	deg	1.4
1.4	- Sidelobe level	dB	≤ 23
1.5	- Gain	dB	42
1.6	- Aperture illumination efficiency	-	0.35
1.7	- Isolation (transmitter-receiver)	dB	≥ 65
	2. Transmitter		
2.1	- Operating frequency	GHz	92.82
2.2	- Wavelength	mm	3.23
2.3	- Average radiation power	W	0.1
2.4	- Frequency noise level (frequency mismatch - 10 kHz)	dB/Hz	≤ -90

Table 3.3 (cont'd)

3. Receiver			
3.1	- LO frequency	GHz	94.23
3.2	- Noise figure	dB	≤ 10
3.3	- Peak sensitivity	W/Hz	$\approx 1 \cdot 10^{-15}$
3.4	- Intermediate frequency	GHz	1.4 ± 0.3
3.5	- IF gain	dB	20
3.6	- Gain control range	dB	40
3.7	- High-pass filter passband	kHz	0.1 – 12
3.8	- Low-pass filter passband	kHz	0.05 – 10
4. Parameters of signal processing			
4.1	- Sampling rate	kHz	44
4.2	- ADC bit capacity	-	10
4.3	- Signal realization size	MB	1.3

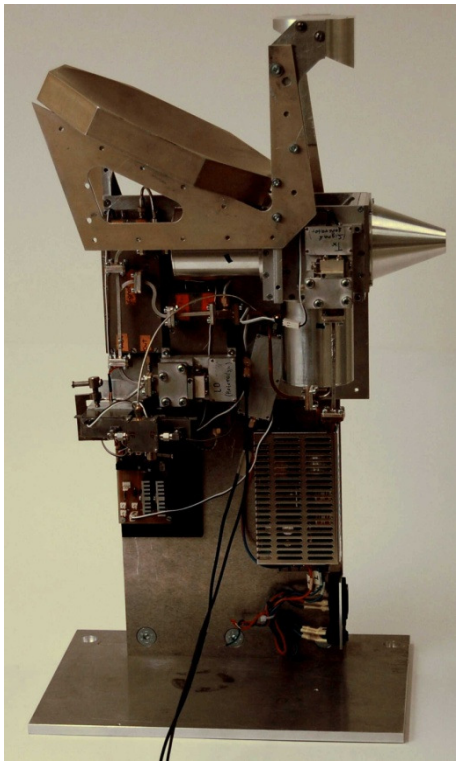

Figure 3.41 Outlook of the monostatic coherent radar

The parameters of the transceiver are very close to the previously developed transceiver for the bistatic radar (Table 3.1) and correspond to the modern state of radar technology in the short millimeter-wave band. The radar was used for measuring the characteristics of coherent signals reflected from volume scatterers such as precipitation and dust stream. For example, the spectrum of signals reflected from drizzle is shown in Figure 3.42, the energy part of which (less than -15 – -20 dB) corresponds to collective particle motion in a rain stream, and the spectrum periphery is formed by a fast amplitude modulation of reflected signals due to mutual shading of particles.

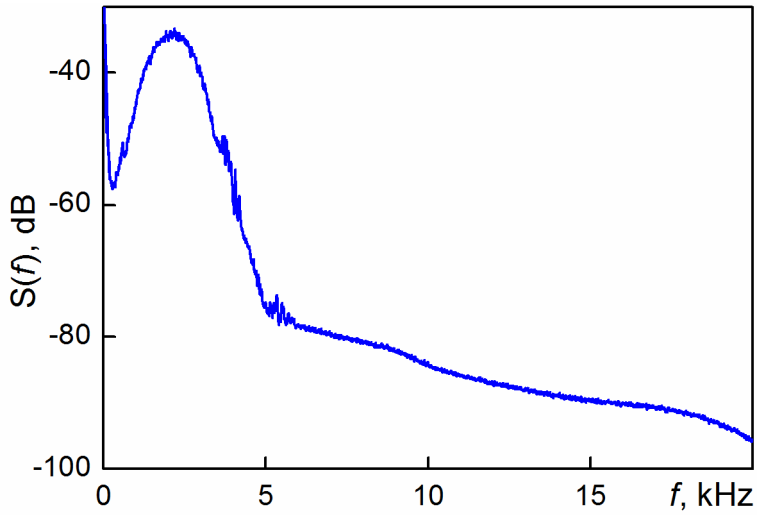

Figure 3.42 Spectrum of signals reflected from drizzle

Finally it is worth to note that the considered configuration of the monostatic radar with quasioptical antenna-feeder path can be used for almost all kinds of transmitted signals including those with pulse modulation and frequency- and phase-modulation as well, because of the high isolation between the transmitting and receiving channels and the high dynamic range of the receiver ($\geq$ 50dB).

3.3 Double-frequency bistatic radar-sensor

The double-frequency method described in section 2.3 for remote sensing of disperse streams is based on several simplifying assumptions, including the assumption of single scattering of the electromagnetic field by a particle ensemble and of a spherical particle shape. A theoretical estimation of the applicability of these assumptions is hardly possible taking into account the complexity of the electromagnetic scattering problem. Therefore, the experimental study is of strong interest for validating the proposed method.

This study should be conducted in wavebands where the necessary instrumentation exists already. In this connection, the wavebands of $\lambda_1 = 3\,\text{mm}$ and $\lambda_2 = 8\,\text{mm}$ have been chosen.

3.3.1 Configuration of the double-frequency bistatic radar-sensor

The block diagram of the W-band radar is basically the same as for the radar configuration described in section 3.1. The simplified block diagram of the Ka-band radar is presented in Figure 3.43. The Ka-band radar is also designed using a bistatic configuration, where the transmitter includes a driving generator (DG) based on IMPATT diodes and a ferrite circulator (FC_1) which is used to branch a part of the DG power into a mixer of the reference channel (Mx_R). The transmitting antenna A_T, which is connected to the output port of the FC_1, forms a Gaussian beam for illuminating the target particles. The receiver includes the reference and signal channels for compensation of the frequency fluctuations of the DG

and a local oscillator (LO), which is based on a Gunn diode with an external stabilizing high-Q resonator. A ferrite isolator (FI) provides a constant load for the DG, and the ferrite circulator FC_2 also provides branching of the LO power to the mixers of the signal and reference channels Mx_S and Mx_R, respectively.

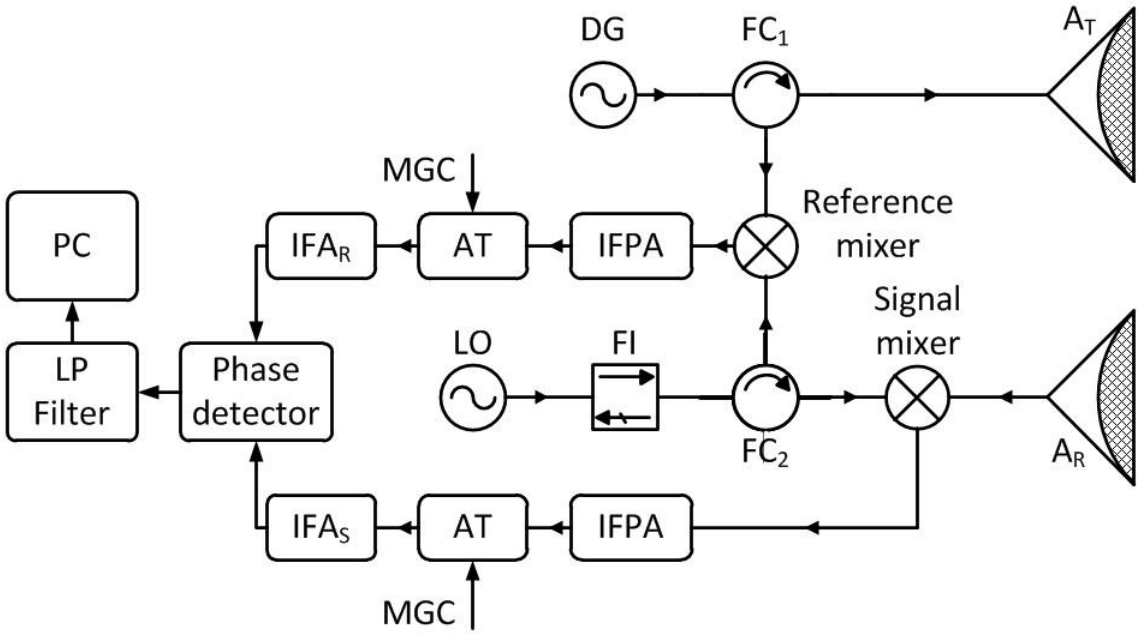

Figure 3.43 Block diagram of 8 mm radar-sensor

The mixers are realized using balanced circuits with Schottky diodes providing a good SNR performance. The intermediate-frequency amplifiers of the signal and reference channels consist of a preamplifier (IFPA), an electrically controlled attenuator (AT_0) for manual gain control (MGC), and a main intermediate-frequency amplifier (IFA). The signals from the reference and signal IFA's enter a phase detector to extract the Doppler frequency shift of the signal reflected from the particle ensemble. Then the extracted signal passes through the LPF and arrives at the analogue-to-digital (A/D) converter and PC.

3.3.2 Antenna system of the double-frequency bistatic radar-sensor

In order to form a Gaussian beam, the advantages of which have already been described in section 2.1, a horn-lens antenna (HLA) was used. The HLA permits to form the necessary amplitude-phase distribution in the antenna aperture with low field amplitude on the aperture edge for beam forming which is close to the Gaussian beam parameters. The antenna was simulated in HFSS environment, its configuration is presented in Figure 3.44a. It consists of a horn feed and a dielectric lens. Figure 3.44b shows the simulated amplitude-phase distribution in the principal planes of the antenna confirming that the horn illuminates only the central area of the lens. To form a Gaussian power pattern, the aperture taper exceeds 30 dB and absorbing material is placed on the inner surface of the lens holder in order to suppress lateral radiation of the horn. This also prevents re-reflections of sidelobe radiation of the horn feed from the inner surface of the antenna housing and thus a distortion of the Gaussian beam.

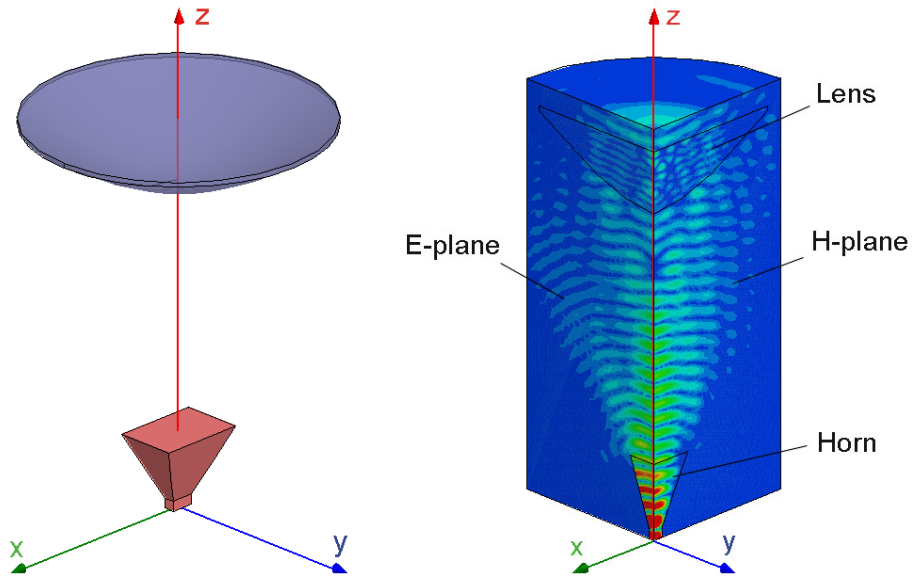

a) b)

Figure 3.44 Simulation of the horn-lens antenna in HFSS environment:
a) – calculating model b) – field distribution

Finally, the antenna system of the Ka-band radar consists of two identical horn-lens antennas (Figure 3.45), which are assembled on a common metal plate.

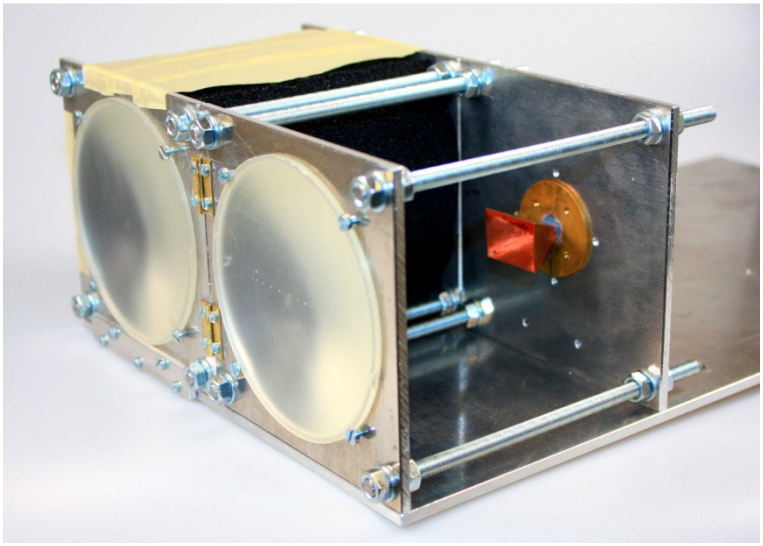

Figure 3.45 HLA design

The antennas may be adjusted by means of threaded rods with nuts which permit to regulate the relative positions of the horn and the lens. The antenna lens flanges are connected to each other by joints, which enable to adjust the convergence angle of the antenna beams with quite high accuracy. The lenses are made of polystyrene with dielectric constant of $\varepsilon = 2.61$ (loss tangent of $\tan(\delta) < 0.001$), the horn is made of copper by the galvanoplastic method and soldered into a brass flange. For suppression of the sidelobe radiation of the horn, a special

muff made of sheet-absorbing material is placed between the horn and the lens flanges (in Figure 3.45, the absorber is removed from one of the antennas for better viewing).

The antennas designed were experimentally studied in an anechoic chamber using a field scanner device (Figure 3.46).

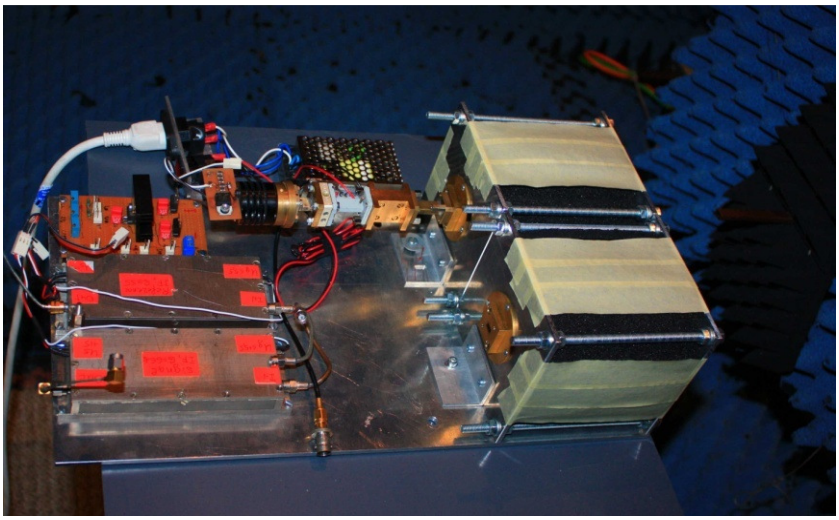

Figure 3.46 Measurement of the HLA in an anechoic chamber

Figures 3.47 and 3.48 show 3D power distributions of the transmitting and receiving antenna fields at distances of $z = 200$ mm and $z = 1200$ mm from the antenna apertures, respectively. The field distributions of the receiving (Figure 3.47a) and transmitting (Figure 3.47b) antenna near the aperture ($z = 200$ mm) are slightly different from each other

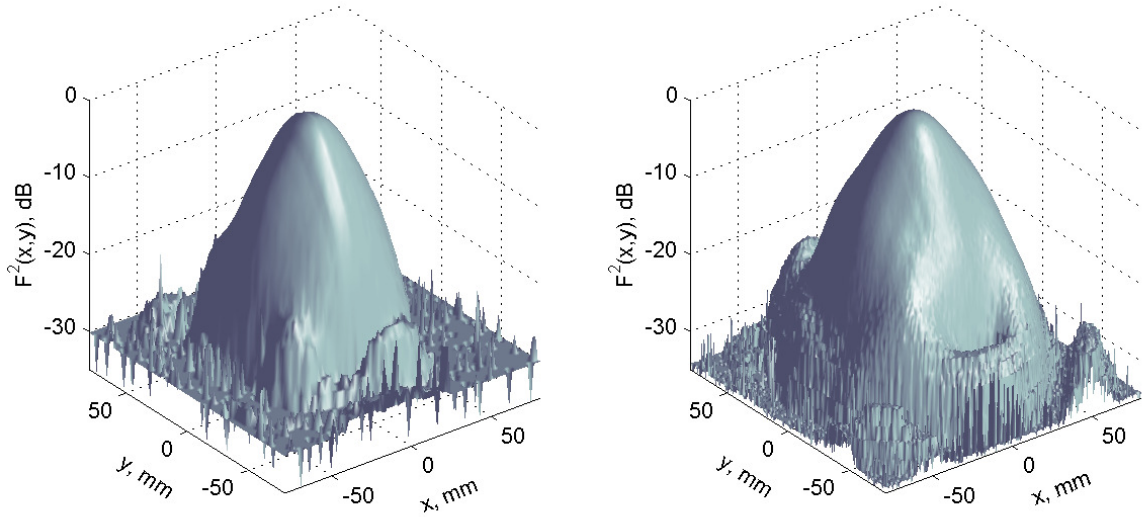

a) b)

Figure 3.47 3D power profile of the antennas, $z = 200$ mm: a) – R_X ; b) – T_X

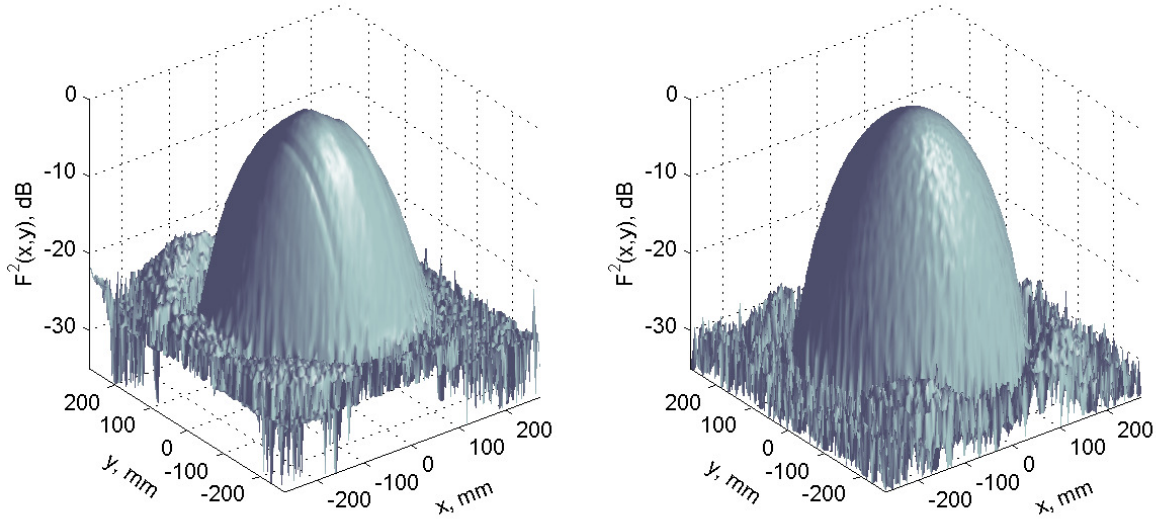

a) b)

Figure 3.48 3D power profile of the antennas, $z = 1200$ mm: a) – R_X ; b) – T_X

at the periphery of the beam owing to field diffraction by elements of the antenna construction. However, at a distance of z = 1200 mm, the field distribution for both antennas is basically the same (Figure 3.48).

Considering the field distribution in the principal planes at different distances from the aperture of $z = 0$, 100, 600, and 1200 mm (Figures 3.49 – 3.52), one can observe the coincidence of the beam obtained with a Gaussian distribution (black curve, H-plane – at the left, E-plane – at the right, lens diameter $d = 90$ mm). The blue curves show measured values for the receiving channel R_X and the red ones represent the power profiles of the transmitting channel T_X, for a beamwidth in the antenna aperture of $\omega_0 = 27$ mm. The measured field distributions are satisfactorily approximated by the Gaussian beam, any differences

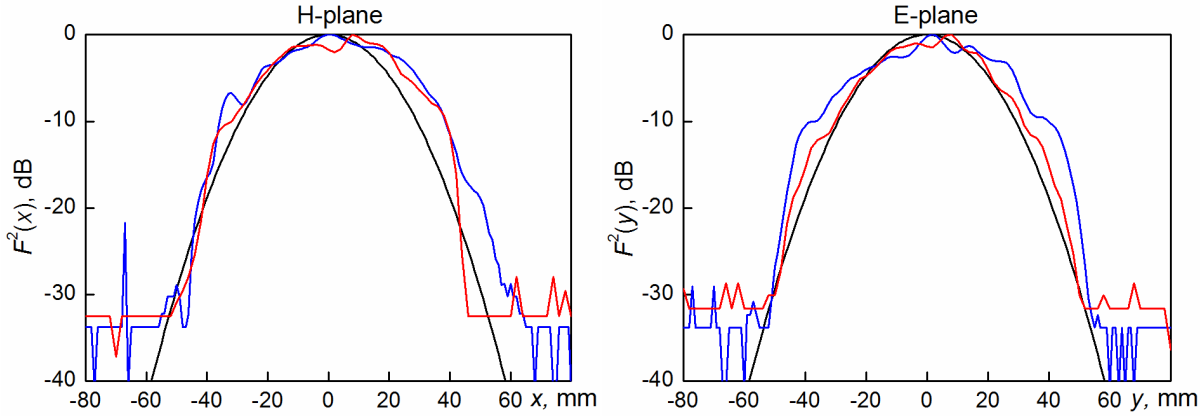

Figure 3.49 Power profile of the beam at $z = 0$ mm

(blue – R_X ; red – T_X ; black – Gaussian beam)

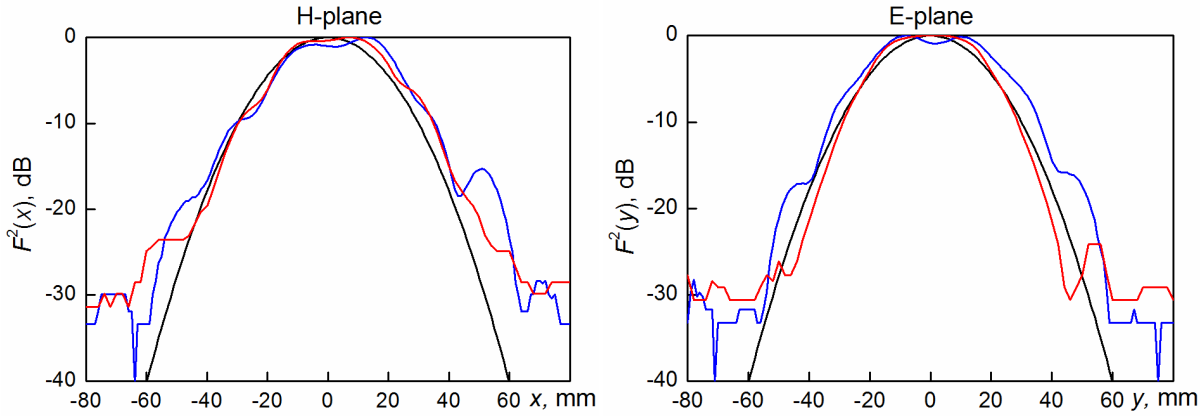

Figure 3.50 Power profile of the beam at $z = 100$ mm

(blue – R_X; red – T_X; black – Gaussian beam)

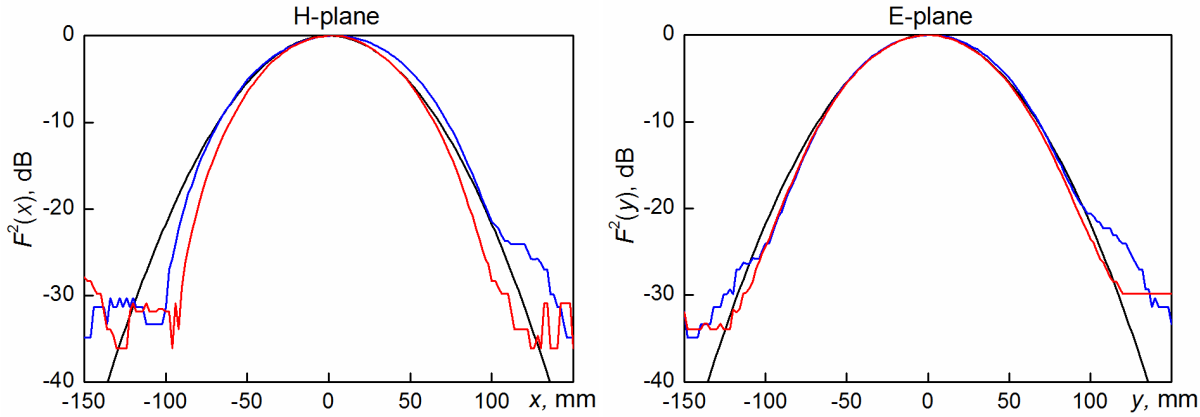

Figure 3.51 Power profile of the beam at $z = 600$ mm

(blue – R_X; red – T_X; black – Gaussian beam)

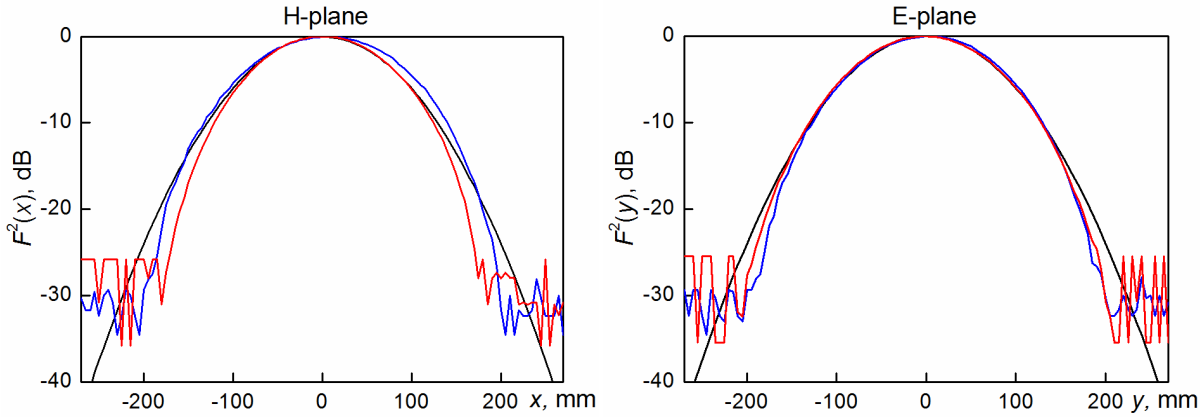

Figure 3.52 Power profile of the beam at $z = 1200$ mm

(blue – R_X; red – T_X; black – Gaussian beam)

are basically caused by field re-reflections from the HLA elements and the interaction between the measuring probe and the HLA close to the aperture.

Nevertheless, the discrepancies mentioned above do not violate the chosen concept of the AFP design using Gaussian beams, which is confirmed by the dependencies of the beamwidth on distance z – Figure 3.53 – 3.54 (solid curve – calculated data (2.10), asterisks – experimental data for the receiving antenna, circles – experimental data for the transmitting antenna).

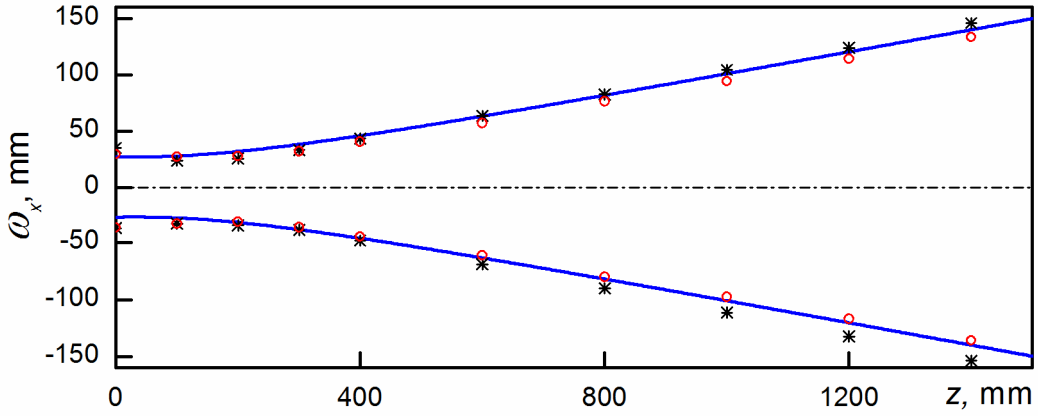

Figure 3.53 Beamwidth of the antennas in H-plane
(solid curve – calculations; * – transmitting antenna; ° – receiving antenna)

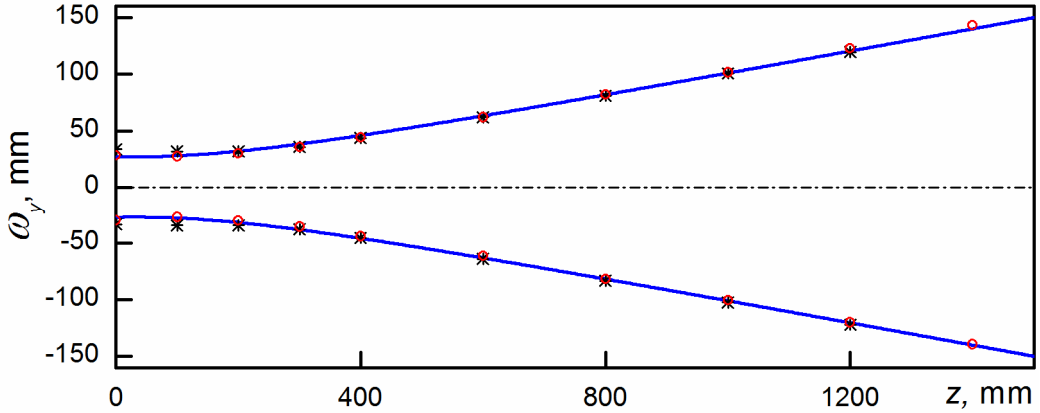

Figure 3.54 Beamwidth of the antennas in E-plane
(solid curve – calculations; * – transmitting antenna; ° – receiving antenna)

Hence the measured longitudinal and transversal field structures of the developed antennas prove a close correspondence between the measured data and a Gaussian beam, which enables to use the expressions (2.10) and (2.11) for the effective scattering volume V_{ef} calculation.

3.3.3 Design of the double-frequency radar-sensor

For calibration of the antenna systems of W-band and K_a-band frequency channels, it is necessary to provide an antenna pattern overlap in the same region of the disperse stream. Therefore, the radar construction provides beam interception of both frequency channels as shown in Figure 3.55, where the relative position of the transmitting and receiving antenna

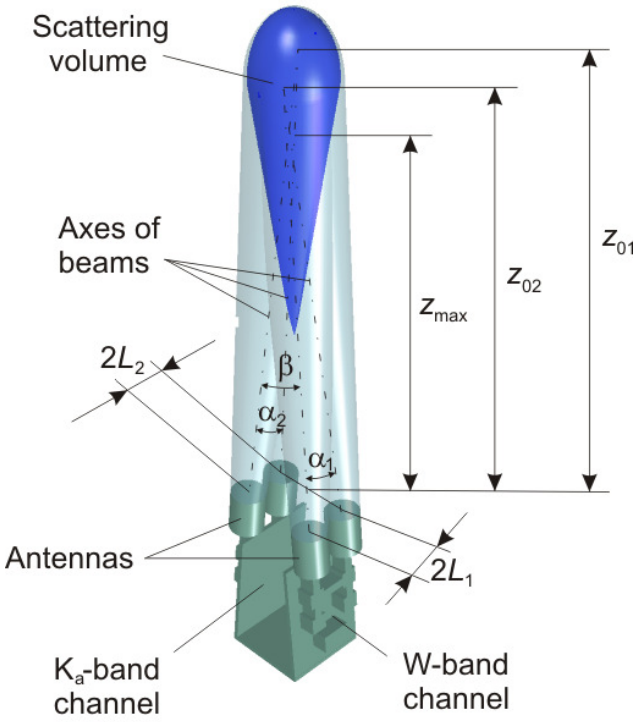

Figure 3.55 Configuration of the radar-sensor beams

beams is shown. The antenna beams of each frequency channel intercept at an angle α and at a distance z_0 from the antenna apertures, the phase centers of which are spaced by a distance $2L$. Subscript 1 represents the parameters of the W-band channel and subscript 2 – the K_a-band channel. The longitudinal axes of both channels converge at an angle β at a distance z_{max}, which corresponds to maximum illumination of the scattering volume (Figure 3.3). Moreover, for both channels this distance z_{max} has the same value. The parameters of the beam convergence are given in Table 3.4.

Table 3.4 Parameters of antenna beam convergence

Parameter	W-band channel	K_a-band channel
λ, mm	3.23	8.5
α, °	1	2
L, mm	35	55
Z_{max}, m	0.62	0.61
z_0, m	2.005	1.575
V_{ef}, 1/m	9.5	18.9

In Figure 3.56, an outlook of the designed bistatic double-frequency radar-sensor is shown. The frequency channels are fixed on both sides of a robust metal plate (W-band frequency channel on the left, Ka-band frequency channel on the right). The W-band channel is inclined relatively to the vertical axis at an angle of β=10 deg in order to form a common scattering volume for both radars.

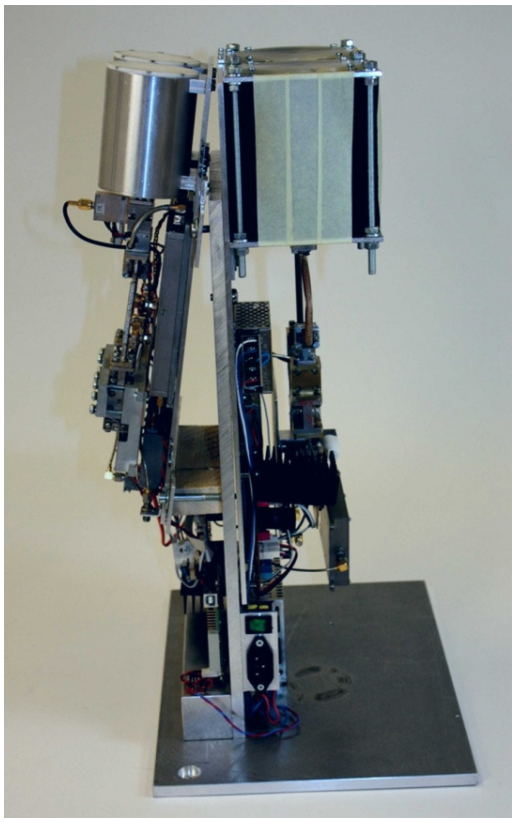

Figure 3.56 Outlook of the bistatic double-frequency radar-sensor

Each radar has its own supply board which is fed by power supply units with output voltage of 25 V to decrease any influence of joint line interference. In addition, both radars are controlled by an interface unit which is connected to a PC providing power control, calibration of the radar sensitivity by a built-in noise generator, and gain control. The parameters of the double-frequency radar-sensor measured during test are presented in Table 3.5, an example of the spectrum of a reflected signal is shown in Figure 3.57.

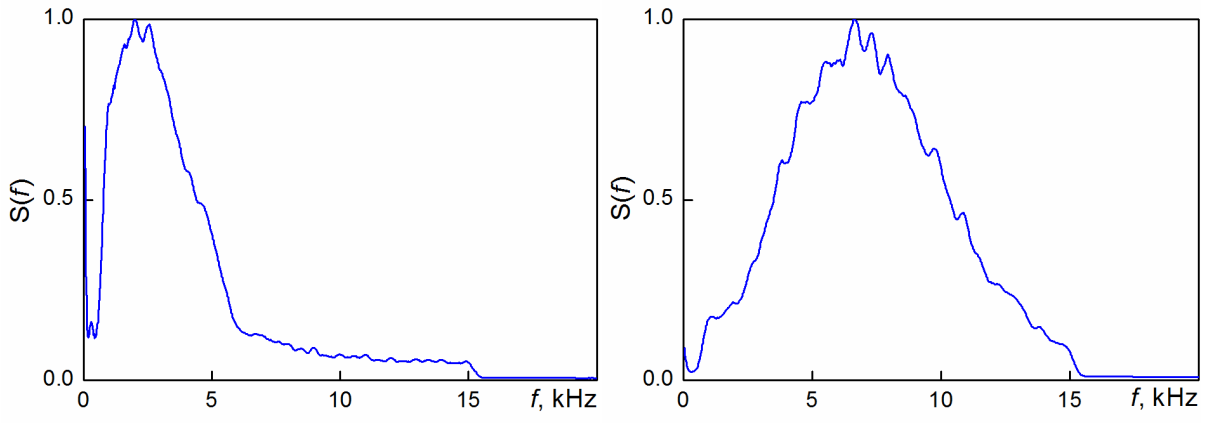

a) b)

Figure 3.57 Spectrum of the signal reflected from sand particles:
K_a-band channel – a), W-band channel – b)

Table 3.5 Parameters of the double-frequency radar-sensor

№	Parameter	W-band channel	K_a-band channel
	1. Antenna-feeder path		
1.1	- Aperture diameter, mm	60	90
1.2	- Beamwidth in aperture, mm	18.5	27
1.3	- -3dB beamwidth in far field zone, deg	4.1	6
1.4	- Sidelobe level, dB	≤ 26	≤ 25
1.5	- Antenna gain, dB	32.82	29.26
1.6	- Aperture efficiency	0.56	0.76
1.7	- Transmitter-receiver isolation, dB	≥ 80	≥ 80
1.8	- Convergence angle ($2\alpha_a$), deg	1	2
1.9	- Distance between antennas ($2L$), mm	60	110
1.10	- Distance to interception point (z_0), m	2.005	1.575
	2. Transmitter unit		
2.1	- Operating frequency, GHz	92.82	35.29
2.2	- Wavelength, mm	3.23	8.5
2.3	- Average radiation power, W	0.1	0.04
2.4	- Frequency noise level, dB/Hz (frequency mismatch – 10 kHz)	$\leq$ -90	$\leq$ -90
	3. Receiver unit		
3.1	- LO frequency, GHz	94.23	34.05
3.2	- Noise figure, dB	≤ 10	≤ 7.94
3.3	- Peak sensitivity, W/Hz	$\approx 1\ 10^{-19}$	$\approx 3\ 10^{-20}$
3.4	- Intermediate frequency, GHz	1.4 ± 0.3	1.2 ± 0.3
3.5	- IF gain, dB	80	62
3.6	- Gain control range, dB	≥ 25	≥ 25
3.7	- LPF passband,	0 – 15	0 – 15
	4. Parameters of signal processing		
4.1	- Sampling rate, kHz	44	44
4.2	- A/D converter bit capacity	10	10
4.3	- Size of signal realization, MB	1.3	1.3

The signal presented is reflected from a monodisperse stream of sand particles with diameter 0.96 mm for both the Ka-band frequency channel (Figure 3.57a) and the W-band frequency channel (Figure 3.57b). The measurement was carried out in an experimental set-up using a designed ejecting particle dispenser which is described in section 4.1. The large width of the spectrum can be explained by air stream turbulences in the duct and by peculiarities of the ejecting particle dispenser operation.

3.4 Conclusions to Chapter 3

As a result of the study presented in Chapter 3, it is possible to draw the following conclusions:

1. A bistatic mono-frequency radar-sensor in W-band has been developed, constructed, and studied. To provide coherent signal processing for the superheterodyne receiver configuration, the principle of a drifting intermediate frequency is used which permits to compensate independent frequency fluctuations of transmitter and local oscillator of the receiver. For calibration of the receiver sensitivity, the built-in device is used which is based on a solid-state noise generator.

2. To form a Gaussian beam for the mono-frequency bistatic radar-sensor in W-band, a horn-lens antenna has been simulated and developed. As the measurement shows, the formed antenna beam well coincides with a Gaussian distribution down to -20 dB level.

3. The bistatic configuration of the developed mono-frequency radar-sensor provides high isolation between receiver and transmitter (≥ 60 dB), which permits to obtain a noise-figure of not higher than 10 dB. The transmitter channel is equipped with an output amplifier based on a power combiner for 4 IMPATT diodes which provides a radiated power of about 100 mW. The output signal from the sensor is digitized in an A/D converter and processed in a PC.

4. A correlation method for signal processing of noise-like signals from disperse streams is proposed and studied. The method is based on a distinction of the fine structure of the correlation functions for the reflected signal and for thermal noise. It is shown that using a wide receiver bandwidth and long observation time lead to an increase of the signal-to-noise ratio by up to 20 dB. The efficiency of this method strongly depends on the influence of pulse and harmonic clutter which must be taken into account in applying the proposed method.

5. The configuration of a monostatic radar-sensor on the base of a quasioptical antenna-feeder path has been developed, studied, and tested. The use of a cross-shaped junction of quasioptical beams with a dielectric film in the diagonal section provides high isolation between transmitter and receiver (> 60 dB) and allows operation of the transceiver with a common antenna in W-band.

6. The optimal parameters of a quasioptical duplex device have been found to provide minimal transmit-receive loss. The experimental study of the device confirms the calculated parameters and furthermore shows that the transmit-receive loss does not exceed 6.9 dB, that the isolation between transmitter and receiver exceeds 60 dB, and that the output beam well coincides with a Gaussian shape.

7. An offset near-field Gregorian antenna has been developed and studied experimentally. The antenna provides lack of back reflection to the feed which is necessary to provide the CW mode of radar operation. Because of the specially chosen amplitude distribution in the feed aperture, the shape of the antenna power pattern can well be approximated by a Gaussian beam (down to -20 dB) which strongly decreases any influence of outside re-reflections on radar operation.

8. A mono-frequency monostatic radar-sensor has been developed and tested on the base of the near-field offset Gregorian antenna and a quasioptical feeder path, which provides transceiver operation with a common antenna in CW mode. The peculiarities of the radar configuration permit to substantially suppress any transmitter leakage to the receiver and thus provides a large dynamic range (> 50 dB) in the CW mode.

9. A double-frequency bistatic radar-sensor in CW mode has been developed, constructed, and studied. The sensor operates in W- and K_a-bands, its construction provides antenna beam convergence for both radars, synchronous data input into the PC, and permits to minimize any influence of re-reflections from elements of the experimental set-up construction.

Chapter 4

Experimental study of remote sensing of disperse streams

4.1 Development of the experimental set-up

4.1.1 Experimental set-up configuration

For measuring the parameters of disperse streams, the experimental set-up is based on a construction which has been produced by DURAG GROUP company. The configuration of the set-up is shown in Figure 4.1. It consists of a fan, a dispenser of particles, and an air duct,

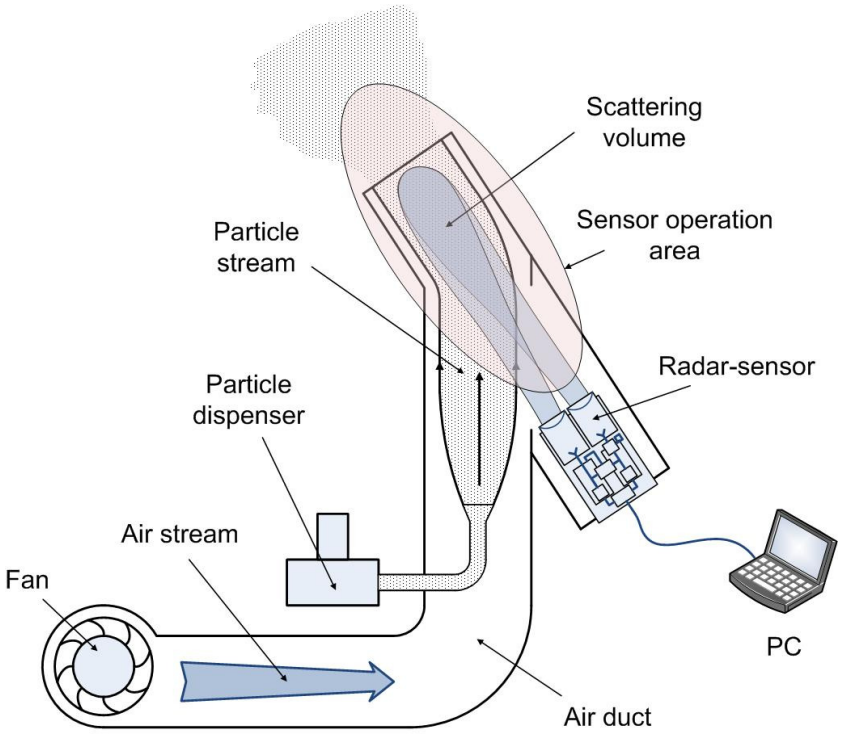

Figure 4.1 Experimental set-up configuration

in which the scattering volume of the radar-sensor is located. The fan forms the air stream which passes through the duct where a disperse stream is generated by spraying a dosed number of particles into the air stream using a particle dispenser. Then the particle stream appears in the sensor operation area and finally comes out into atmosphere.

The outlook of the experimental set-up is shown in Figure 4.2. In the foreground, there is the fan which generates an air stream into the rectangular duct that contains the bend and a transition to a circular cross-section. The bottom part of the duct is made of stainless steel and contains a tapered section, the confuser, and then a smoothly divergent section, the diffuser, which serve for air stream stabilization. The top part of the air duct is a polyethylene pipe which splits in two branches, one of them is inclined at an angle of 20° to the vertical axis (Figure 4.1). The radar-sensor is fixed to the bottom port of the inclined branch (Figure 4.2), which permits to direct the radar beam longitudinally to the pipe axis. It thus provides minimal influence of the pipe walls on the reflected signal.

Figure 4.2 Outlook of the experimental set-up

The particles under test are fed into the air stream in the narrowest cross-section of the duct where the stream velocity is maximal to promote most effective particle spraying. The inner radius of the opening at the radar beam insertion is made equal to the size of the antenna apertures in order to minimize penetration of the particles into the branch where the radar sensor is located. The rotary speed of the fan may be controlled that permits to regulate stream velocity from 1 to 12 m/s (meter per second). For protecting the entry port of the fan from outside objects, a special air filter is used.

In order to form a disperse stream with given physical characteristics (concentration and average particle size), two specimens of a special device have been developed and studied for spraying a given number of particles per certain time interval into the air stream.

4.1.2 Study of a screw dispenser for the experimental set-up

The screw dispenser is a part of equipment produced by DURAG GROUP. Its principle of operation is briefly explained referring to Figure 4.3. The particles under test are directly delivered from a container into the main air stream by means of a screw conveyor. Their number is defined by the conveyor speed.

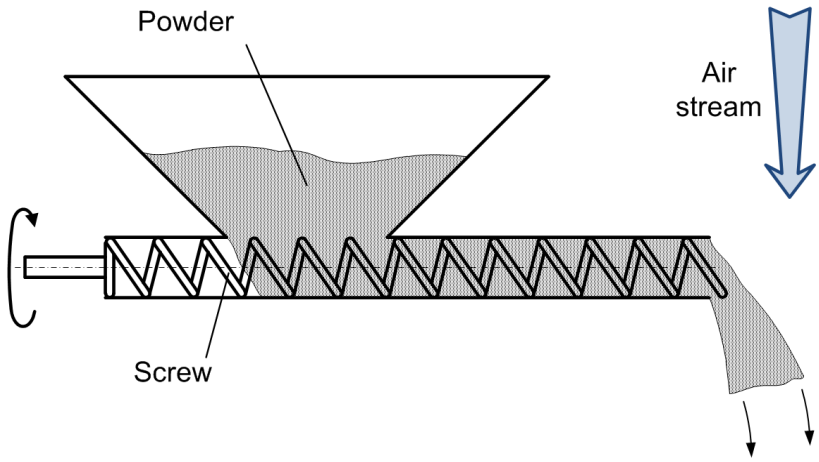

Figure 4.3 Screw dispenser configuration

Figure 4.4a shows the outlook of the used screw dispenser and Figure 4.4b the view from the side of the particle container.

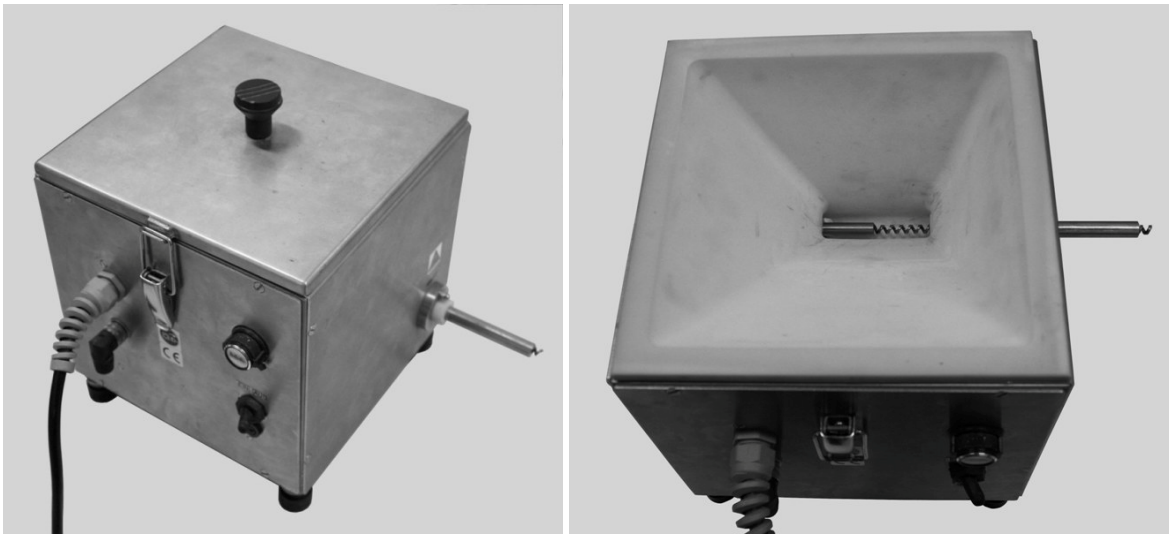

a) b)

Figure 4.4 Outlook of the screw dispenser

For carrying out the experimental study of the disperse stream, the screw dispenser is calibrated with particles of different size ($d = 29.2\ \mu$m; 44.5 μm; 84 μm; and 152 μm). The data obtained have been presented in Figure 4.5, different curves correspond to different

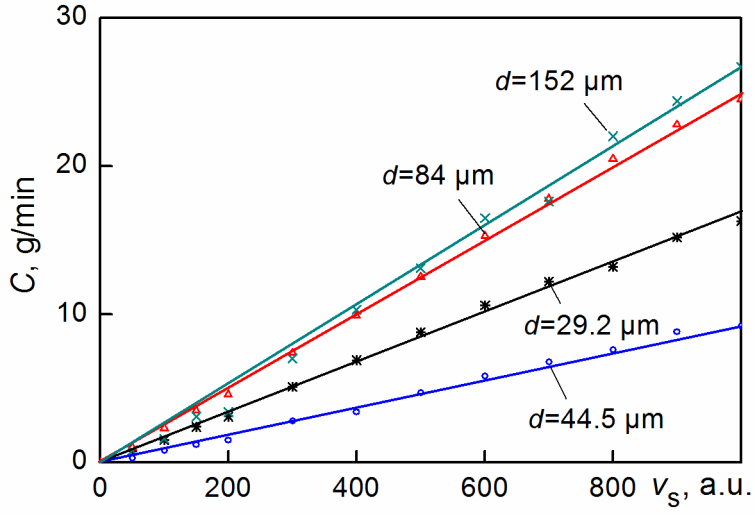

Figure 4.5 Powder consumption dependency on screw conveyor speed

particle diameters. As can be seen, the dependencies obtained are practically linear so that the particle consumption can be expressed by:

$$C = k_d \cdot v_s \tag{4.1}$$

where v_s – screw speed scale reading, k_d – coefficient of proportionality depending on particle size. The measured values of the coefficient k_d are given in Table 4.1 for powders of different particle size.

Table 4.1 Parameters of powder consumption for screw dispenser

d , μm	29.2	44.5	84	152
k_d	0.017	0.0094	0.025	0.0267

The screw dispenser is quite simple in operation and calibration, but at the same time it has several serious disadvantages:

- For small particles (< 10 μm), a coagulation process is observed when powder particles stick together forming particle clusters, thus producing an inhomogeneous disperse stream;
- Particles accumulate on elements of the fan leading to errors in the consumption measurement.

4.1.3 Development of an ejecting dispenser for the experimental set-up

A dispenser based on the ejection principle has been designed and studied. The developed dispenser provides spraying of particles from 5 μm up to 1 mm in size. Its configuration is presented in Figure 4.6. The particles under test are placed into a cylindrical

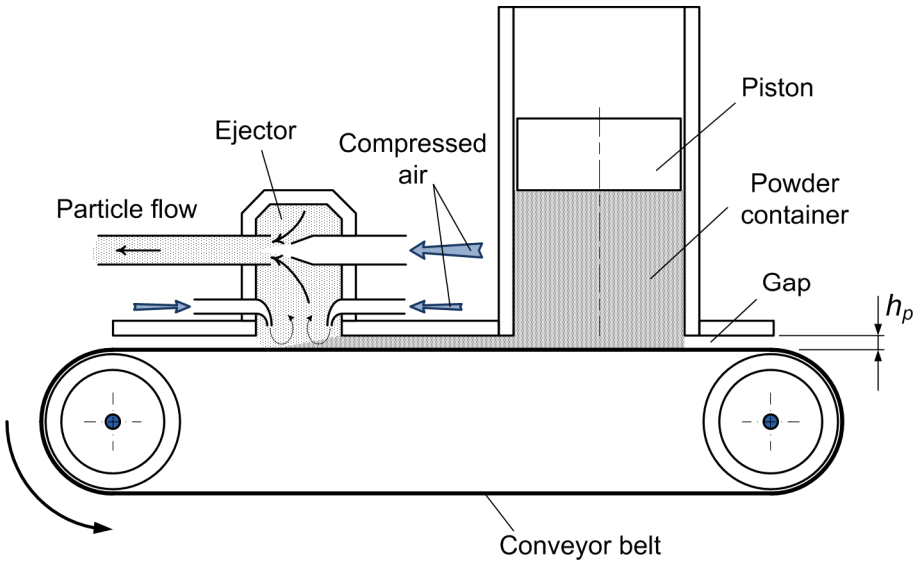

Figure 4.6 Ejecting dispenser configuration

container from which they pass onto a conveyor belt which transports a layer of thickness h_p of the powder into the operating chamber, where particle suspension is generated by means of high-velocity streamlets disposed along the perimeter of the chamber. The suspension obtained is inhausted into an ejector mixing chamber where particles are mixed with induced air. Then the formed high-speed particle stream passes through a pipeline to the air duct of the experimental set-up and is sprayed into the main air stream. Varying the speed of conveyor belt, one can easily control particle consumption which can be defined without taking into account any loss by

$$C = D_c h_p v_c \tag{4.2}$$

where D_c – cylindrical container diameter, h_p – thickness of the particle layer, v_c – conveyor belt velocity.

The main element of the dispenser is the ejector which must provide effective mixing of the gaseous and disperse phases of the particle stream. To provide proper operation of the injector, it is necessary to provide equal consumption of the induced gas (a composition of particles and air) from the ejector operating chamber and inducing gas. For effective fine-dispersed spraying of particles which tend to coagulation, it is necessary to provide a high speed of the streamlets in the operating chamber. In such a way, a strong turbulent stream is formed in the chamber which entrains all particles from the conveyor belt into the ejector mixing chamber.

To calculate the gas consumption of the ejector, the momentum conservation law [43] is used in the form:

$$Q_2 = Q_1 + Q_3 \text{ or } \frac{Q_2}{Q_1} = \xi + 1, \tag{4.3}$$

where Q_1 – consumption of inducing gas (air), Q_3 – consumption of induced gas (particle suspension), Q_2 – total consumption, and $\xi = Q_3/Q_1$ – ejection coefficient. The consumption ratio in the nozzle and the mixing chamber (Figure 4.7) is proportional to the ratio of their diameters [43]:

$$\frac{Q_2}{Q_1} = \frac{d_{n2}}{d_{n1}} \tag{4.4}$$

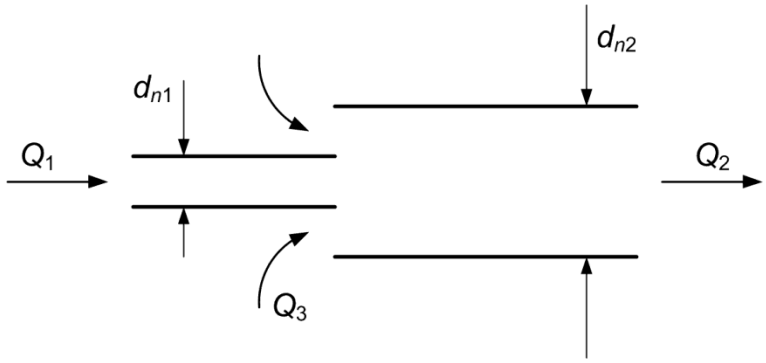

Figure 4.7 Ejector configuration

For effective turbulence generation in the operation chamber, the air streamlets coming out from nozzles must have significant kinetic energy applied by high-enough steam velocity (Figure 4.6), which leads to high values of nozzles flow rate. The pressure in the operation chamber must be sustained at the level of atmospheric pressure so that the consumption of the inducing gas Q_3 is sufficiently high (Figure 4.7).

The ejector construction provides a common supply for the inducing and the induced gas. For guaranteeing stable operation, it is necessary to fulfil the condition of $\xi = 1$. However, because of the impossibility to determine the hydraulic loss in a complicated system of channels and holes, the ejection coefficient must be defined by exceeding the value of the consumption Q_3 ($\xi > 1$) in order to prevent excess pressure in the ejector operation chamber. Moreover, low pressure in the operation chamber promotes additional air inflow providing more effective particle capture from the conveyor belt. In the dispenser designed, the value of the ejecting coefficient is equal to $\xi = 5$ which corresponds to nozzle and mixing chamber diameters of $d_{n1} = 2$ mm, $d_{n1} = 8$ mm. Valves for regulation of the inducing gas and blowing streamlets consumption are provided in the ejector construction, which permits the optimal control for every type of powder.

The outlook of the designed ejecting dispenser is presented in Figure 4.8a, the dispenser built in the experimental set-up is shown in Figure 4.8b. In the construction, the adjustment of the gap h_p (Figure 4.6) depends on the particle size of the powder. Moreover, the variation of the parameter h_p permits to regulate the particle consumption over a large range. A system of rotation speed control of the conveyor engine which is equipped with

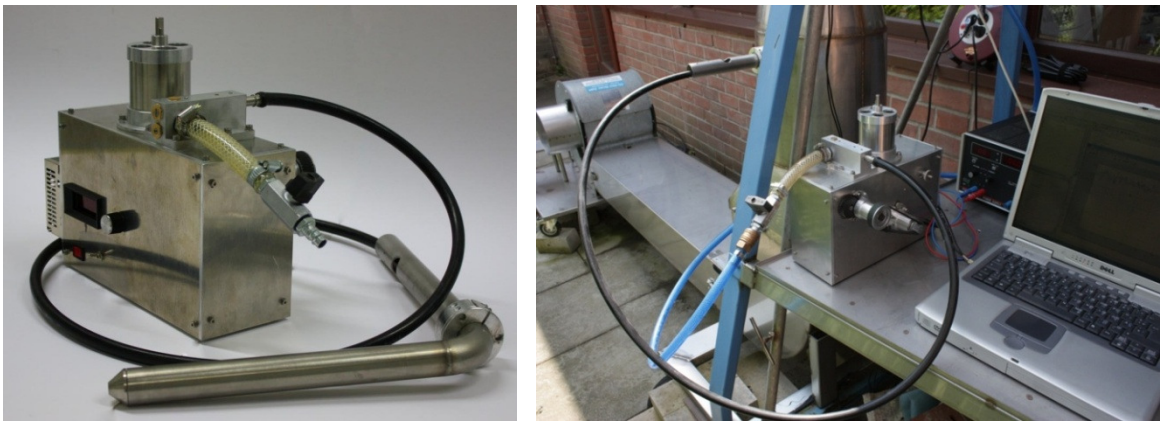

a) b)

Figure 4.8 Outlook of ejecting dispenser

a rotation frequency indicator permits to control the powder consumption manually or automatically by using a computer. In automatic mode, interaction with the PC is realized with RS-232 interface and a D/A converter embedded in the supply control board of the conveyor engine. The software MATLAB is used as control program which permits to automate particle stream parameter measurements.

For a determination of the ejecting dispenser characteristics, an experimental study of the device has been carried out using particles of different size. Some results of dispenser calibration are given in Figure 4.9 where the ordinate corresponds to particle mass

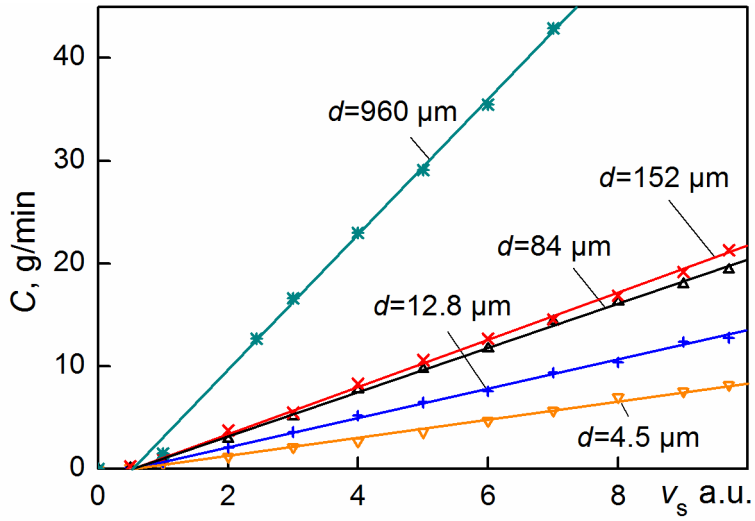

Figure 4.9 Particle consumption vs. particle supply velocity

consumption (gram per minute) and the abscissa represents the velocity of powder supply in arbitrary units. As can be seen, the obtained particle consumption depends practically linearly on this velocity which can be modelled by the expression:

$$C = k_d v_s - V_0, \tag{4.5}$$

where k_d – coefficient of proportionality depending on powder type and gap thickness h_p (Figure 4.6), V_0 – starting voltage of the conveyor engine which is here equal to $V_0 = 0{,}55$ V. The coefficient k_d has been determined experimentally for all particle sizes – Table 4.2

Table 4.2 Consumption parameters of the ejecting dispenser

d , μm	4.5	12.8	84	152	960
h_p , μm	0.12	0.12	0.12	0.2	1.5
k_d	0.9	1.4	2.06	2.26	6.12

4.1.4 Powder materials for the full-scale experiments

Different samples of powders widely applied in the abrasive industry are used for carrying out some modelling experiments, including:

- artificial quartz SiO_2 (~ 84 μm);
- fused alumina Al_2O_3 (4.5 μm, 29.2 μm, 44.5 μm, 152 μm);
- sand (mostly SiO_2 with impurities – 960 μm).

The majority of the used powders are polydisperse, the particle size distribution of which depends on their origin [44 – 47]. The particle size of powders of natural origin is usually distributed log-normally [44] (2.22). For powders of artificial origin which are generated in technological processes (fused of solid material, crashing into small pieces etc.), a two-parameter Weibull distribution is more typical. Their cumulative distribution function is given by [45]:

$$F_X(d) = 1 - e^{-\left(\frac{d}{\gamma}\right)^{\chi}} \tag{4.6}$$

where d – particle diameter, $\chi > 0$, $\gamma > 0$ – shape and scale distribution parameters, respectively. The corresponding probability density function can be represented by:

$$f_X(d) = \frac{\chi}{\gamma}\left(\frac{d}{\gamma}\right)^{(\chi-1)} \cdot e^{-\left(\frac{d}{\gamma}\right)^{\chi}}. \tag{4.7}$$

During crashing of the powder material, a quite wide particle size distribution is usually obtained. Therefore crashed powders are divided into several fractions with quite narrow distribution. The way of separation depends on particle size [46]: particles of less than 50 μm in size are separated using the sedimentation method, and for rough fractions the sieving method is applied with two sieves. It is significant that the fractions obtained by the sedimentation process also obey the Weibull distribution law [47], but for sieved powders the distribution law depends on fraction size Δd (Figure 4.10). Moreover, the narrower the

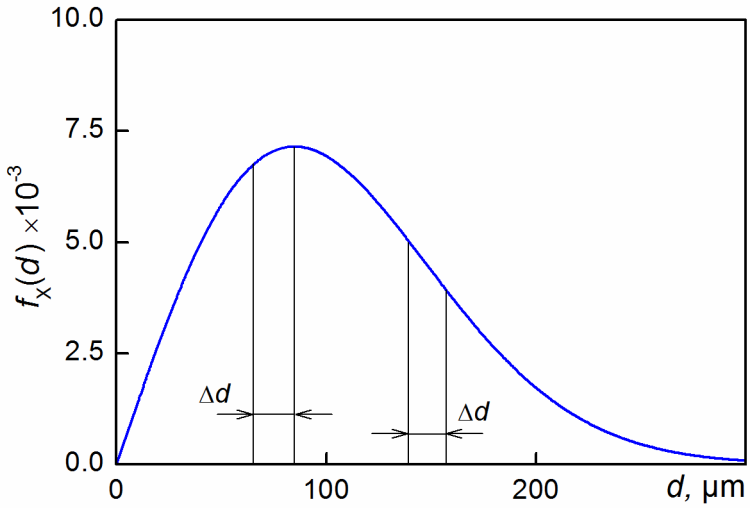

Figure 4.10 Particle ensemble separation into fractions

fraction size and the wider the initial distribution, the more uniformly are the sizes of particles distributed inside the fraction, so that as first approximation such distribution can be considered as uniform. As an example, Figure 4.11 shows a uniform particle size distribution of a powder under test which was obtained by the sieving method, the lower bound of particles being $d_{\min} = 63$ μm and the upper bound – $d_{\max} = 106$ μm.

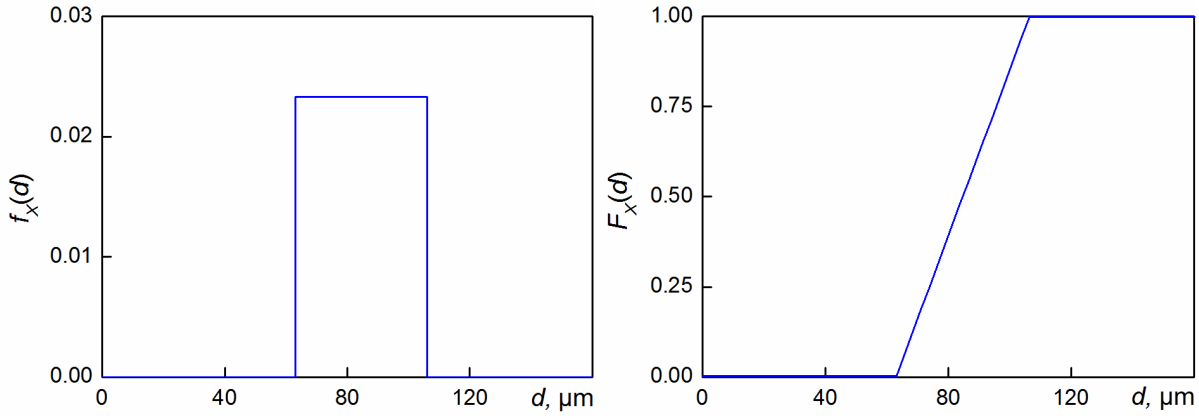

a) b)

Figure 4.11 Uniform particle size distribution of sieved fraction: probability density function – a), cumulative distribution function – b)

As mentioned above, all powders can be classified into two big groups according to the way of separation: 1) powders obtained by the sedimentation method; 2) sieved powders. The sedimentary powders are characterized by 3rd, 50th, and 94th quantile, according to FEPA (Federation of European Producers of Abrasives) standards – d_S3-Factor, d_S50-Factor, d_S94-Factor.

The data of powder producers (e.g. Kuhmichel Abrasiv GmbH) have been approximated by the cumulative Weibull distribution (4.6) – Figure 4.12a (smooth curves, the

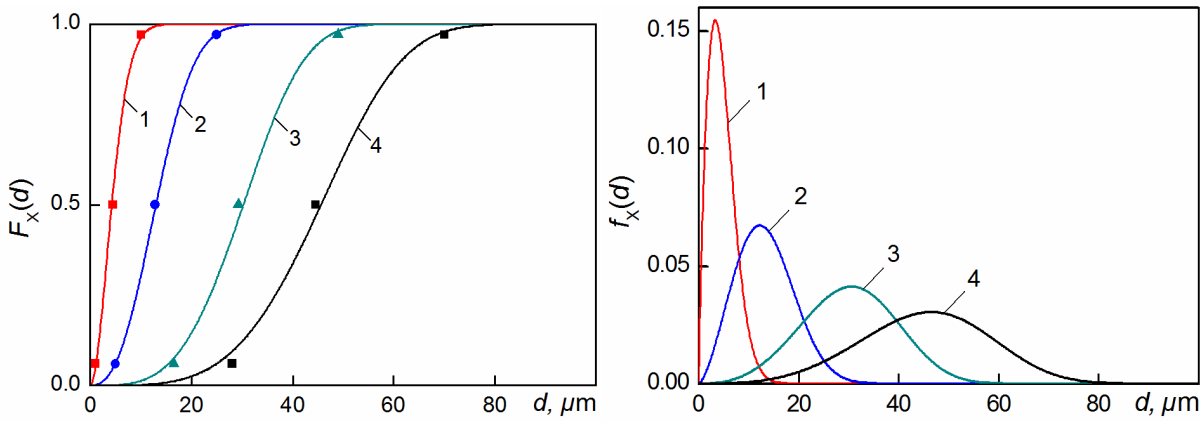

a) b)

Figure 4.12 Particle size distribution for the powders under test according to Table 4.3: cumulative distribution function – a), probability density function – b)

number of which correspond to Table 4.3, the asterisks correspond to the quantiles outlined in the producer specification) and the parameters of the distribution γ and χ have been determined (see Table 4.3). This permits to calculate the density function (Figure 4.12b) for all powders obtained by the sedimentary process.

Table 4.3 Parameters of sedimentary powders

Curve in Figure 4.12a	FEPA	Powder parameters			Weibull distribution parameters			
		d_S94-Factor, μm	d_S50-Factor, μm	d_S3-Factor, μm	γ	χ	d_{mode}, μm	d_{mean}, μm
1	F1000	1.0	4.5 ± 0.8	10.0	5.2	1.8	3.31	4.62
2	F500	5.0	12.8 ± 1.0	25.0	15	2.5	12.23	13.31
3	F320	16.5	29.2 ± 1.5	49.0	33.5	3.6	30.6	30.18
4	F240	28.0	44.5 ± 3.0	70.0	50	4	46.53	45.32

Results of the analysis done for powders with bigger particle size, which have been obtained by the sieving method, showed that the particle size distribution is close to a uniform one – Table 4.4. Parameters $d_{\max}$ and $d_{\min}$ correspond to the mesh size for passing and no-passing sieves.

Table 4.4 Parameters of sieved powders

N	FEPA	d_{min}, μm	d_{mean}, μm	d_{max}, μm
5	F150	63	84	106
6	F090	125	152	180

Besides these parameters, producers also often outline in their powder specification the so-called Stokes diameter [48] or the root-mean-cube diameter which is equal to the diameter of an equivalent sphere, the volume of which is equal to the volume of the particle

under test: $d = \sqrt[3]{\frac{6}{\pi} V_p}$. In reality, however, the powder particles show the shape of complex polygons with sharp edges as can be seen from Figure 4.13. Nevertheless, to simplify the calculation of electromagnetic scattering it is assumed here that they are of spherical shape.

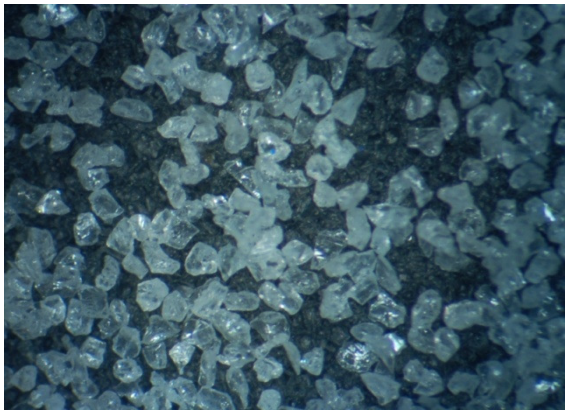

Figure 4.13 Outlook of the fused alumina (Al_2O_3) grain F080

The calibrated particles have also been prepared from sea sand by using the sieving method with two specially made sieves (Figure 4.14) with mesh sizes $d_{\min}$ = 1.0 mm and $d_{\max}$ = 1.3 mm. As has been found (Figure 4.15), sea-sand particles are also far from showing spherical shape.

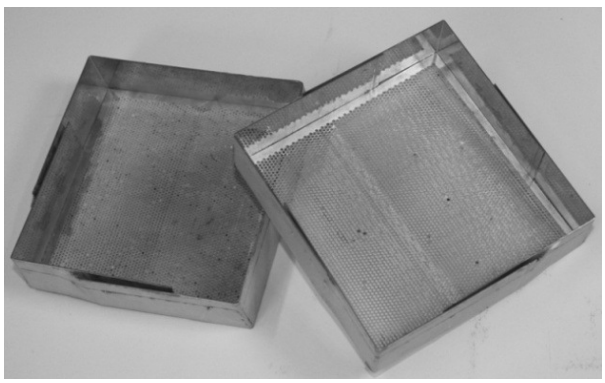

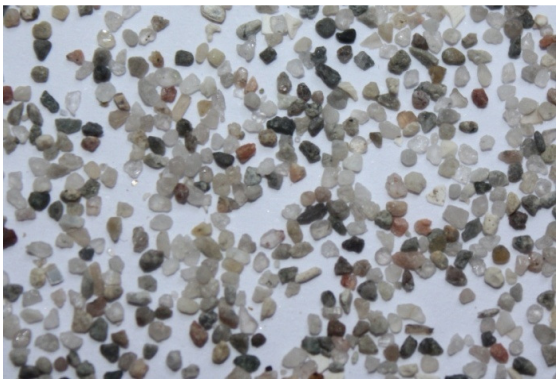

a) b)

Figure 4.14 Sieves used for sand fraction separation – a), sand particles – b)

That is why the root-mean-cube particle diameter has been estimated to represent the volume of a liquid V_l displaced by N sand particles $\bar{d}_3 = \sqrt[3]{\frac{6}{\pi} \overline{V_p}}$, where $\bar{V}_p = \frac{V_l}{N}$ (in the case under consideration: N = 2100). So the root-mean-cube particle diameter is here equal to $d_3 = 0.96$ mm which slightly differs from the minimum mesh diameter of the no-passing sieve of $d_1 = 1$ mm . Moreover, weighting the particle set permits to estimate the material density: $\rho_p = 2.65$ g/cm^3 in our example, which corresponds to quartz, granite, and shell rock

($\rho_p = 2.4 - 2.8$ g/cm^3). Thus the measurement carried out permits to determine the root-mean-cube diameter which is used in the calculation of the RCS for double-frequency sounding (Chapter 2).

The dielectric parameters of the powder particles used are also needed for such calculations. As has been found, all used materials have quite high value of permittivity and provide low dielectric losses (Table 4.5), which makes them suitable for radar sounding in mm wave band.

Table 4.5 Physical properties of the materials under test

Material	ρ_p, kg/m^3	ε'	ε''
Corundum (Al_2O_3)	3900	9.8	0.001
Quartz (SiO_2)	2600	4	0.0001
Sea-sand	2650	3.75	0.001

4.2 Comparison of remote sensing by a mono-frequency radar-sensor and by contact measurements

The particle mass loading (g/m^3) is one of the most important characteristics of a disperse stream which is widely used for the description of the dustiness of air and for the intensity of industrial emissions. In the last case, which is the most interesting one for environmental monitoring, the disperse stream parameters can be measured by contact methods. Particularly by using sampling, one can obtain a sufficient quantity of particles and measure the particle size distribution by contact. However, it is not possible to estimate the mass loading of industrial emissions in some distance from the emission source (funnel etc.) using contact measurements. Therefore, the method proposed in paper [16] for remote measurement of the mass loading in disperse streams by using a radar-sensor (section 2.2) is of apparent interest.

In this connection, an experimental study of the proposed remote sounding method has been carried out with the help of the developed radar sensor (section 3.1) and the experimental set-up (section 4.1).

4.2.1 Algorithm of data processing

As mentioned above (section 2.1), the specific value of the RCS of a volume scatterer can be expressed by

$$\sigma_0 = \frac{P_r}{P_t} \frac{(4\pi)^3}{G_{0T} G_{0R} \lambda^2 \cdot V_{ef}}, \quad \left(\frac{1}{\mathrm{m}}\right) \tag{4.8}$$

where P_t – transmitter power, P_r – power received, $G_{0T,0R}$ – transmitting and receiving antenna gain, respectively, λ – operating wavelength, and V_{ef} – effective value of scattering volume. On the other hand, in an approximation of Rayleigh scattering, the specific RCS is given by [16]

$$\sigma_0 = \frac{\pi^5}{\lambda^4} |K|^2 \cdot N_T \cdot \sum_i d_i^6 f_X(d_i), \tag{4.9}$$

$$|K|^2 = \frac{(\varepsilon' - 1)^2 + \varepsilon''^2}{(\varepsilon' + 2)^2 + \varepsilon''^2},$$

where N_T – total number of particles in unit volume, d_i – diameter of i^{th} particle, $f_X(d_i)$ – probability density function for particle size.

The mass loading of the disperse stream (g/m^3) can also be expressed in terms of the probability density function in the following form:

$$M = \frac{\pi}{6} \rho_p \cdot N_T \sum_i d_i^3 \cdot f_X(d_i) \tag{4.10}$$

where ρ_p – particle material density ($\mathrm{g/m^3}$). Combining expressions (4.8 – 4.10), one can obtain an important relation:

$$\sigma_0 = B(d) \cdot M \ , \qquad B(d) = \frac{\pi^4 |K|^2}{\lambda^4 \rho_p} \cdot \frac{\sum_i d_i^6 f_X(d_i)}{\sum_i d_i^3 f_X(d_i)}, \tag{4.11}$$

in which the coefficient $B(d)$ depends only on particle size and operating wavelength. The physical interpretation of the coefficient $B(d)$ becomes understandable for a monodisperse stream ($d_i \equiv d$) when $B(d) \cong d^3$, and for other distributions $B(d) \cong d^q$, where $q < 3$. This leads to the following relation: $\sigma_0 = \alpha \cdot M^\beta$ (in the case under consideration $\beta = 1$), which is widely used in radio-meteorology in $Z = AI^B$ (the reflectivity-intensity relation) [15].

During our experimental study, the developed equipment in W-band has been used (sections 3.1 and 3.2), and the measurements have been carried out for mean values of the powder diameter being equal to $\bar{d} = 29.2$ μm, 44.5 μm, and 152 μm.

The contact measurements of mass loading use the powder consumption C in g/min according to:

$$M = \frac{1}{60}\frac{C}{S_D \times v}\ , \tag{4.12}$$

where S_D – duct cross section in m^2, v – stream velocity which is measured by the Doppler frequency shift $v = \frac{\lambda}{2} f_D$.

4.2.2 Calibration of the mono-frequency radar-sensor

To use expression (4.11) for measuring the mass loading, the specific RCS of the disperse stream must be determined. For this to do, a calibration of the radar has been performed using an etalon reflector in the form of a metallic sphere. Comparing the radar equation for a point target (metallic sphere) (2.1) with that for a volume scatterer in the bistatic case (2.8), it is easy to show that the specific RCS of the disperse stream σ_0 is determined as:

$$\sigma_0 = \frac{P_{DS}}{P_{et}} \cdot \frac{L_c}{V_{ef} R_{et}^4} \cdot \sigma_{et}\,, \tag{4.13}$$

where P_{DS} – power reflected from a disperse stream, P_{et} – power reflected from the etalon reflector, V_{ef} – effective scattering volume of the disperse stream (2.14), R_{et} – distance from radar to the etalon reflector, σ_{et} – RCS of the etalon reflector (for a sphere $\sigma_{et} = \pi\left(\frac{D_{et}}{2}\right)^2$, where D_{et} – diameter of the sphere), L_c – coefficient of losses due to an additional signal attenuation when the etalon reflector is outside the effective scattering volume V_{ef}, which leads to a decreased effective RCS of the etalon reflector. As the estimations show, the value of the additional losses $L_c = \left[\frac{G(\theta_{et})}{G(0)}\right]^2$ dB and the rest of the components in (4.13) may be measured.

To calibrate the scale of the receiver meter, an experimental set-up is used (Figure 4.15) which contains a radar-sensor and a small metallic sphere pendulum on a nylon cord to utilize the Doppler selection of the reflected signals.

The spectrum of the signal reflected from the calibrating sphere with diameter D_{et} = 49.95 mm at a distance of R_{et} = 5.2 m is shown in Figure 4.16. The spectrum shows almost rectangular shape corresponding to the Doppler frequency shift of the moving sphere $f_D \le \frac{2v_{\max}}{\lambda}$, where $v_{\max}$ – maximal velocity of the calibrating sphere.

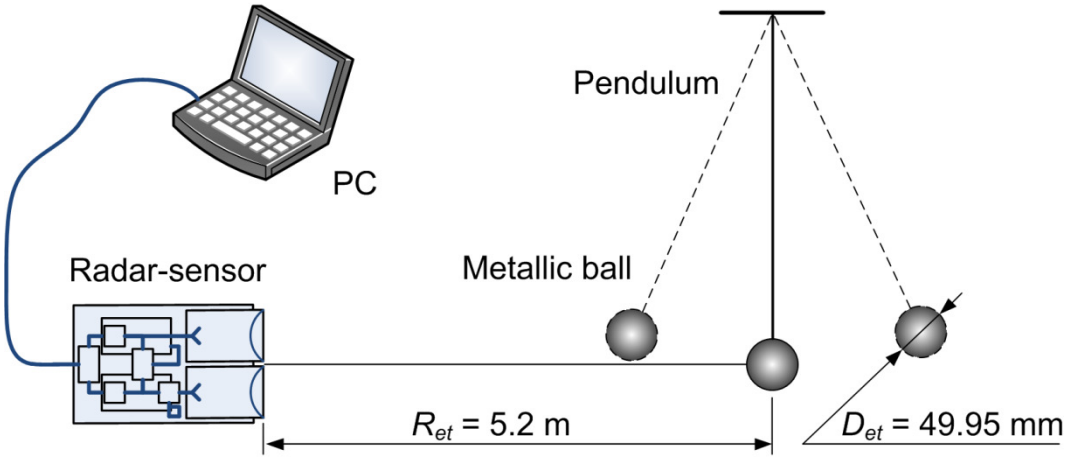

Figure 4.15 Configuration of the radar-sensor calibration

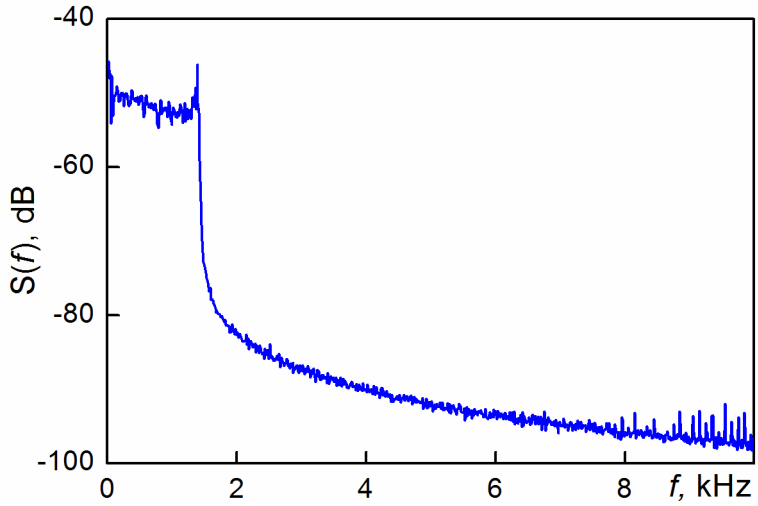

Figure 4.16 Spectrum of signal reflected from a calibrating sphere

The software for signal processing used has logarithmic scale and permits to directly measure the ratio of power reflected from the disperse stream and from the etalon reflector for further data processing.

4.2.3 Results of experimental study

In Figure 4.17a, the typical spectra of a signal reflected from several disperse streams (particle mean diameter $\bar{d} = 29.2$ μm, 44.5 μm, and 152 μm) are presented. As can be seen, the mean value of the Doppler frequency (mean stream velocity) just insignificantly depends on the mean particle diameter, which was taken into account for particle mass loading calculations.

In Figure 4.17b, an example of the radar sensitivity calibration [49] is shown, where the black curve corresponds to the receiver noise, red curve – to a signal reflected from a

disperse stream with particles of 5 μm in size, and blue curve – to signal from noise generator with spectral noise density of 12 dB/kT ($k = 4 \cdot 10^{-21}$ W/HzK° – Boltzmann constant).

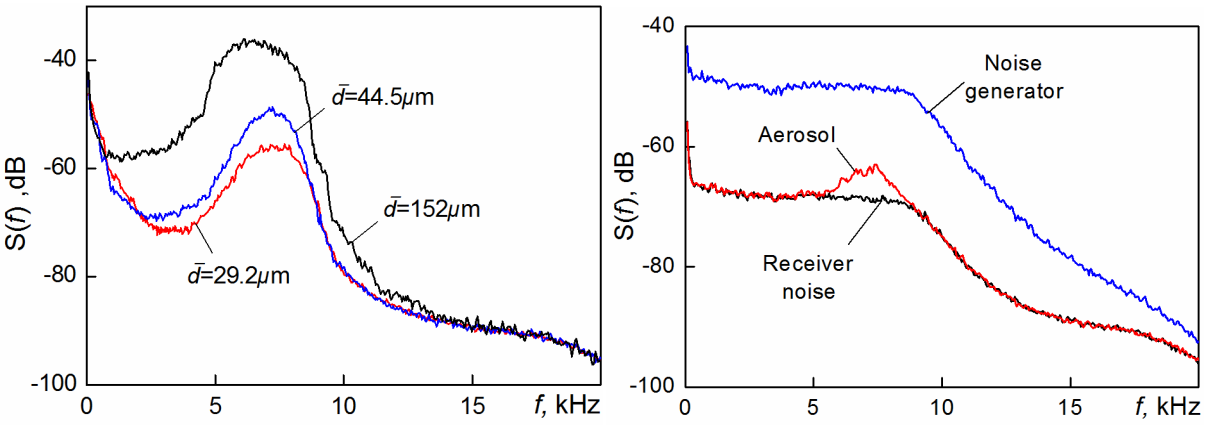

a) b)

Figure 4.17 Spectra of signals reflected from disperse streams

The calibration performed in section 4.2.2 permits to carry out absolute measurements for the RCS of the disperse stream depending on the particle mass loading M (g/m^3) according to (4.11) – Figure 4.18. As can be seen, the data obtained confirm the linear character of the dependence, which is predicted by expression (4.11) over wide ranges of the mass loading values. This is an important result for the measurement of disperse stream parameters.

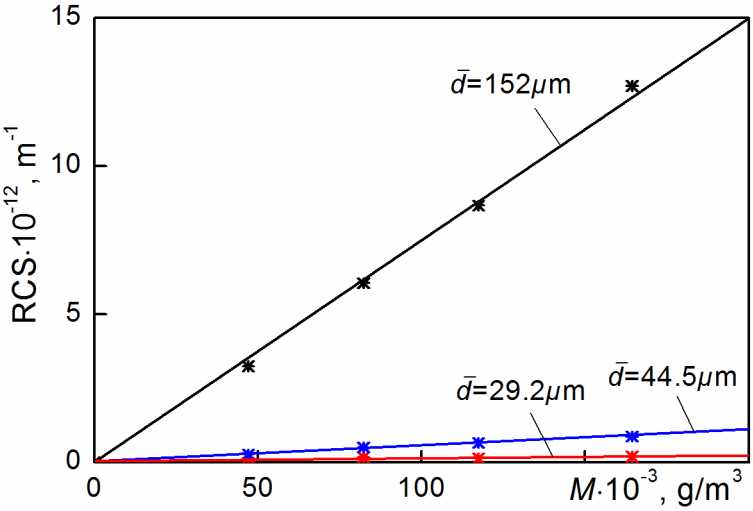

Figure 4.18 RCS dependence on particle mass loading

The conducted measurement permits to approximate the dependence of the coefficient $B(d)$ in (4.11) on the particle diameter in the form of $B(d) = 1.4 \cdot 10^{-15} \cdot \bar{d}^{2.1}$ which is depicted in Figure 4.19 (smooth curve). It is interesting to compare this dependence with the analogous one for a monodisperse medium which corresponds to a cubic dependence $\bar{d}^3$ (dashed curve in Figure 4.19). This confirms the preceding conclusion concerning the inequality $q < 3$ in

expression $B(d) \cong d^q$ (section 4.2.1) and the decrease of the rate of increase of coefficient $B(d)$ for a polydisperse stream.

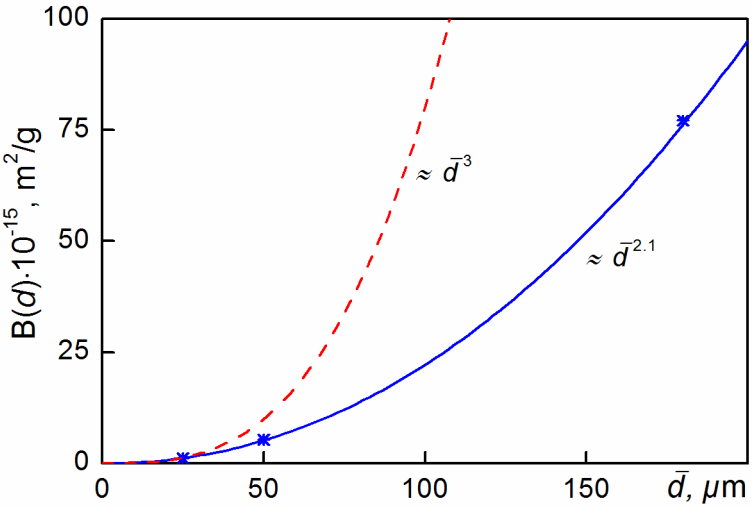

Figure 4.19 Dependence of coefficient $B(d)$ in (4.11) on mean particle size

Furthermore, a comparison of the experimental data from remote sensing and contact measurements has been performed for a monodisperse stream of solid particles of different concentration and mass loading. The experimental set-up developed in the previous part (Figure 4.1, 4.2) has been used for measurements on corundum and quartz powders, the characteristics of which are shown in Tables 4.3 – 4.5.

The signal processing is performed in accordance with expressions (2.18, 2.19) and results of the set-up calibration were used. Measurements were performed for powders with mean particle diameter $\overline{d}$ = 29.2 μm, 44.5 μm, 84μm, and 152 μm, the powder consumption Q in g/min was registrated, which permits to calculate mass loading (4.12) and particle concentration (2.20).

The comparison data from contact measurements and remote sensing by a mono-frequency bistatic radar-sensor are shown in Figure 4.20. As one can see, the data of remote sensing for powders with particles $\overline{d}$ = 29.2 μm and $\overline{d}$ = 44.5 μm are in a quite good agreement with the data of the contact measurements. The measurement error of mass loading and particle concentration does not exceed 23% over the whole range of the disperse stream parameter variation.

On the other hand, a comparison of measurement data for powders with larger particle dimentions $\overline{d}$ = 84 μm and $\overline{d}$ = 152 μm shows rising of the error to up to 70%. This is a consequence of an enlarged diffraction parameter $\rho = \frac{2\pi r}{\lambda}\sqrt{|\dot{\varepsilon}|}$ which does not permit to use expressions (4.9) for Rayleigh scattering (Figure 2.8), which had, however, been used to obtain the main expressions for the calculation (2.20, 4.10, 4.11).

It is interesting to note, that the results obtained confirm the conclusion that the RCS of particles of arbitrary shape may be considered as being the RCS of particles of spherical shape, if their dimensions are essentially smaller than the wavelength. Futhermore, the use of

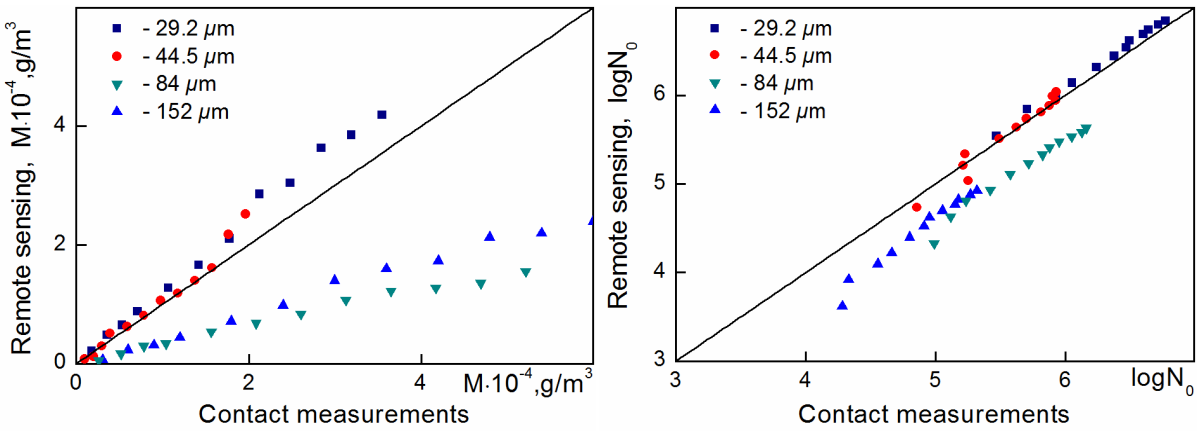

Figure 4.20 Data comparison of remote sensing by a mono-frequency radar-sensor (Ver. axis) and by contact measurements (Hor. axis): mass loading – a), particle concentration – b)

expressions (2.20, 4.10, 4.11) is only possible for the Rayleigh scattering regime, otherwise the rigorous expressions must be used [27]. So the main conclusion is that the mono-frequency method of remote sensing permits to measure mass loading and particle concentration of disperse streams in the case of a known particle distribution law and under the condition of Rayleigh scattering.

4.3 Comparison of remote sensing by a double-frequency radar-sensor and by contact measurements

In practice, the particle distribution law is often unknown, so that the method described above (section 2.3) is of great interest. The method can provide remote sensing of disperse streams with unknown particle distribution law and is based on the use of a double-frequency radar-sensor.

A number of traditional assumptions for electromagnetic scattering had been made to obtain the main relations (section 2.3) on which the signal processing algorithm is based. The estimation of the validity of such assumptions is of great interest. It can be performed by an experimental study using a double-frequency sensor (section 3.3) and the developed experimental set-up (section 4.1).

The main approach is based on the remote sensing of a disperse stream model which is controlled by the contact method. Therefore, the model of a monodisperse stream is used in the form of a sea-sand particle ensemble which is calibrated by means of sieving (section 4.1).

The size of the particles and the wavelengths of the double-frequency radar are chosen to satisfy the conditions for non-Rayleigh scattering that have been formulated in Chapter 2.

4.3.1 Algorithm of data processing

As has been shown in section 2.3, the measurement of mass loading $M\,(\mathrm{g/m^3})$ and particle concentration may be performed under a condition $r_{\min} \le r \le r_{\max}$, where the upper boundary is defined as:

$$r_{\max} \le 0{,}44\frac{\lambda_{\min}}{\left|\sqrt{\dot{\varepsilon}}\right|}, \qquad \mathrm{Re}\,\dot{\varepsilon} \ge 5 \tag{4.14}$$

and the lower boundary $r_{\min}$ depends on the measurement accuracy of the specific RCS of the disperse stream $\Delta\sigma_{\min}$. It is represented as a root of a transcendental inequation:

$$40\lg\frac{\lambda_{\max}}{\lambda_{\min}} - \sigma_D\left(r_{\min}\right) \ge \Delta\sigma_{\min}, \tag{4.15}$$

where the first component represents the asymptotic value of the differential RCS (DRCS) for small values of the particle radius: $\lim\sigma_D(r) = \left(\frac{\lambda_{\max}}{\lambda_{\min}}\right)^4$ for $r \to 0$; σ_D and $\Delta\sigma_{\min}$ are expressed in dB. In the case under consideration, $\lambda_{\min} = 3.23$ mm, $\lambda_{\max} = 8.16$ mm, and $\mathrm{Re}\,\dot{\varepsilon} = 3.75$. The measurement accuracy of the differential RCS rate is estimated as $\Delta\sigma_{\min} = 1\,\mathrm{dB}$ which gives $r_{\min} = 0.413\,\mathrm{mm}$ and $r_{\max} = 0.72\,\mathrm{mm}$. So the root-mean-cube diameter of the sea-sand particles $\mathrm{d}_3 = 0.96$ mm satisfies the mentioned condition $r_{\min} \le r_3 \le r_{\max}$.

As a result, the effective value of the particle radius is determined by a numerical solution of the transcendental equation [25]:

$$\sigma_D^{eq}\left(\rho_{rmc}^{ef}\right) = \sigma_D^X, \tag{4.16}$$

where $\sigma_D^{eq}(r)$ – DRCS of an equivalent medium which must be calculated for the dielectric parameters of the used sea-sand particles, σ_D^X – measured value of DRCS, ρ_{rmc}^{ef} – effective value of diffraction parameter $\rho_{rmc}^{ef} = \frac{2\pi}{\lambda_{\min}\sqrt{\left|\dot{\varepsilon}\right|}} \cdot r_{rmc}^{ef}$, r_{rmc}^{ef} – effective root-mean-cube radius.

In Figure 2.9, the graphical solution of equation (4.16) has been depicted to find the effective root-mean-cube radius r_{rmc}^{ef} using the measured value of the DRCS σ_D^X. Then it is

possible to calculate the effective values of the disperse stream parameters, including an effective particle concentration N_T^{ef} (1/m) and an effective mass loading [12, 17] M^{ef} (g/m^3):

$$\begin{cases} N_T^{ef} = \dfrac{\sigma_0^x(\lambda_{\min})}{\sigma_p\left(\rho_{rmc}^{ef}\right)}; \\ M^{ef} = N_T^{ef} \cdot \dfrac{4}{3}\pi\left(r_{rmc}^{ef}\right)^3 \rho_p, \end{cases} \tag{4.17}$$

where $\sigma_0^x(\lambda_{\min})$ – the specific RCS value measured at the minimum wavelength $\lambda_{\min}$, $\sigma_p\left(r_{rmc}^{ef}\right)$ – the RCS of particle with radius r_{rmc}^{ef}, ρ_p – density of particle material (g/m^3).

At the output of each frequency channel, the value of the power spectrum density (PSD) must be averaged over a set of time intervals which corresponds to the Fast Fourier Transform (FFT) size $M = Int\left[\dfrac{T_0}{T_S}\right]$, T_0 – realization time of signal reflected, T_S – time of interval that corresponds to FFT size:

$$\left\langle S(\Omega)\right\rangle = \frac{S_0}{M}\sum_{m=1}^{M} S_m(\Omega), \tag{4.18}$$

where S_0 – maximum of spectrum which depends on the power budget of the radar-sensor, $S_m(\Omega)$ – squared modulus of FFT at m^{th} interval $m \in (1, M)$, which is calculated in a MATLAB environment.

In Figure 4.21, an example of the reflected signal has been plotted in time domain at wavelengths $\lambda_{\min} = 3.23$ mm – Figure 4.21a and $\lambda_{\max} = 8.16$ mm – Figure 4.21b. These measurements have been carried through for three different values of the particle stream

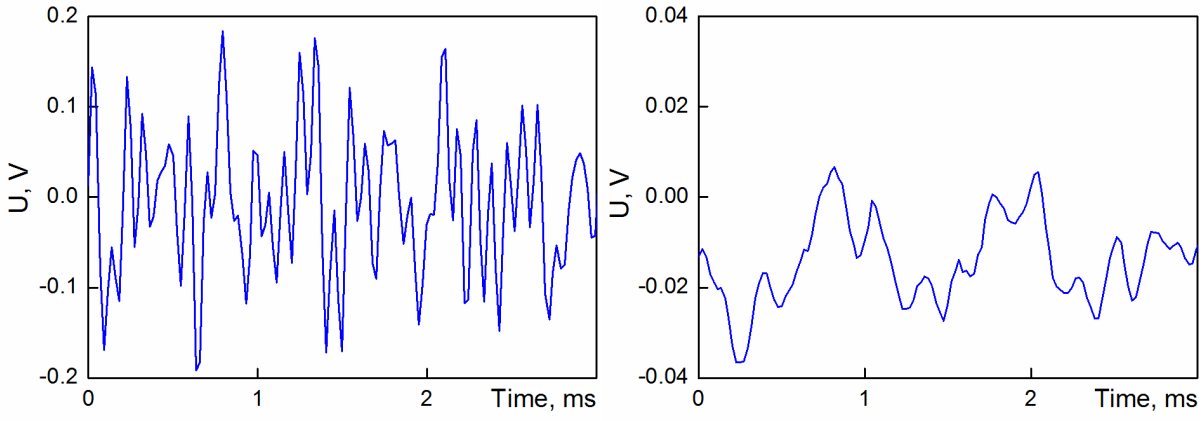

a) b)

Figure 4.21 Signal reflected in time domain:
a) $\lambda_{\min} = 3.23$ mm; b) $\lambda_{\max} = 8.16$ mm

consumption $C_1 = 12.7$ g/min; $C_2 = 23$ g/min; and $C_3 = 35.5$ g/min which correspond to a mass loading of $M_1 = 0.3$ g/m^3; $M_2 = 0.54$ g/m^3; and $M_3 = 0.84$ g/m^3. These figures confirm the noise-like structure of the signals reflected from a particle ensemble in a turbulent disperse stream and thus justify the procedure of statistical signal processing (4.18).

Figure 4.22 shows the PSD which corresponds to the signal measured at wavelengths $\lambda = 3.23$ mm – Figure 4.22a and $\lambda = 8.16$ mm – Figure 4.22b, respectively. It is necessary to note that the width of the obtained PSD confirms the turbulent nature of the air stream in the duct. Therefore, it is necessary to integrate the measured value of the PSD in order to calculate the specific RCS (4.13):

$$P_{DS} = \int_0^{\Omega_{max}} d\Omega \left\langle S(\Omega) \right\rangle, \tag{4.19}$$

where Ω_{max} – passband of the Doppler filter at the output of the IF mixer (Figure 3.47).

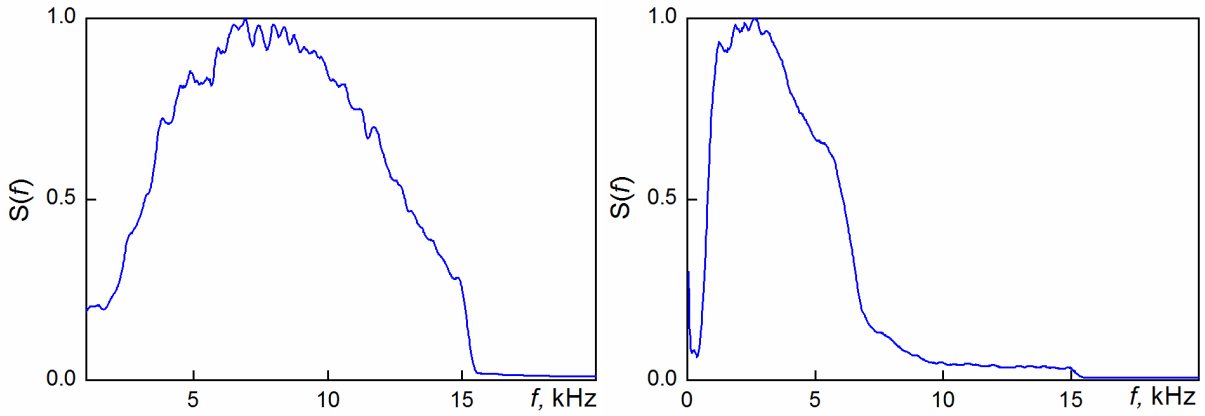

a) b)

Figure 4.22 Spectrum of signal reflected:
a) $\lambda_{min} = 3.23$ mm; b) $\lambda_{max} = 8.16$ mm

The constant S_0 in (4.18) is calculated from the calibration of the sensitivity of the radar receiver by using the noise generator NG (Figure 3.1). The radiated power P_T as well as the antenna gain $G_{0R} = G_{0T}$ were measured during the test. To use expression (4.13) for calculation of the RCS of the disperse stream, it is necessary to define the effective value of the scattering volume (2.14) for which the distance to the antenna beam interception point (Figure 3.55) must be taken into account. (In the case under consideration, $z_0 = 2.005$ m for the W-band frequency channel and $z_0 = 1.575$ m for the K_a-band frequency channel, respectively.)

4.3.2 Results of the experimental study

To check the algorithm proposed for measurement of mass loading and particle concentration of disperse streams, a full-scale experiment has been performed using the experimental set-up described in section 4.1 and the double-frequency radar-sensor (section 3.3). The calibrated sea-sand particles were also used to measure the DRCS of the disperse medium at three modes of the dispenser which differ by their particle consumption leading to different mass loading and particle concentration.

As a result of the experimental study, some data obtained are presented in Table 4.6 (remote sensing data – red text) for the DRCS, effective root-mean-cube radius, mass loading, and concentration of particles [50 – 52]. As one can see, the experimental data are characterized by good reproducibility (coefficient of variation ≤ 1%) in spite of a significantly differing particle flow consumption $\frac{C_{\max}}{C_{\min}} \cong 3$. On the other hand, the particle diameter and the mass loading obtained by remote sensing slightly exceed the corresponding data of contact measurements within a range of 10%, while the particle concentration from remote sensing stays below the value of the contact data by about 25%.

Table 4.6 Comparison of remote and contact measurements

Parameter	Consumption 12.7, g/min		Consumption 23.0, g/min		Consumption 35.5, g/min	
	Remote	Contact	Remote	Contact	Remote	Contact
Differential RCS, dB	13.4	14.96	13.48	14.96	13.48	14.96
Effective value of RMC radius, mm	0.55	0.48	0.547	0.48	0.547	0.48
Mass loading, g/m^3	0.344	0.3	0.562	0.54	0.875	0.84
Particle concentration, m^{-3}	186	245	309	440	482	685

Thus the performed experimental study of the double-frequency method of remote sensing confirms both validity and efficiency of the proposed method of disperse stream sensing with preliminary unknown particle size distribution law.

4.4 Conclusions to Chapter 4

As a result of the work performed in Chapter 4, the following conclusions can be drawn:

1. An experimental set-up for study of the characteristics of the signals reflected from disperse streams of solid particles has been developed on the base of a construction which had been produced by DURAG GROUP company. The configuration of the set-up includes a fan, a dispenser of particles, and an air duct in which the radar-sensor is mounted.

2. A screw dispenser for dosing of solid particles, which had been produced by DURAG GROUP, has been tested and calibrated. This permits to control the particle consumption in the experimental study of electromagnetic scattering of disperse streams. It has been shown that such type of dispenser does not permit to form a homogeneous stream with particle dimensions less than 20 μm because of their coagulation.

3. A new dispenser based on the ejection principle has been designed and studied. The developed dispenser provides spraying of particles at least from 5 μm up to 1 mm in size. Calibration data have been obtained to perform an experimental study of radar sensing of disperse streams.

4. The abrasive powders produced in industry have been studied. It was shown that the particle size distribution obeys the Weibull law, which is necessary for a calculation of the electromagnetic scattering characteristics from disperse streams. A calibrated sea-sand powder was produced by sieving in order to confirm the validity of the proposed double-frequency method.

5. The procedure of power budget radar-sensor calibration has been proposed and worked out, which permits to measure the absolute value of the radar cross-section of the studied disperse streams.

6. A comparison of the data obtained from a mono-frequency radar-sensor and from contact methods has been performed. It has been shown that the RCS of particles of arbitrary shape may be considered as resulting from particles of spherical shape, if their dimensions are essentially smaller than the wavelength. Furthermore, the use of the proposed method of mono-frequency sensing is possible only for the Rayleigh scattering regime. Hence the mono-frequency method of remote sensing permits to measure mass loading and particle concentration of disperse streams in the case of known particle distribution law and under the condition of Rayleigh scattering.

7. A comparison of the data obtained from a double-frequency radar-sensor and from contact methods has been performed. It is shown that the effective root-mean-cube radius, mass loading, and concentration of particles are in satisfactory agreement with

contact data. The experimental data are characterized by good reproducibility (the coefficient of variation being ≤ 1%) over a wide range of particle flow consumption. The particle diameter and the mass loading obtained by remote sensing slightly exceed the data of contact measurements (≤ 10%), while the particle concentration from remote sensing differs from corresponding contact data more essentially (≤ 25%).

8. The performed experimental study of the double-frequency method confirms both validity and efficiency of the proposed method for remote sensing of disperse streams with preliminary unknown particle size distribution law.

Summary

The main results of the present work may be formulated as follows:

1. The development of remote sensing methods for solving the inverse problem of reconstruction of the disperse stream parameters is of great scientific interest and practical significance;

2. A bistatic configuration of the radar-sensor for remote sensing of disperse streams is proposed and studied. Such configuration permits to obtain high spatial resolution owing to the transmitting and receiving antenna beam interception and high isolation between transmitting and receiving channels, which allows using a CW mode of signal radiation. For this case, the radar equation for volume scatterers is obtained, which permits to measure the specific RCS of disperse streams of solid particles;

3. An expression for the scattering volume in the case of Gaussian transmitting and receiving antenna beams is obtained. As a result of the analysis, relations for spatial resolution are obtained which permit to optimize the geometry of the bistatic radar-sensor and to propose a mono-frequency method for measuring the characteristics of polydisperse streams. It is shown that disperse stream parameters (mass loading and particle concentration) can be measured by this method, if the particle size distribution law is known, or if its width is quite "narrow": $\Delta r / r_{\text{mod}} \le 0.3$;

4. A double-frequency method for measuring the characteristics of polydisperse streams is proposed and limits of its applicability are defined. It is shown, that this method permits to measure the parameters of disperse streams (mass loading and particle concentration) for both arbitrary but "narrow" particle size distribution $\Delta r / r_{\text{mod}} \le 0.3$ and "wide" particle size distribution $\Delta r / r_{\text{mod}} \ge 4$. The method allows estimating the effective value of the particle size, the particle concentration, and the mass loading. Application limits of the method are defined taking into account unambiguity and attainable accuracy of radar measurements;

5. A bistatic mono-frequency radar-sensor in W-band is developed, constructed, and studied. To provide coherent signal processing, the principle of a drifting intermediate frequency is used. For calibrating the receiver sensitivity, a built-in device is used which is based on a high-stability solid-state noise generator. A horn-lens antenna provides forming Gaussian beams down to the -20 dB level, the isolation between the

receiver and the transmitter is higher than 60 dB, and the receiver noise-figure is ≤ 10 dB. The transmitter includes a high-stability IMPATT generator and a power combiner (for 4 IMPATT diodes), which provides an output power of about 100 mW;

6. A correlation method for signal processing of the noise-like signals from the disperse streams is proposed and studied. The method is based on the distinction of the fine structure of the correlation functions for the reflected signal and thermal noise. It is shown that using broad bandwidth of receiver and long observation time leads to increasing the signal-to-noise ratio by up to 20 dB. The efficiency of such method strongly depends on the influence of pulse and harmonic clutter, which must be taken into account when applying it;

7. The configuration of a monostatic radar-sensor on the base of a quasioptical antenna-feeder path is developed, studied, and tested. The use of a quasioptical beam splitter provides high isolation between transmitter and receiver (> 60dB). The transceiver with common antenna is operated in W-band. The optimal parameters for the quasioptical duplex device are defined and an experimental study shows that the transmit-receive loss does not exceed 6.9 dB, the isolation between transmitter and receiver is not less than 60 dB, and the output beam well coincides with one of Gaussian shape. The use of an offset near-field Gregory antenna provides lack of back reflection to the feed and thus allows radar operation in a CW mode;

8. A double-frequency bistatic radar-sensor in CW mode is developed, constructed, and studied. The sensor operates in both W- and K_a-band, its construction provides antenna beam convergence for both radars, synchronous data input into a PC, and permits to minimize the influence of re-reflections from elements of the experimental set-up;

9. An experimental set-up for the study of electromagnetic scattering from disperse streams is developed on the base of a construction, which had initially been produced by DURAG GROUP company. The dispenser for dosing the particle flow is developed on the base of the ejection principle. It provides spraying of particles at least from 5 μm up to 1 mm in size. It was also shown that the particle size distribution of abrasive powders produced in industry obeys to the Weibull distribution law. A calibrated sea-sand powder was produced by sieving in order to confirm the validity of the proposed double-frequency method;

10. The comparison of data obtained by the mono-frequency radar-sensor and by contacting methods shows that the RCS of particles of arbitrary shape may be considered as resulting from particles of spherical shape, if their dimensions are essentially smaller than the wavelength. Furthermore, the use of the proposed method of mono-frequency sensing is possible only in the Rayleigh scattering regime. So the mono-frequency method of remote sensing permits to measure mass loading and particle concentration of disperse streams only in the case of a known particle distribution law and under the condition of Rayleigh scattering;

11. A comparison of data obtained from the double-frequency radar-sensor and from contact methods is also performed. It is shown that the effective root-mean-cube radius, the mass loading, and the concentration of particles are in satisfactory agreement when determined by both methods. The experimental data are characterized by a good reproducibility (coefficient of variation being $\leq 1\%$) in a wide region of particle flow consumption. The particle diameter and the mass loading, obtained by remote sensing both slightly exceed the data of contact measurements ($\leq 10\%$), while the particle concentration from remote sensing differs from contact data measurements more essentially ($\leq 25\%$);

12. The performed experimental study of the double-frequency method confirms the validity and the efficiency of the proposed method for remote sensing of disperse streams with preliminary unknown particle size distribution law.

References

[1] A. Seaton, D. Godden, W. MacNee, and K. Donaldson, "Particulate Air Pollution and Acute Health Effects," *Lancet*, vol. 345, no. 8943, pp. 176-178 January 1995.

[2] European Community, 2001b. Directive 2001/80/EC of the European Parliament and of the Council of 23 October 2001 on the limitation of certain pollutants into the air from large combustion plants. OJ L 309. 27.11.2001

[3] S. Inoue, *Video Microscopy*, Plenum Press, New York, 1986.

[4] R. Xu, *Particle Characterization: Light Scattering Methods*, New York: Kluwer Academic Publishers, 2002.

[5] C. Bernhard, *Particle size analysis: Classification and sedimentation methods*, Chapman&Hall, London 1994.

[6] J. C. Wilson and B. Y. H. Liu, "Aerodynamic particle size measurement by laser-Doppler velocimetry," *Journal Aerosol Science*, vol. 11, pp. 139-150, 1980.

[7] Edited by James P. M. Syvitski, *Principles, methods, and application of particle size analysis*, Cambridge university press, Cambridge, New York, 2007.

[8] V.D. Kutovoj, P.A. Samarskij, and S.I. Tregubov, "Study of particle ensemble with dimensions of hundreds microns by using scattering of submillimeter emission", *Trudy VNIIFTRI*, vol. 40 (70), pp. 27-88, 1979.

[9] N.V. Krasnogorskaya, Yu.Ya. Kurilenko, and I.M. Rybin. "Study of precipitation particle parameters in free atmosphere" *Phizika atmosphery i okeana*, vol. 3, no. 12, pp. 1292-1304, 1967.

[10] N. Gabas, N. Hiquily, and C. Laguerie, "Response of Laser Diffraction Particle Sizer to Anisometric Particles," *Particle & Particle Systems Characterization*, vol. 11, no. 2, pp. 121-126, April 1994.

[11] L. J. Battan, *Radar Observation of the Atmosphere*, Chicago: University of Chicago Press, 1973.

[12] J. Goldhrish, "Attenuation and Backscatter from a Derived Two-dimensional Duststorm Model," *IEEE Trans. on Antennas and Propagation*, vol. 49, no. 12, pp.1703-1711, December 2001.

[13] W. I. Rose, A. B. Kostinski, and L. Kelley, "Real-Time C-Band Radar Observations of 1992 Eruption Clouds from Crater Peak, Mount Spurr Volcano, Alaska," *Geological Survey Bulletin* B 2139, pp. 19-26, 1992.

[14] M. I. Skolnik, *Radar Handbook*, 3rd Ed., New York: McGraw-Hill Book Company, 2008.

[15] A. Ishimaru, *Wave Propagation and Scattering in Random Media*, vol. 1, New York, San Francisco, London: Academic Press, 1978.

[16] A. Teplyuk, R. Knoechel, and G. Khlopov, "Millimeter wave coherent radar with high spatial resolution for the determination of water content in aerosols," *Proc. of the European Microwave Association*, vol. 4, pp. 12-17, December 2008.

[17] E. I. Arsenian and A. A. Semenov, "Attenuation of ultra-short waves in dust-sand aerosol," Zarubezhnaya Radioelektronika, no. 1 pp. 16-26, 1995.

[18] B. E. A. Saleh and M. C. Teich, *Fundamentals of Photonics*, New York: J.Wiley & Sons, 1991.

[19] G. I. Khlopov, and V. P. Gudkov, "Millimeter wave quasioptical antennas for super-low range surveillance radar," *Telecom. and RadioEngineering*, vol. 51, no. 10, pp. 1-4, 1997.

[20] G. Khlopov, "High Isolation Duplex Millimeter Wave Quasioptical Antenna," *Proc. of Joint 29th International Conference on Infrared and Millimeter Waves and 12th International Conference on Terahertz Electronics*, pp. 697-698, September 2004.

[21] R. C. Hansen, *Microwave scanning antennas*, vol. I, Academic Press, New York and London, 1964.

[22] A. Teplyuk, R. Knoechel, G. Khlopov, and K. Schuenemann, "Radar measurement of mass loading of small volume scatterers," *Proc. of German Microwave Conference GeMiC 2008*, pp. 408-411, March 2008.

[23] S. M. Kay, *Fundamentals of statistical signal processing: estimation theory*, New Jersey: Prentice Hall, 1993.

[24] M. T. Abshaev and Y, A. Dadaly, "About the possibility of microstructure study of clouds and precipitations using radar methods," *Proc. Visokogorny Geofizichesky Institut*, no. 5, pp. 71 – 85, 1966.

[25] O. A. Vojtovych, A. M. Linkova, and G. I. Khlopov, "Study of double frequency method for remote sensing of solid aerosols," *Proc. Radiophysics and Electronics*, vol. 14, no. 2, pp. 169-176, 2009.

[26] R. Knoechel, G. Khlopov, A. Linkova, A. Teplyuk, K. Schuenemann, and O. Vojtovych, "Double frequency sounding of volume scatterers," *Proc. of International Radar Symposium IRS 2009*, pp. 437-441, September 2009.

[27] H. C. van de Hulst, *Light scattering by small particles*, New York: J. Wiley & Sons, 1957.

[28] W.J. Wiscombe, "Improved Mie scattering algorithms," *Appl. Optics*, vol. 19, no. 9, pp. 1505-1509, 1980.

[29] M. I. Skolnik, *Introduction to Radar Systems*, 3rd Ed., New York: Mc-Graw-Hill Book Company, 1991.

[30] G. Khlopov, and K. Schuenemann "Application of Millimeter Wave Coherent Radar for Remote Measurement of Vibrations and Displacements," *Proc. of Joint 29th International Conference on Infrared and Millimeter Waves and 12th International Conference on Terahertz Electronics*, pp. 761-762, September 2004.

[31] G. Khlopov, "Coherent radar in short millimeter wave band," *MSMW'04 Symposium Proceedings, 5-th International Kharkov Symposium on Physics and Engineering of microwaves, millimeter and submillimeter waves*, vol. 1, pp. 103-108, June 2004.

[32] I. V. Zvershhovsky, N. F. Karushkin, and M. I. Polgina, "Solid-state devices in millimeter wave range realized using silicon technology," *Proc. of 1st Ukrainian Symposium "Physics and techniques of millimeter and sub-millimeter radio waves"*, vol. 1, pp. 203-204, 1991.

[33] R. W. McMillan, "Near-millimeter-wave sources of radiation," *Proc. of the IEEE*, vol. 73, no. 1, pp. 86-108, January 1985.

[34] G. T. Wrixon, "Schottky-diode realization for low-noise mixing at millimeter wavelengths," *IEEE Trans. Microwave Theory & Tech.*, vol. 24, no. 11, pp. 702-706, November 1976.

[35] R. Knoechel, A. Teplyuk, G. Khlopov and K. Schuenemann, "Correlation processing of noise-like signals from coherent radar" *Proc. of International Radar Symposium IRS-2008*, pp. 103-106, May 2008.

[36] A. A. Minakov and O. F. Tyrnov, *Statistical Radiophysics*, Kharkov: V. N. Karazin Kharkiv National University, 2003.

[37] Alain Foure, *Perception et reconnaissance des Formes*, Edi Tests, 1985.

[38] V. I. Bezborodov, A. A. Kostenko, G. I. Khlopov, and M. S. Yanovski, "Quasioptical Antenna Duplexers," *International Journal of Infrared and Millimeter Waves*, vol. 18, no. 7, pp. 1411-1422, 1997.

[39] G. Goubau, *Electromagnetic theory and antennas*, New York: Pergamon *Press*, 1963.

[40] M. Born and E. Wolf, *Principles of Optics*, New York: Pergamon Press,1964.

[41] G. Trentini, K. P. Romeiser, und W. Jatsch, "Dimensionierung und elektrische Eigenschaften der 25 m Antenne der Erdefunkstelle Raisting für Nachrichten Verbindungen über Satelliten," *Frequenz*, no. 12, pp. 402-421, 1965.

[42] K. W. Brown and A. Prata, "A design procedure for Classical Offset Dual Reflector Antenna Circular Apertures," *IEEE Trans. on Antennas and Propagation*, vol. AP-42, no. 8, pp. 1145-1153, August 1994.

[43] G. N. Abramovich, *Applied gas dynamics*, 5th Ed., Moscow: Nauka, 1991.

[44] F. J. Pettijohn, *Sedimentary rocks*, New York: HarperCollins, 1983.

[45] L. G. Austin, S. L. Shojik, V. K. Bhatia, and F. F. Apian, "Extension of the empirical Alyavdin equation for representing batch grinding data," *Intern. J . Miner. Process.*, vol. 1, no. 2, pp. 107-123, 1974.

[46] L. R. Kittleman Jr., "Application of Rosin's distribution in size frequency analysis of clastic rocks," *J. Sediment. Petrol.*, vol. 34, no. 3, pp. 483-502, 1964.

[47] J. J. W. Rogers and C. Schubert, "Size distributions of sedimentary populations," *Science*, vol. 141, no. 3583, pp. 801-802, 1963.

[48] P. C. Reist, *Aerosol Science and Technology*, 2nd Ed., New York: McGraw-Hill, 1992.

[49] A. Teplyuk, R. Knoechel, and G. Khlopov, "Aerosol Particle Sensor based on Millimeter Wave Coherent Radar with High Spatial Resolution," *Proc. of 2009 IEEE MTT-S International Microwave Symposium*, pp. 1173-1176, June 2009.

[50] G. I. Khlopov, R. Knoechel, A. M. Linkova, K. Schuenemann, and A. L. Teplyuk, "Double frequency sounding of the polydisperse solid aerosols," *Journal Radiophysics and Electronics*, vol. 15, no. 1, pp. 51-61, 2010.

[51] G. Khlopov, R. Knoechel, A. Teplyuk, K. Schuenemann, "Application of double frequency radar for measurement of parameters of solid polydisperse aerosols", The 7th international Kharkov symposium on physics and engineering of microwaves, millimeter and submillimeter waves (MSMW'10), Kharkov, Ukraine, June 21-26, 2010.

[52] G. I. Khlopov, R. Knoechel, A. M. Linkova, K. Schuenemann, A. L. Teplyuk, and O. A. Voitovych, **"**Peculiarities of Double Frequency Radar for Polydisperse Aerosols Sounding", Telecommunication and radio engineering, vol. 70, no. 2 pp. 95-114, 2011.